

Czech Technical University in Prague
Faculty of Nuclear Sciences and Physical Engineering

Obor: Fyzikální inženýrství
Zaměření: Fyzika a technika termojaderné fúze



**Study of visible plasma radiation by
high resolution spectroscopy at
additional plasma heating by neutral
beams injection on the COMPASS
tokamak**

DIPLOMA THESIS

Autor: Bc. Tomáš Odstrčil
Supervisor: RNDr. Jan Stöckel CSc.
Year: 2012

zadání

prohlášení

Acknowledgement

I would like to thank my supervisor Dr. Jan Stöckel CSc. for providing a support for my work and a useful comments on this thesis. Moreover I am grateful to members of the COMPASS team for their patient during my *in situ* calibrations of the spectrometer. And finally I thank also Michal Odstrčil for a thorough proofread of this thesis.

Bc. Tomáš Odstrčil

Název práce:

Studium viditelného záření plazmatu s vysokým spektrálním rozlišením při dodatečném ohřevu plazmatu výkonovými neutrálními svazky na tokamaku COMPASS

Autor: Bc. Tomáš Odstrčil

Obor: Fyzikální inženýrství

Druh práce: Diplomová práce

Vedoucí práce: RNDr. Jan Stöckel CSc.
ÚFP AV ČR v.v.i.

Konzultant: —

Abstrakt:

Tato práce se zabývá měřením a vyhodnocením viditelného záření nečistot z okraje plazmatu pro měření teploty a rotace. K měření byl použit spektrometr s vysokou disperzí který byl pečlivě nastaven pro dosažení požadovaného rozlišení .

V rámci teoretické části jsou shrnuty nezbytné základy teorie záření plazmatu a důkladně prozkoumána teorie rotace plazmatu. V experimentální části je detailně popsán proces kalibrace spektrometru a následně shrnuto a diskutováno chování plazmatu na základě dat z tokamaku COMPASS.

Klíčová slova: Poloidální rychlost plazmatu, Dopplerův posuv, Pasivní spektroskopie, COMPASS, spektrometr s vysokou disperzí

Title:

Study of visible plasma radiation by high resolution spectroscopy at additional plasma heating by neutral beams injection on the COMPASS tokamak

Author: Bc. Tomáš Odstrčil

Abstract:

This work deal with the measurement of visible light radiation of the impurities at the plasma edge for estimation of temperature and plasma rotation. The measurement was realized by a high dispersion spectrometer which was patiently focused in order to achieve the desired parameters.

In the theoretical part of this theses, theory of plasma radiation was summarized and the theory of the plasma rotation was thoroughly investigated. In the experimental part of this thesis, the focusing proses was described in detail and the observed plasma behavior based on the data from COMPASS tokamak was discussed.

Key words: Poloidal plasma velocity, Doppler shift, passive spectroscopy, COMPASS, high dispersion spectrometer

Contents

1	Introduction	9
1.1	Thermonuclear Fusion	9
1.1.1	What is fusion?	9
1.1.2	Conditions for Fusion	10
1.1.3	Magnetics Confinement	12
2	Tokamak COMPASS	15
2.1	History of the COMPASS tokamak	15
2.2	The scientist program for the COMPASS	16
2.3	COMPASS diagnostics	16
2.3.1	Magnetics diagnostics	17
2.3.2	Probe diagnostics	18
2.3.3	Interferometer	18
2.3.4	Doppler reflectometer	18
2.3.5	Thompson scattering system	18
2.3.6	Multi range tomography system	18
2.3.7	Spectrometers	19
2.3.8	High resolution spectrometer for plasma rotation measurement	19
2.4	Neutral Beam Injectors	20
3	Plasma radiation in tokamaks	22
3.1	Radiative processes	22
3.1.1	Line radiation	23
3.1.2	Bremsstrahlung	24
3.1.3	Recombination radiation	24
3.2	Collisional processes	25

3.3	Plasma models	26
3.3.1	TE (Thermodynamic Equilibrium) model	26
3.3.2	LTE (Local Thermodynamic Equilibrium) model	27
3.3.3	Coronal model	27
3.3.4	CR (Collisional Radiative) model	28
3.4	Line broadening mechanisms	29
3.4.1	Natural broadening	30
3.4.2	Doppler broadening	30
3.4.3	Stark broadening	30
3.4.4	Zeeman splitting and Motion Stark effect	31
3.4.5	Instrumental broadening	32
3.5	Applications in tokamak plasma	32
4	Plasma Rotation	34
4.1	Momentum balance equation	35
4.2	Momentum transport	37
4.2.1	Flux surface average	38
4.2.2	Momentum sources and sinks	39
4.3	Neoclassical rotation	40
4.3.1	Poloidal velocity dumping	41
4.3.2	Impurities rotation velocity	42
4.4	Radial electric field	43
4.5	MHD rotation	43
5	High dispersion spectrometer	45
5.1	Experimental setup	45
5.1.1	Description	46
5.1.2	Detector	47
5.1.3	Optical path	48
5.2	Focusing of the spectrometer in dispersion plane	48
5.2.1	Focusing as a mathematical problem	50
5.2.2	Optimization algorithms	50
5.2.3	Focusing on the position of the CIII triplet	52
5.3	Focusing of the spectrometer in the sagittal plane	53

5.4	Instrumental function	54
5.4.1	The definition	54
5.4.2	Measurement of the instrumental function	56
5.5	Wavelength calibration	57
5.5.1	Differential Doppler spectroscopy line	57
5.5.2	Reference line	60
5.5.3	Other ways	60
5.6	Limits of the achievable accuracy	63
5.6.1	Statistical uncertainty	63
5.6.2	Systematic uncertainty	65
6	Spectrometers control	68
6.1	Ocean Optics spectrometers	68
6.1.1	Spectrometer Control	68
6.1.2	Data analyse	68
6.2	High resolution spectrometer	70
6.2.1	Andor Camera control	70
6.2.2	Data extraction	70
6.2.3	Data analyzing	70
7	Results	71
7.1	Spectrometer configuration	71
7.2	Line integrated characteristic of the plasma	72
7.2.1	Zero momentum	72
7.2.2	First momentum	74
7.2.3	Second momentum	74
7.3	Plasma rotation	78
7.3.1	Neoclassical prediction	78
7.3.2	Rotation in ohmically heated plasma	79
7.3.3	Rotation in NBI heated plasma	79
7.3.4	Rotation measured on COMPASS in Culham	83
7.4	Ion temperature	83
	Conclusions	88

Chapter 1

Introduction

1.1 Thermonuclear Fusion

One of the main tasks for mankind in the next decades will be probably solution of problems with growing consumption of energy. Moreover increasing demands on the stability and greenness of the power sources limit the acceptable solutions. The steep raise of energy consumption can be expected also in the developing countries and it can not be expected that people from the developed countries will be willing to decrease their standards of living.

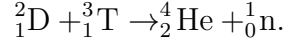
Therefore a new sources of energy must by produced. Almost 80% of the world energy is created by burning of the fossil fuels (coal, natural gas and petrol). However, the fossil fuels have limited reserves and therefore it will soon run out. The next disadvantage of the fissile fuels is production of pollution and so called greenhouse gases. The second most important energy source is nuclear fission. The fission energy is much cleaner compared to the previous one but it suffers from several disadvantages i.e requirements of long term storage for nuclear waste or political pressures that made it almost impossible to build a new fission power plants now. The last important group of power sources are so called it renewable energy sources. However, these sources also suffer from many disadvantages, for example low power density, low reliability and high price.

Therefore among other energy sources currently developed, the thermonuclear fusion should have advantage of cheap and geographically evenly distributed fuel, little of the long term radioactive waste and high power density. On the other hand these advantages are balanced by physical, engineering and economical difficulties connected with developing and building of thermonuclear power plant. The thermonuclear fusion energy can be successful only if we will find a way how to produce it cheaply.

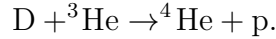
1.1.1 What is fusion?

The nuclear fusion is defined as a process by which two atomic nuclei are jointed together to create one single heavier nucleus. Energy is produced during the fusion if the fusion product is not heavier than iron (Fig. 1.1) that has highest binding energy. Most of the fusion energy is released in the interior of the stars where hydrogen and also heavier nucleus are fused. But not all fusion reactions are useful for the production of the energy

on the Earth. The cross section of the most common proton-proton reaction in the Sun is so low that power density in the sun is less than 300 W/m^3 [1]. However, much more promising fusion reaction has been discovered. The highest reaction cross section at the lowest energies has reaction of the deuterium and the tritium (Fig. 1.2)



Fusion of deuterium with tritium create helium, freeing a neutron, and release 17.6 MeV of energy. The neutron obtains 4/5 of fusion energy and the α -particle only 1/5 because of energy and momentum conservation laws. High energy neutrons are disadvantage of this reaction, because they damage plasma facing materials (PFM). On the other hand, fusion power is distributed to the deeper layers of the container of the plasma, therefore the surface power density incidenting on the PFM is much lower. Further, tritium is radioactive isotope of hydrogen, beta emitter, with half-live of 12 years. Tritium economy and tritium safety will markedly increase complexity and price of the fusion power plants. Therefore so called *advance fuels*, where fusion products are only charged particles, can be tested in future. An example of such reaction is



This type of the reaction can not be accomplish in the present-day devices because the fusion temperature is more than $10\times$ higher.

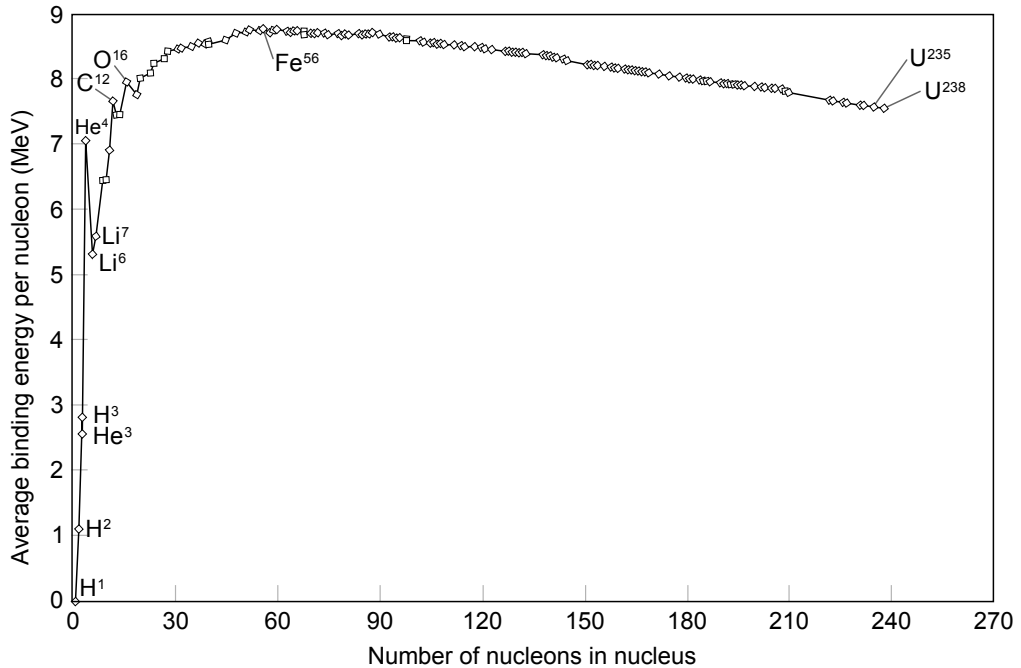


Figure 1.1: Binding energy curve of the most common isotopes

1.1.2 Conditions for Fusion

The plasma is a relatively complex physical system which is still not fully understood. Nevertheless, it is possible to derive a criterion for the fusion ignition based on simple assumptions. This condition for D-T fusion was derived by John D. Lawson in 1955 and

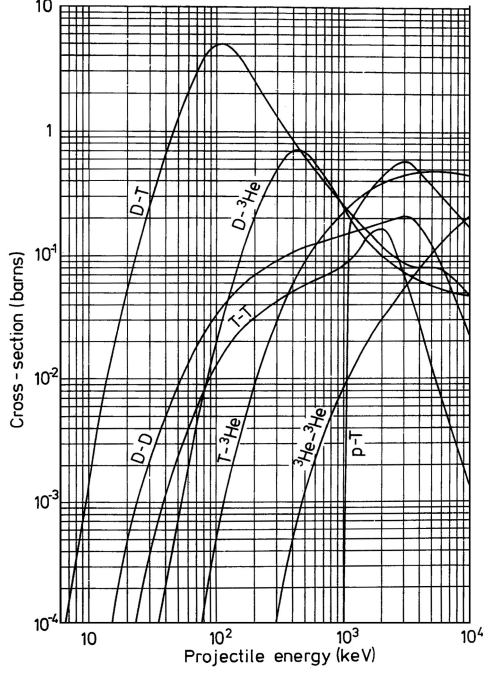


Figure 1.2: The fusion reaction rate for the most important fusion reactions

published in 1957 [2]. Later analyses suggested that so called *triple product* is more useful. It is product of density, confinement time, and plasma temperature T . Triple product is defined by following formula

$$nT\tau_E > 5 \cdot 10^{21} \text{keVs/m}^3,$$

where n denoted plasma density, T temperature and τ_E is a energy confinement time defined as

$$\tau_E = \frac{W}{P_{\text{loss}}},$$

W is total energy stored in plasma and P_{loss} is power of energy losses.

The Lawson criterion express a simple idea that the energy created by fusion must exceed the losses expressed by τ_E . Every single quantity in the Lawson criterion can be experimentally achieved almost arbitrary high, but every times we paid for that by decrease of the other quantity. The temperature can not be chosen arbitrary, because the cross section of the D-T reaction is highest close to temperature 10 keV, hence only n and τ_E can be changed.

At present the most promising are two very different concepts of a hot plasma confinement. The first is *inertial confinement* where should be achieved extremely high density ($\sim 10^{32} \text{m}^{-3}$) but much lower confinement time ($\sim 10^{-10} \text{s}$). The second concept, which is much closer to the scope of this thesis, is *magnetic confinement*. Unlike the inertial confinement, densities achievable in magnetically confined plasma are much lower ($\sim 10^{21} \text{m}^{-3}$). But the energy confinement time is high enough (about 10 s) to fulfill the Lawson criterion.

1.1.3 Magnetics Confinement

The plasma for magnetic confinement fusion mainly consist of charged particles, therefore the movement of these particles is influenced by magnetic and electric field. In early experiments with an electrostatics confinement [3] the expected results were not achieved. Therefore experiments with electromagnetic and magnetic confinement started to be tested. The most promising from the point of transport theory [4] should be infinitely long linear (cylindrical) magnetic device. But real linear devices have never achieved the predicted parameters mainly due to plasma instabilities and end losses of particles and energy. Further, the toroidal devices have been tested, because intuitively, one might expect that the transport in toroidal devices with successfully large main radius and small minor radius could closely approximate the ideal linear device. However toroidal (neoclassical) effect are significant even in this limit. Only the toroidal shape of the vacuum vessel is not enough to confinement the plasma. The main reason are particle drifts caused by the gradient and curvature of magnetic field. The latter drift causes particles movement in vertical direction, opposite for electron and ions. This charge separation immediately creates electric field and together with toroidal magnetic field leads to an outward drift of all particles.

Several concepts of such magnetic confinement devices has been proposed and studied up to date, among others stellarators [5] and tokamaks [6] have attained reasonable results. However better results have been observed on tokamaks¹, mainly due to neoclassical diffusivity by ripple trapped particles in stellarators. Poloidal component of the magnetic field is generated by a toroidal plasma current. The plasma current usually is induced by a transformer, where the plasma is the secondary winding (Fig. 1.3).

Due to the toroidal symmetry the field lines lie on the *magnetic surfaces*. This can be derived from Grad–Shafranov equation [7, 8]. The magnetic surfaces create an infinite set of nested surfaces which are perpendicular to the gradient of the pressure. Because particle transport within magnetic surfaces is much faster than transport perpendicular to them, many plasma properties can be considered to be constant over magnetic flux surfaces. One of the important properties defined on magnetic surfaces is a *safety factor* q

$$q = \frac{\Delta\phi}{2\phi} \approx \frac{rB_\phi}{RB_\theta},$$

where $\Delta\phi$ is the toroidal angle circumscribed by magnetic field line after one full circle (2π) in poloidal direction. The expression on the right side is approximation for small aspect ratio (relation between minor (r) and major (R) radius of torus). Close to the surfaces with low rational number of q instabilities can easily arise. And also $q > 1$ inside the plasma, so called *Kruskal-Shafranov current limit* is necessary condition for stability of plasma column against kink instability [9, 10].

After a half century of progress in the research of the magnetic confinement a large international project is realized. This project is called the International Tokamak Experimental Reactor ITER [12] (*iter* also means *the way* in Latin). This will be the first prototype of fusion energy plant capable of producing 500 MW of thermal energy in neutrons during 500 s long plasma discharge. This power should 10 times exceed necessary heating power from auxiliary heating systems. ITER is one of the biggest science project ever, supported

¹Tokamak was invented by Tamn and Sakharov (1961)

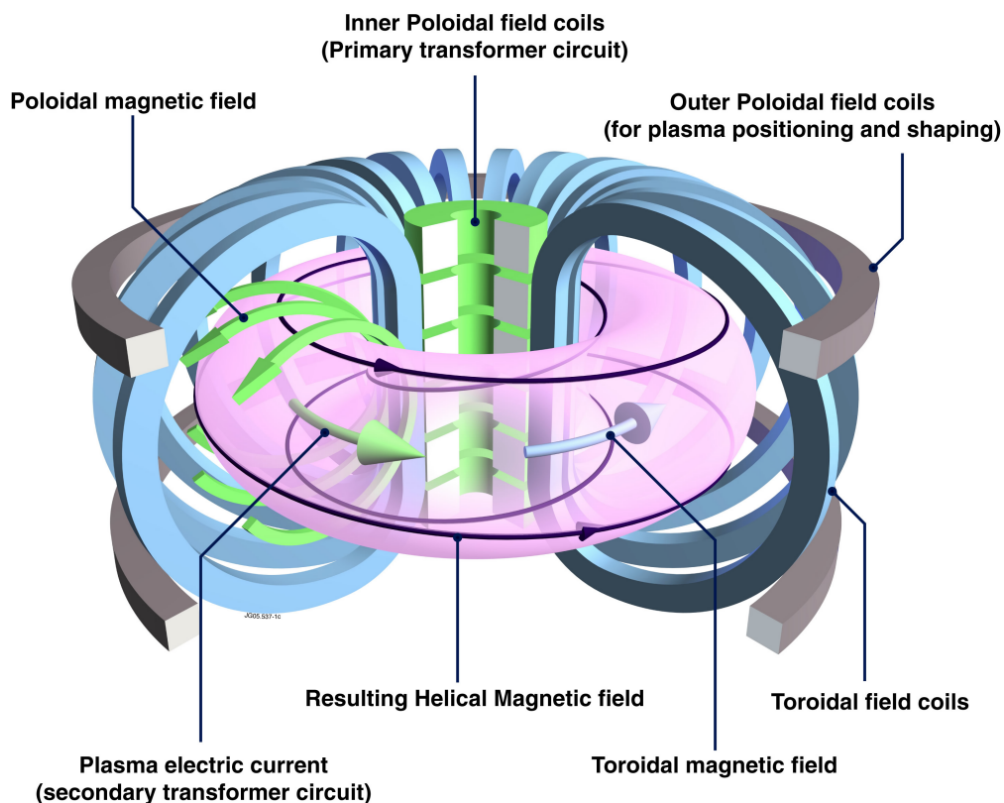


Figure 1.3: Principle of the tokamak: superposition of the toroidal and poloidal field create helical magnetic field which prevent $E \times B$ drift of the particles and consequent loss of the confinement [11]

by 7 parties, EU, USA, India, Russian, South Korea, China and Japan, representing most of the world population. Detail information about this project can be found in the actual ITER plant description [13].

Also the COMPASS, 10 times smaller in linear scale tokamak from UKAEA at Culham, was reinstalled in Czech Republic [14, 15]. It is the smallest tokamak with a clear H-mode and ITER relevant geometry. The role of this tokamak will be studying of the H-mode (high confinement mode) and edge plasma, especially *pedestal*, the part of the plasma on the edge where step gradients of the temperature and density occurs. The second important contribution to plasma knowledge can be from scaling laws. The ITER parameters are extrapolated mostly from middle and large size tokamaks, however for a reliability of the extrapolation also results from small tokamaks with ITER relevant parameters should be used.

The structure of this thesis is following:

Chapter 2: provides basic information about COMPASS tokamak, the scientist program and overview of accessible diagnostics including their actual status.

Chapter 3: contains a theory of the plasma radiation in the tokamaks. Many radiative processes and models are explained. Moreover the sources of the spectral line broadening in plasma were investigated.

- Chapter 4:** presents a summary of concepts about momentum transport and intrinsic rotation, including estimated impact of the COMPASS neutral heating injection.
- Chapter 5:** is devoted to describing of the experimental setup. Moreover a very complex problem of precise spectrometer focusing and wavelength calibration is examined in detail.
- Chapter 6:** contains a short description of the programs developed for the control and evaluating of data from the COMPASS spectrometers.
- Chapter 7:** reports and discuss the observation of the ion temperature and plasma rotation on tokamak COMPASS.

Chapter 2

Tokamak COMPASS

A brief description of the COMPASS tokamak has been already provided at the end of the previous chapter. This section contains more detailed description of this tokamak, its history and also overview of available diagnostics.

Basic parameters of the tokamak are summarized in the table 2.1. The present parameters are in the second column and the parameters already achieved in UKAEA or planned with new heat sources in IPP are in the last column.

Parameters	Current values	Expected max. values
Major radius R		0.56 m
Minor radius a		0.18 m
Inverse aspect ϵ	0.32	
Plasma current I_p (max)	100 kA	350 kA
Magnetic field B_T (max)	1.8 T	2.1 T
Vacuum pressure	$5 \cdot 10^{-6}$ Pa	$1 \cdot 10^{-6}$ Pa
Elongation	1.0	1.8
Plasma shape	circular	D, SND, elliptical, circular
Pulse length	0.25 s	1.0 s
Current drive PLH 1.3 GHz	0 MW	0.4 MW
Beam heating PNBI 40 keV	0.3 MW	2×0.3 MW

Table 2.1: Main parameters of the COMPASS tokamak in Prague

2.1 History of the COMPASS tokamak

COMPASS tokamak was designed as a flexible small tokamak in 1980's to explore MHD activity with D-shaped and circular plasma, Operation has started at 1989 and in 1992 was restarted with D-shaped vacuum vessel (and renamed from COMPASS-C to COMPASS-D). Because of MHD studies, tokamak is equipped by high number of the diagnostics coils and also the configurations of the poloidal and the vertical magnetic fields coils are easily variable [8].

The tokamak is also equipped by set of four quadratics saddle coils to create resonant

magnetic perturbations. Pioneering experiments with perturbation fields has been done on COMPASS in UKAEA. In these experiments will be continued by development of the ELM mitigation technique [16]. And also a resonance and non-resonance plasma rotation breaking should be studied.

However due to lack of manpower to run the MAST and COMPASS in UKAEA together it was decided to shutdown the COMPASS. And it was also the reason, why was the tokamak given to IPP in Prague [14]. In December 2006, tokamak was transported to Prague. Two years later, first plasma was generated in COMPASS and in February 2009 was the official start of the tokamak operation.

2.2 The scientist program for the COMPASS

The main topics of the scientist program of the COMPASS tokamak were concluded in the article [15] about reinstallation of this tokamak in Prague.

- Edge plasma physics
 - H-mode studies
 - Resonant Magnetic Perturbation technique for the ELM suppression
 - Plasma-wall interaction
 - Turbulences in tokamak plasmas and particle transport
- Wave-plasma interaction
 - Parasitic lower hybrid wave absorption on front of antenna
 - Lower hybrid wave coupling
 - Research on generation and detection of the Electron Bernstein Waves (EBW)
- Development of advanced diagnostic methods
 - Advance reciprocal probes
 - Hall detector
 - Thomson scattering

These goals can not be achieved without very good edge and pedestal diagnostics. Therefore, both the best possible spatial and high time resolution of these diagnostics are necessary. The most important diagnostics for the edge diagnostics are spectroscopy, microwave, probe diagnostics and magnetic.

2.3 COMPASS diagnostics

COMPASS tokamak is equipped by a basic set of the magnetic, optics, microwave and probe diagnostics. A short overview of these diagnostic will be presented here. Positions of the individual diagnostics are plot on Fig. 2.1.

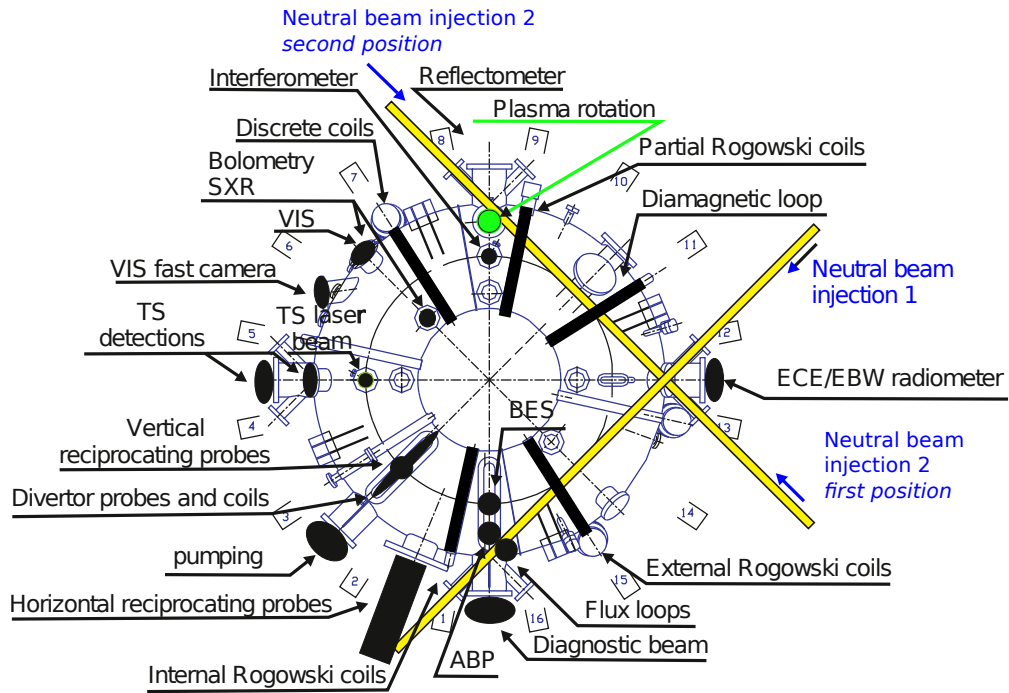


Figure 2.1: Positions of the most important diagnostics in COMPASS [17]. The port for plasma rotation measurement has a green colour.

2.3.1 Magnetics diagnostics

Magnetics diagnostics are the most basic equipment of the every tokamak. COMPASS is equipped with a rich set of the 440 coils arranged over all tokamak vessel [18]. However, only 70 of them are currently in use, because of limited number of currently available data acquisition channels.

- 4 Mirnov coils for B_θ measurement placed equidistantly in toroidal direction around the vessel.
- 16 internal partial Rogowski coils for precise measurement of mean B_θ in 16 equidistant poloidal directions around the torus.
- 8 flux loops without integration for measurement of the U_{loop} voltage
- 8 flux loops with integration for poloidal flux measurement
- 6 Rogowski coils for measurement of the current in the tokamak coils
- 1 Rogowski coil inside vessel for I_p measurement
- 1 Rogowski coil outside for $I_p + I_{vessel}$ measurement
- 2 diamagnetic loops for measurement of the plasma diamagnetism, necessary for calculation of energy stored in the plasma

Magnetics equilibrium reconstruction is still not implemented. The plasma position is now calculated only from a few chosen partial Rogowski coils. And the second problem closely connected to magnetic diagnostic is very strong electromagnetic noise in some diagnostics caused by tokamak power sources.

2.3.2 Probe diagnostics

Two reciprocal probes are installed on the COMPASS tokamak. The first come from EPFL Switzerland [19] and the second came from CCFE, UK with COMPASS. Both probes should be able to investigate scrape of layer (SOL) of the plasma with time resolution up to $1 \mu\text{s}$ and radial resolution 2-4 mm. The reciprocal probes heads are interchangeable and compatible with ASDEX Upgrade manipulator. Therefore SOL can be investigated by many different probes. Currently only I-V characteristics with Langmuir probe is measured, however in future also a Much probe can be installed and the plasma velocity in the SOL estimated.

2.3.3 Interferometer

The interferometer for the line integrated electron density measurement has been developed in CCFE and transported to Prague together with the tokamak. The phase shift is measured on two close frequencies 131 and 133 GHz propagating through plasma in opposite directions. This way a high stability and reliability of density measurement has been achieved. High reliability is necessary condition for a planned real-time density control.

2.3.4 Doppler reflectometer

Microwave Doppler reflectometer [20] for study of the fast events at the plasma edge was tested on COMPASS. Frequency range of the reflectometer operation is 26.6 – 40 GHz, but the frequency can not be changed during discharge. The reflectometer was not set perpendicularly, but it was inclined by 18 degrees in poloidal direction. This device should be also capable of the measurement of the poloidal plasma rotation [21]. However the reflectometer was tested only shortly at the turn of the year 2011 and 2012 and the results were inconsistent.

2.3.5 Thompson scattering system

The Thompson scattering system is already fully operable. The light gathering optics is divided to two parts – core region and edge region. The spatial resolution of electron density and temperature measurement is 10 mm at plasma centre and 3-5 mm at the plasma edge. Time resolution is 30 Hz when lasers are triggered simultaneously or an arbitrary time gap between lasers can be set. Details about this Thompson scattering system are published in [22].

2.3.6 Multi range tomography system

The systems for a plasma radiation observation in visible, XVUV and SXR were recently installed on the tokamak. This systems are capable of acquiring light with a few μs time resolution and spatial resolution about 1 cm in pedestal region [23].

In the visible light diagnostics should by possible to install interference filter and observe the radial distribution of the most intense spectral lines. Light is collected from wide-angle

objective to 37 optical fibres. The light is collected by array of the photodiodes S4114-35Q by Hamamatsu, which will be replaced by array of photomultipliers H7260A also by Hamamatsu. In the early stages of this experiment, also the plans for plasma rotation and bremsstrahlung radiation measurement was proposed [24], however it is not very probable that it will be finished soon.

Soft X-rays are detected by two 35 channel SXR sensors LD35-5T covered by $5\ \mu\text{m}$ thick beryllium foil. The highest efficiency of this detector is in the range 0.5-20 keV. The detectors are placed in upper and lower ports on the high field side (HFS) together with the bolometers and the visible light diagnostics.

Fast bolometric measurement is based on six 20 channel AXUV silicon bolometers AXUV20-ELM. Two pairs are placed in up and down port on the low field side (LFS) of the tokamak and the rest are in up and down port on the high field side. The appropriate cover of the plasma cross section by lines of sight is essential for a tomographic radiation profile reconstruction. For that reason a stability and speed of the algorithm for the tomographic reconstruction by Minimal Fisher information algorithm [25, 26] has been improved and it is able to perform the full tomographic reconstruction between discharges (about 15 min).

2.3.7 Spectrometers

Presence of the impurities in the plasma is currently measured by three single channel spectrometers Ocean Optics HR 2000+. Two of these spectrometers are dedicated only for impurities observation, one of them is for UV range 248-472 nm and the second for visible range 457-663 nm. Both are connected to the tokamak by 20 m long optical fibres. In presence, only spatially integrated radiation from plasma, perpendicular to toroidal direction is observed. But it is also possible to connect them as 2 of 37 channels from visible tomographic system and measure the impurities radiation with some limited spatial resolution. The maximal time resolution of these spectrometers is 1 kHz, but due to low light intensity the spectra are acquired only with 100 Hz frequency (10 ms exposure time).

The third spectrometer is designed for motion Stark effect measurement (more in section 3.4.4) on the $\text{H}\alpha$ line from neutral beam. For such measurement a high dispersion is necessary, hence the spectral range of this spectrometer is 629-680 nm and dispersion 0.025 nm/px. The resolution should be sufficient to recognize motion stark effect from neutral beam and also the stark splitting due to fast movement of these neutrals in strong toroidal magnetic field [27]. Moreover this spectrometer could be also suitable for the measurement of the toroidal plasma velocity on the CII line (657.8 nm), because the shift of the line over 1 pixel corresponds to velocity $\sim 10\ \text{km/s}$. The most important properties of these spectrometers summed up in table 2.2.

2.3.8 High resolution spectrometer for plasma rotation measurement

The high resolution spectrometer is designed for measurement of the poloidal rotation velocity. The plasma rotation velocity measurement is based on the observation of the Doppler shift of some spectral lines. The bulk plasma poloidal velocity is usually much smaller than the thermal velocity of the ions. The ion temperature at the cold plasma

Type	Ocean Optics HR2000+		
Serial number	HR+C0732	HR+C1103	HR+C1834
Spectral range [nm]	457-663	247-472	629-680
Resolution	2048 pixels		
Readout noise	400 photoelectrons (10 counts)		
Readout speed	≤ 1 kHz		
Focal length	101.6mm		
Numerical aperture	0.125		
Dynamic range	1300:1		

Table 2.2: Basic properties of the spectrometers for impurities observation on the COMPASS tokamak

edge is approximately ~ 20 eV and the thermal velocity of carbon ions is ~ 20 km/s. The poloidal rotation in similar experiments with circular plasma, without NBI is usually $0 - 2$ km/s at the plasma edge, for example in TEXTOR [28] or TCV [29].

Such small shift can be measured only by highly stable spectrometer with very high dispersion. This properties should be fulfilled by spectrometer made in ISTTOK tokamak [30]. This spectrometer is designed for observation of the CIII triplet (465 nm), because these are usually the most intense impurities lines in tokamak plasma. The dispersion of this spectrometer is 0.16–0.19 nm/mm, but more illustrating is the dispersion recalculated to Doppler shift, which is 2 km/s/px. The system has been upgraded from previous configuration by EMCCD detector for low light high speed application. Time resolution of the device is up to 0.5 ms and spatial resolution is theoretically up to 5 mm.

More details about this spectrometer and program for evaluating of the spectra will be provided in Chapter 5.

2.4 Neutral Beam Injectors

Two new neutral beam injectors (NBI), developed in Budker Institute, Novosibirsk, were installed to COMPASS at the beginning of year 2011. The basic parameters of the NBI are in the table 2.3. These injectors were primary designed for plasma heating and current drive [31]. The power of the beams can be modulated to achieve theoretically arbitrary heating power. The neutral beams are injected tangentially to increase trajectory length of the fast neutrals through plasma.

NBI will be used in two different configurations.

- In the first configuration optimized for plasma heating, both NBI will be installed in co-direction to plasma current to minimize orbit losses of fast particles. Position of the first and the second NBI are in Fig. 2.1, 2. NBI will be in the first position.
- The second configuration of the spectrometers is optimized to achieve minimal momentum input to the plasma, so called balanced injection. It should be possible to study slowly rotating plasma, one of the ITER relevant conditions. The position of the second NBI is illustrated in Fig. 2.1.

Currently only the second NBI is connected to tokamak in position 2 and only very short beam injections are possible. Moreover

The behaviour of the beam inside the COMPASS tokamak was intensively studied by simulations Monte Carlo code FAFNER [31], NBEAMS, current drive by ACCOME code and plasma transport, heating was determined by ASTRA code. The heating and current drive with the NBI and LHCD was studied in the article [32]. However, detailed study of the momentum input was not performed yet. Typically it is performed by verified Monte Carlo simulations, for example TRANS code [33].

Heating particles	H, D
Number of NBI	2
Energy of beam	< 40 keV
Max. ion current	2×13 A
Max. pulse length	2×0.3 MW
Focal length	1.8 m
Divergence of the beam	0.7°
Beam diameter at focus	5.5 cm
Power input (from flywheel generator)	0.7 MVA

Table 2.3: Basic parameters of the COMPASS NBI system [34]

Chapter 3

Plasma radiation in tokamaks

Radiation is the typical property characterizing the plasma. The plasma can emit and absorb the radiation and in the thermodynamic equilibrium these processes are in balance. But the conditions for thermodynamic equilibrium can not be fulfilled in any tokamak device, because of low density and size. An example of the system, where the plasma is close to thermodynamic equilibrium is only the interior of the Sun.

Plasma radiation is influenced by conditions and processes occurring in the plasma. Every charged particle is influenced by the electromagnetic field of neighbouring particles and it results in radiation. Theoretically, plenty of information about plasma can be extracted from this radiation. However, due to constraints in the measurement and very complicated interpretation of results by imprecise models, the analysis of radiation is very complicated. Determining of plasma parameters from radiation is the aim of the plasma spectroscopy.

Two kinds of physical processes in plasma are important for the population kinetics in the plasma - *radiative processes* and *collisional processes*.

3.1 Radiative processes

Most of the radiation in plasma comes from electrons and their transitions from higher to lower energy levels, bounded or unbounded. Part of their energy can be lost as the radiation. Probability of these processes is usually determined by *rate coefficient* R calculated from process cross section $\sigma(v)$ by averaging over Maxwell distribution $f(v)$ of the particles

$$R \equiv \langle \sigma v \rangle = \int \sigma(v) f(v) dv.$$

The most common types of radiation observed in plasma are:

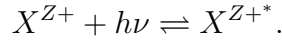
- **Line radiation** is a discrete line radiation created by transitions of the electron in the atom shell. This type of transition is called *bound-bound transition*.
- **Recombination radiation** is a radiation in plasma caused by recombination of the electrons. This radiation is continuum, because free electrons can have arbitrary energy with respect to their distribution function. The radiated spectra has edges

at ionization energy, because free electrons can have lower energy. This transition is called *free-bound*.

- **Bremsstrahlung** continuous radiation caused by acceleration and deceleration of the charged particles in plasma during their coulomb collisions. This radiation is called *free-free*.

The previous list of general mechanism of radiation in plasma is caused by different processes in plasma. Here is list of the radiative reactions:

- **Photo excitation/de-excitation**
Photo excitation/ de-excitation of ion X^Z is the following process

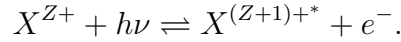


The rate of photo excitation process is given by

$$R_{ij}^{\text{ex}} = 4\pi \int \alpha_{ij} \frac{I(\nu)}{h\nu} d\nu,$$

where $I(\nu)$ is angle averaged intensity and α_{ij} is absorption cross section [35, 36].

- **Photo ionization/recombination**
Photo ionization/recombination is described by



Photoionization rate of ion X^Z to X^{Z+1} is given by

$$R_{ij}^{\text{ion}} = 4\pi \int \alpha_{Z(Z+1)} \frac{I(\nu)}{h\nu} d\nu,$$

The cross section if this process is published in [35, 36].

3.1.1 Line radiation

Characteristic radiation due to de-excitation of the excited states of the ions¹ is a common part of the observed spectra. De-excitation of the excited state is caused by a spontaneous or a induced decay. The radiation is discrete, because the bounded electrons in the ions shells can only exist in discrete energy levels. The photon energy that is radiated after the transition from level n to l is equal to

$$\Delta E_{nl} = \hbar\omega = E(n) - E(l).$$

The probability of the spontaneous and the induced decay can be computed from the quantum mechanics. The probability of the spontaneous emission can be expressed by *Einstein coefficient* $A_{n \rightarrow l}$ [s^{-1}] and coefficient B_{ij} for stimulated absorption ($i < j$) or emission ($i > j$). These coefficients are calculated from the quantum mechanics or a

¹For clarify consider neutral atoms as zero times ionized ions.

dedicated experiment. The emission coefficient $\epsilon_{n \rightarrow l}(r)$ (the power radiated from a unit volume to a unit solid angle) can be calculated as

$$\epsilon_{n \rightarrow l}(\mathbf{r}) = \frac{1}{4\pi} n_n A_{n \rightarrow l} \Delta E_{nl} \quad [\text{W} \cdot \text{m}^{-3} \cdot \text{sr}^{-1}],$$

where n_n is a density of the excited state. However, the induced emission is negligible in typical tokamak plasma conditions.

The spectral emission coefficient can be expressed as a dimensionless normalized line shape $\phi(\nu)$

$$\epsilon_{n \rightarrow l}(\mathbf{r}, \nu) = \epsilon_{n \rightarrow l}(\mathbf{r}) \phi(\nu).$$

The line shape $\phi(\nu)$ depends on the radiation process and the plasma conditions. The shape of line of the single unperturbed ion is given only by the natural broadening caused by the finite lifetime of the excited state. However, the contribution of this broadening to the final shape of the line in typical plasma is negligible. Examples of the relevant types of broadening in plasma are Doppler broadening caused by the Doppler shift of the photons due to their fast movement of the ion and the Stark broadening caused by collisions in a dense and cold plasma [27].

3.1.2 Bremsstrahlung

Bremsstrahlung is caused by the Coulomb collisions of charged particles in plasma. From the point of view of the quantum mechanics, the collisions corresponds to transitions between two quantum states with continuum value of energy. The spectral emission coefficient of the bremsstrahlung is given by formula [37]

$$\epsilon_{\text{ff}}(r, \nu) = \frac{1}{4\pi} n_e^2 Z_{\text{eff}} \left(\frac{e^2}{4\pi\epsilon_0} \right)^3 \frac{32\pi^2}{3\sqrt{3}m^2c^3} \left(\frac{2m}{\pi T} \right)^{\frac{1}{2}} e^{-\frac{h\nu}{T}} \bar{g}, \quad (3.1.1)$$

where the effective charge Z_{eff} is defined as

$$Z_{\text{eff}} = \frac{\sum_Z n_Z Z^2}{\sum_Z n_Z}$$

and \bar{g} is Maxwell-averaged Gaunt factor which is close to 1. More precise approximations of the \bar{g} for different plasma conditions are in [37, 27, 38]. Under conditions of interest in the tokamak, Gaunt factor is $\simeq 2\sqrt{3}/\pi = 1.1$ and formula (3.1.1) can be simplified [8] and wavelength integrated radiated power is

$$\epsilon_{\text{ff}}(r, \nu) = 5.35 \cdot 10^{-37} n_e^2 Z_{\text{eff}} T_e^{1/2} \quad [\text{W} \cdot \text{m}^{-3} \cdot \text{sr}^{-1}, \text{m}^{-3}, \text{eV}],$$

and an example of the calculated shape of the bremsstrahlung spectra is in the graph 3.1.

3.1.3 Recombination radiation

When a free electron is captured by a ion, the excess energy is radiated as a photon. The energy of this photon is given by

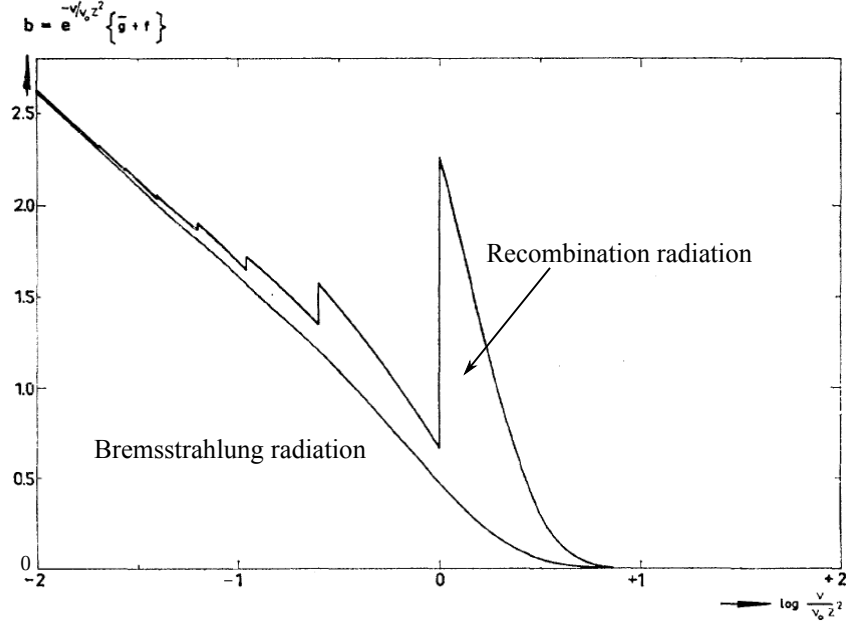


Figure 3.1: An example of calculated recombination radiation and bremsstrahlung radiation [38]

$$E = h\nu = E(\eta) - E(l) = E_{\text{kin}} + (E_{\infty} - E(l)),$$

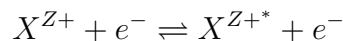
where $E(\eta)$ is energy of the free state of the electron, $E(l)$ is the energy of the energy level l , where was the electron captured, E_{kin} is a kinetic energy of free electron and E_{∞} is the ionization energy from ground level. Typical shape of recombination spectra is in graph 3.1.

3.2 Collisional processes

The most common processes leading to excitation or ionization in the tokamak plasma are collisional processes.

- **Electron impact excitation/de-excitation**

Energy from the free electron is transferred by a collision to a bounded electron in the ion and transferred energy is lower than the ionization energy. Then the bounded electron stay captured on higher energy level.

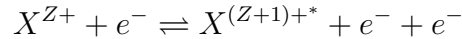


Electron impact excitation is the main process populating low energy levels in the tokamak plasma.

- **Electron impact ionization/three body recombination**

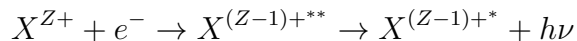
A free energetic electron can collide with a bounded electron and it release the bounded electron. It can happen if the free electron transfers towards the bounded electron enough energy to cause the ionization. Also the inverse process is possible

when two electrons hit the same ion and one of them remains bounded and the second one runs away with the excess energy. However this inversion process is usually negligible in tokamak plasma.



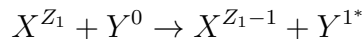
- **Auto-ionization/Dielectronic recombination**

Auto-ionization process is composed from two steps. In the first step two bounded electrons must be excited to higher levels. Then the deexcitation of one electron from this pair can release enough energy to liberate the second one. Inverse process called *dielectronic recombination* can happen only if the fast free electron is captured into double excited state by excitation one of the bounded electrons. After the deexcitation of one of these electrons, the second one can be liberated by autoionize process or one photon with exceed energy can be radiated. If the energy is lost by radiation, it is energetically impossible for an electron to escape and recombination process is finished. The second way is called dielectronic recombination, which is usually a resonance process. The excitation rate of this process for light ions dominates over electron impact excitation at higher energies. Typical examples of the excitation rates are in Fig. 3.2.



- **Charge exchange recombination**

This mechanism causes transfer of a bounded electron between an ion and a atom in collision. This process is typically resonant and it can influence plasma only if the population of neutrals is high enough. Typical sources of the neutrals in tokamak plasma are vessel walls and NBI.



3.3 Plasma models

A theoretical prediction of the radiative behaviour of the ions in the plasma is very complicated. Every process from the previous section can potentially influence the resulting equilibrium populations of excited states and thus the observed radiation. Therefore a few simplified models are used for estimation of the plasma behaviour.

3.3.1 TE (Thermodynamic Equilibrium) model

It is expected that all processes are in the complete *thermal equilibrium* in this model. It means that the rate of each atomic process is exactly balanced to the rate of the inverse process. This situation is called *detailed balance*. Level population distribution is determined from Boltzmann statistics and Saha ionization distribution [27]. The radiation is fully described by Planck law. However, the conditions for this type of equilibrium are rarely fulfilled in any laboratory plasma, because of finite volume of these experiments. The typical example is equilibrium in the interior of the sun.

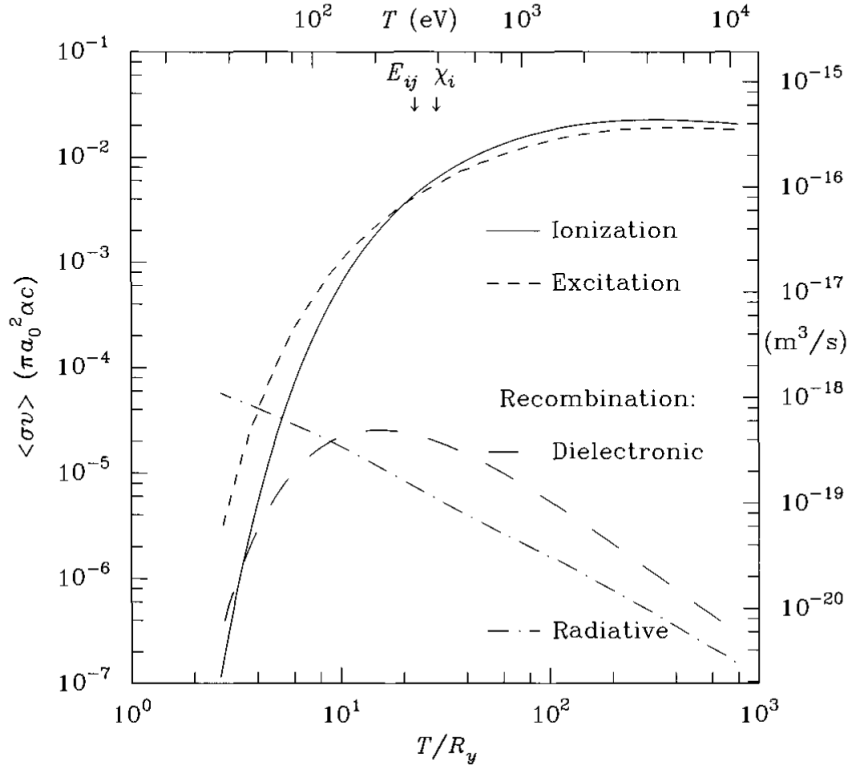


Figure 3.2: An example of the rate coefficient for an excitation and ionization of ion CV [37]

3.3.2 LTE (Local Thermodynamic Equilibrium) model

This type of equilibrium is less restrictive than the TE. The level population is determined by collisions and can be calculated from Boltzmann statistics and Saha ionization distribution, but the radiation is not in detailed balance and can not be determined from Planck law. Radiation must be therefore calculated from atomic transition probabilities.

LTE is typical for low temperature dense plasma. The condition for electron density is [39]

$$n_e \gg 10^{19} T_e^{1/2} \Delta E^3 \quad [\text{m}^{-3}, \text{eV}, \text{eV}].$$

Also this condition is not fulfilled for magnetically confinement plasma. But for high energy levels in ions where is ΔE sufficiently low, it can be valid. These levels are said to be in *partial LTE*.

3.3.3 Coronal model

When the temperature of the plasma is high and density low, the plasma can be described by *coronal model* (typical conditions corona of the Sun). All upward excitations are collisional (due to low light intensity) and downward radiative be spontaneous decay (low electron density). Ionization is also only collisional and recombination is only radiative. For hydrogenic ions the coronal model is valid if [39]

$$n_e \ll 6 \cdot 10^{16} (Z + 1)^6 T_e^{1/2} \exp\left(\frac{0.1(Z + 1)^2}{T_e}\right) \quad [\text{m}^{-3}, \text{eV}]. \quad (3.3.1)$$

Most of the electrons are in the ground level of the ion, probability of cascade excitation to the higher level is negligible. Therefore the higher levels are populated only by collisional process from ground level.

The population of the higher level with respect to ground level can be calculated from rate balance equation.

$$\frac{n_{z,i}}{n_{z,1}} = \frac{n_e \langle \sigma_{1i} v \rangle}{\sum_{j < i} A_{ij}}, \quad (3.3.2)$$

where $n_{z,i}$ is density of ion z in excited state i , $\langle \sigma_{1i} v \rangle$ is excitation rate and A_{ij} is the rate of spontaneous decay from level i to j . Relaxation to equilibrium is very fast, in order of $10 \cdot Z^{-4}$ ns, therefore the time dependence of this process is negligible.

The relaxation time of the ion equilibrium is much slower, for typical magnetically confined fusion plasma about 5 ms [37]. Time-dependent rate equation for the ion population evolution is

$$\frac{dn_z}{dt} = n_e (n_{z+1} \alpha_{z+1} - n_z (S_z - \alpha_z) + n_{z-1} S_{z-1}),$$

where $\alpha_{z+1}(T_e)$ and $S_z(T_e)$ are recombination rate and ionization rate respectively.

If the level population is calculated, the emissivity coefficient for radiation transition between level $i \rightarrow j$

$$\epsilon_{ij} = \frac{1}{4\pi} n_{z,i} A_{z,i \rightarrow j} E_{ij} \quad [\text{W} \cdot \text{m}^{-3} \cdot \text{sr}^{-1}].$$

In the stationary conditions, the emissivity coefficient can be related to ground level of the ion from equation (3.3.2)

$$\epsilon_{ij} = \frac{1}{4\pi} n_e \langle \sigma_{1i} v \rangle n_{z,i} \frac{A_{z,i \rightarrow j}}{\sum_{k < i} A_{z,i \rightarrow k}} E_{ij} \quad [\text{W} \cdot \text{m}^{-3} \cdot \text{sr}^{-1}],$$

dimensionless fraction with ratio of Einstein coefficients is called *branch ratio* and determine fraction of electrons, which deexcite to level j .

Coronal model can be also extended by other processes as dielectronic recombination and charge exchange. These processes can be added to the radiation recombination rate α_Z

$$\alpha'_Z = \alpha_Z + \alpha_Z^{\text{dielc}} + \frac{n_0}{n_e} \alpha_Z^{\text{CX}}.$$

3.3.4 CR (Collisional Radiative) model

Because neither LTE nor CE are fully valid in the magnetically confined plasma, more general model has to be applied. The most general model is called *Collisional Radiative*

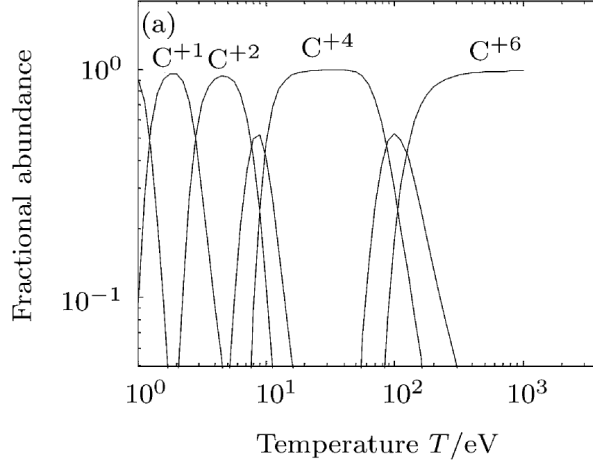


Figure 3.3: The carbon corona equilibrium ionisation state distribution [40].

model. In this model are used full time dependent rate equations for level population of plasma and transport equation for light. General form of the rate equation in cylindrical geometry is

$$\frac{\partial n_{z,i}}{\partial t} + \frac{1}{r} \frac{\partial}{\partial r} (r \Gamma_{z,i}) = R((z, i) \leftarrow) - R((z, i) \rightarrow),$$

where $R((z, i) \leftarrow)$ represent sources of particles in state (z, i) by radiative and collision processes and $R((z, i) \rightarrow)$ represent sinks of the particles in this state. These processes has been already described in sections 3.1 and 3.2. Radial flux of particles is given by

$$\Gamma_{z,i} = -D_{\perp} \frac{\partial n_{z,i}}{\partial r} - n_{z,i} v,$$

where the first term describe perpendicular diffusion and the second term on the right describe an *inward pinch* with velocity v . Typical velocity is about 1 ms^{-1} [41].

Reliability of the computed spectra depends also on the reliability of the atomic data. The most recent and complete data can be found in ADAS database [42]. Also very useful freely accessible tool is FLYCHK [36, 43]. This code can be used through internet and time dependent calculations of the line intensities can be easily realized. The user must only provide some rough idea of the plasma conditions and FLYCH will try to extract as much information and as straightforward as possible. This code has been already used for analyse of the spectra from COMPASS [44].

3.4 Line broadening mechanisms

Not only the line intensities, but also the shape of the observed lines can help with determining conditions in the plasma. General shape of the observed line can be described by its moments. The zero moment is the intensity. The first moment is the unperturbed position plus the shift of line, the second central moment is caused by the line broadening, third central momentum, caused by skewness of the line, can be caused by multiplet broadening, pressure broadening or instrumental function etc. Every higher momentum is less precisely measurable due to unavoidable noise in real data.

In this section different mechanisms causing a line broadening will be investigated.

3.4.1 Natural broadening

The natural width of the line is caused by an exponential dumping of the radiated light during the radiative transition. This broadening effect can be roughly estimated from the formula

$$h\Delta\nu\tau \sim h,$$

where τ is the lifetime of the excited state and $\Delta\nu$ is the observed broadening. The shape of the line is given by the Fourier transform of a exponentially dumped sinus wave, so called *Lorentz shape*

$$L(x; \mu, \gamma) = \frac{\gamma/2}{\pi((x - \mu)^2 + \gamma/2)}$$

However natural broadening is usually negligible, less than 10^{-5} nm.

3.4.2 Doppler broadening

The thermal motion of particles causes so called *Doppler broadening* of spectral lines. The shape of the Doppler broadened lines $f(\lambda_D)$, can be easily calculated

$$f(\lambda_D)d\lambda_D = \tilde{f}(v)\frac{d\lambda_D}{dv}dv = \tilde{f}(v)\frac{c}{\lambda_0}d\lambda_D$$

where λ_D is Doppler shifted wavelength, $\tilde{f}(v)$ is velocity distribution and v is corresponding velocity. For the Maxwell distribution is line shape Gaussian

$$f(\lambda_D) = \tilde{f}\left(\lambda_D\frac{c}{\lambda_0}\right)\frac{c}{\lambda_0} = \sqrt{\frac{mc^2}{2\pi kT\lambda_0^2}}\exp\left(-\frac{mc^2\lambda_D}{2kT\lambda_0^2}\right)$$

and FWHM is

$$\lambda_D = 2.35\lambda_0\sqrt{\frac{T_i[eV]}{m[eV]}} \quad (3.4.1)$$

Doppler broadening is the most important broadening in the low density high temperature plasma in tokamaks. Ion temperature can be measured this way, however if the measurement is non-local, line of sight integrated, analysis of the temperature is significantly more difficult.

3.4.3 Stark broadening

At high density, low temperature plasma, the spectral lines can be broadened by *pressure broadening*. This broadening is caused by interacting of the emitting particles with a surrounding plasma. The radiating particle is influenced by time-varying electrical field from the close particles, which was not shielded by Debye shielding. The calculation of this broadening is quite complicate and different shapes of the line can arise [27].

There are two main approaches for opposite extremes

- *collisional approach*

The atom radiates most of the time unperturbed and occasionally is interrupted by a collision. The duration of the collision is much shorter than the mean time between collisions τ . The collisions are driven by the Poisson statistics and from the Fourier transform of such wave the broadening similar to natural broadening occur. Only instead of the lifetime of excited state, the mean time between collisions is used. This effect is typical for the collisions with electrons.

- *quasistatic approach*

It is assumed, that the time of the collision is longer than period of radiation of atom. The electric field is therefore effectively static during the period of emission. The broadening is therefore caused by Stark splitting of energy levels in atom. Quasistatic approach is used for treating of heavy and slowly moving ions.

From the experiment it follows, that both effect must be accounted. The line width $\Delta\lambda_{1/2}$ for a hydrogen line profile is [45]

$$\Delta\lambda_{1/2} = 2.5 \cdot 10^{-13} \alpha_{1/2} N_e^{2/3}$$

Fortunately this broadening effect is negligible in the tokamak plasma.

3.4.4 Zeeman splitting and Motion Stark effect

In the strong magnetic field splitting of the multiplet lines occurs, due to the Zeeman effect and electric field observed by fast moving particles in strong toroidal magnetic field. In the magnetic field degenerate quantum state with total angular momentum J is split into $2J + 1$ with projections of angular momentum M . Only transitions with $\Delta M = 0, \pm 1$ are allowed. From the perturbation theory in quantum mechanics can be calculated [46], that:

$$\Delta E = Mg\mu_B B$$

It can be simplified by substitution to shape

$$\Delta\lambda = 4.7 \cdot 10^{-8} \lambda^2 MgB[\text{T}] \quad [\text{nm}]$$

where $g(j, l, s)$ is the Landé g -factor and for LS coupling is given by

$$g(j, l, s) = 1 + (g_s - 1) \frac{j(j+1) - l(l+1) + s(s+1)}{2j(j+1)},$$

where $g_s \approx 2$. For the singlet line ($S = 0$) is line split to three components. Unshifted component (π -component) corresponds to $M = 0$ is parallel polarized when is viewed perpendicularly to magnetic field a σ component ($M = \pm 1$) is perpendicularly polarized. When the radiation is observed parallelly to magnetic field, the π component is unpolarized and σ components are circularly polarized.

For the magnetic field in the COMPASS tokamak $B_\phi \approx 1$ T, Zeeman splitting is of CIII triplet ($1s^2 2s 3s^3 S \rightarrow 1s 2s 3p^3 P^0$) is ≈ 0.02 nm which corresponds to CIII temperature about 4.8 eV (Eq. (3.4.1)).

Motion Stark effect is caused by electric field observed by fast neutrals from NBI in magnetic field

$$\mathbf{E}_{\text{motional}} = \mathbf{V} \times \mathbf{B}$$

For the hydrogenic lines is dominant linear Stark effect even for low intensities of E and line shift is

$$\Delta\lambda_S = \frac{3a_0e\lambda^2V_{\text{beam}}}{2hc} \sqrt{B_\phi^2 \sin^2 \Omega + B_\theta^2}$$

a_0 is classical radius of hydrogen Ω is angle between beam and tor. mag. field. The relation between σ and π components is [47]

$$\tan \theta = \sqrt{\frac{2I_\pi}{I_\sigma - I_\pi}},$$

where θ is angle between \mathbf{E} and line of sight.

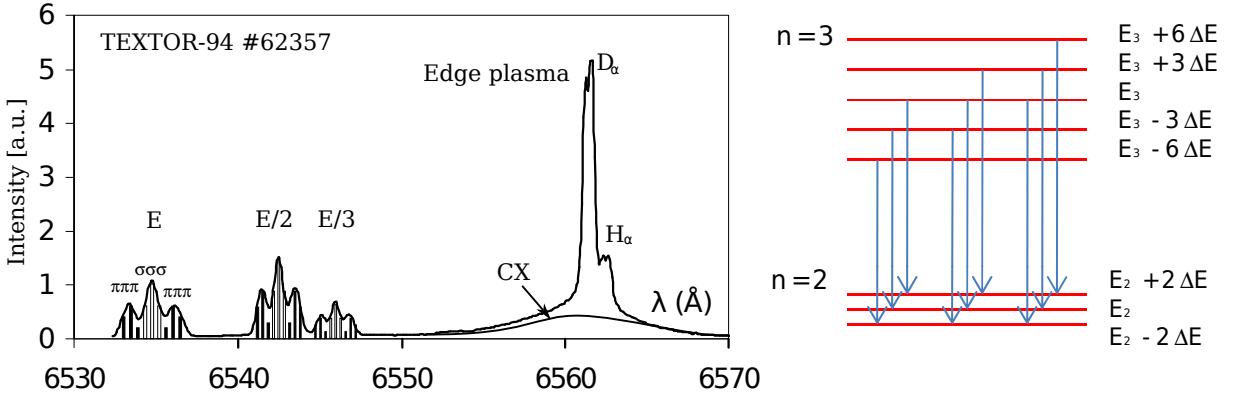


Figure 3.4: Line splitting of hydrogen lines due to Motion Stark effect [48] on NBI beam. The π components of Doppler shifted H_α lines are filled and the σ empty bars.

3.4.5 Instrumental broadening

The previous lines broadening are observable only with spectrometers with very high dispersion. In the common spectrometers the line broadening is mainly influenced by broadening of the device. There are many reasons of this broadening inside the device, for example intrinsic broadening of the grating, focusing, finite width of the slit, etc. The profile of the observed line ϕ_{out} is therefore given by convolution of the input spectra ϕ_{in} and an instrumental broadening function f_i

$$\phi_{out}(y) = (\phi_{in} * f_i)(y) = \int \phi_{in}(y-x)f_i(x)dx \quad (3.4.2)$$

However is is only an approximation suitable for the simple linear detector and wavelength independent instrumental function. For a more general cases must be a more general approach adopted, described in Sec. 5.4.

3.5 Applications in tokamak plasma

Plenty of useful information about the conditions in plasma can be determined from the plasma spectroscopy. The examples of the most common plasma properties which could by measured by spectroscopy are in following list

- **Impurity density:** density of impurities can be estimated from observed lines intensity and from appropriate plasma models, or more precisely with higher spatial resolution by *Charge Exchange Recombination Spectroscopy* (CXRS) on the neutral beams.
- **Effective charge:** The effective ion charge Z_{eff} of plasma can be measured from Bremsstrahlung radiation or directly calculated from impurities densities. Both ways are very difficult to measure and results are usually imprecise.
- **Plasma rotation velocity:** Plasma velocity is measured from Doppler shift of the spectral lines

$$(\mathbf{n} \cdot \mathbf{v}) = c \frac{\Delta\lambda}{\lambda} \quad (3.5.1)$$

where \mathbf{n} is direction of the line of sight. CXRS is usually applied to achieve spatial resolution.

- **Ion temperature:** can be measured from Doppler broadening of the lines

$$\lambda_D = 2.35\lambda_0 \sqrt{\frac{T_i[\text{eV}]}{m[\text{eV}]}} \quad (3.5.2)$$

Also from CXRS the spatial resolution of the measurement can be achieved.

- **Influx of neutrals:** Due to plasma wall interaction the neutrals of the hydrogen are released from the walls. This process is also called fuel recycling. The knowledge of the recycling is necessary for plasma density control. The radiation of the neutrals is given by formula

$$\epsilon_A = \Gamma_A \frac{h\nu}{4\pi} \frac{A_{0,i \rightarrow j}}{\sum_{k < i} A_{0,i \rightarrow k}} \frac{\int n_e(r) n_A(r) \langle \sigma_{exc} v_e \rangle dr}{\int n_e(r) n_A(r) \langle \sigma_{ion} v_e \rangle dr}$$

For a edge of fusion plasma ($n_e < 10^{19} \text{ m}^{-3}$, $T_e = 10 \text{ eV}$) is a sufficient approximation of the H_α line radiation [47]

$$\epsilon_A = \frac{1}{15} \Gamma_A \frac{h\nu}{4\pi} \quad [\text{W} \cdot \text{m}^{-3} \cdot \text{sr}^{-1}] .$$

The passive spectroscopy measurement suffers from one disadvantage typical for plasma measurement. Although the measurement is relatively simple, interpretation of the measurement can be very difficult. A tomographical inversion must be usually applied to achieve limited spatial resolution and because it is ill posed problem, a reliability of the results is sometimes very poor.

With an active spectroscopy for example CXRS, can be achieved more accurate results, but the experimental setup is more complex and also the measurement can perturb plasma.

Chapter 4

Plasma Rotation

In this chapter, basics of the momentum transport theory and neoclassical theory will be explained. It is necessary for understanding to the problems connected with estimation of the plasma rotation. The plasma rotation is very interesting phenomena and a very active topic in fusion research. Some aspect of the plasma rotation are still not fully understood. The rotation play critical role in plasma performance, for example:

- Turbulence suppression ($\mathbf{E} \times \mathbf{B}$ shear)
- Mode stabilisation (RWM, NTM, sawteeth etc.)
- Tolerance to magnetic field errors
- Onset of H-mode and ITB

All these effect are significantly influenced by plasma rotation velocity or the shear of the velocity profile. Because of toroidal symmetry of the tokamak, and if the asymmetrical effect as the toroidal field ripple can be neglected, the canonical toroidal angular momentum in the tokamak is conserved quantity

$$P_\phi = \frac{RB_\perp}{B}mv_\parallel + Ze\psi$$

and due to quasi-neutrality also the total angular momentum is conserved [49]. However in the poloidal direction in the plasma symmetry much weaker and therefore poloidal momentum can be conserved only in the limit of the zero inverse aspect ratio (cylindrical plasma). Because this is not fulfilled in the tokamak, the poloidal rotation is strongly dumped (Sec. 4.3.1).

Rotation can not raise without any external source of momentum. Typical source of the toroidal momentum in the toroidal direction is NBI and in the first experiment where was rotation measured [50] did not expect any other sources. Later was discovered significant influence of the toroidal rotation by neoclassical effects and so called *spontaneous rotation* (Sec. 4.3) was measured. In the recent studies [51] also other sources of the non-diffusion momentum transport was suggested - Coriolis pinch, $E \times B$ shearing, up-down asymmetry, and finite ρ^* effects.

The poloidal rotation is mainly influenced by neoclassical rotation and and strong nondiffusive dumping. However poloidal momentum can be also significantly increased by NBI

and radial current j_r for example from external biasing. Other exceptionally important phenomena influencing poloidal rotation is the H-mode and radial electric field in the pedestal can be evaluated from the radial force balance equation.

The plasma rotation is defined as component of fluid velocity which lies within a flux surfaces and the radial velocity v_r describes slow particle convection $\Gamma_r = m_i n_i v_r$. The rotation velocity is composed from the poloidal v_θ and toroidal v_ϕ component. The main advantage of this description are simplified computations in toroidal symmetry of the tokamak. However, another decompositions can be used, for example decomposition to the direction parallel with helical magnetic field and perpendicular (within the flux surface). This way of the velocity description is more useful from the physical point of the view.

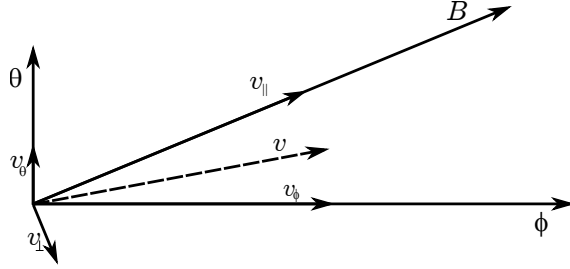


Figure 4.1: Decomposition of the velocity vector v to parallel and perpendicular component (v_{\parallel} and v_{\perp}) and to poloidal and toroidal component (v_{θ} and v_{ϕ})

4.1 Momentum balance equation

From the point of view of the kinetics theory, the plasma is a statistical assembly of a few species of particles interacting with the Coulomb interaction. This statistical assembly can be described by a distribution function $f_{\alpha}(\mathbf{x}, \mathbf{u}, t)$ for each species α that presents in plasma. The time evolution of the assemble is evaluated from the Boltzmann equation

$$\frac{\partial f_{\alpha}}{\partial t} + \mathbf{u}_{\alpha} \nabla_{\mathbf{u}} f_{\alpha} + \frac{\mathbf{F}}{m_{\alpha}} \cdot \nabla f_{\alpha} = \left(\frac{\partial f_{\alpha}}{\partial t} \right)_{\text{coll}}.$$

The evolution of f_{α} is therefore influenced by convection, the external force \mathbf{F} and also by collision term on the right side of the equation. In the plasma, the force term in previous equation is mainly the Lorentz force $\mathbf{F} = \mathbf{E} + \mathbf{u} \times \mathbf{B}$. Moreover, the Maxwell's equations for the time evolution of the magnetic and electric field must be included because the Boltzmann equation does not provide full description of the plasma. On the other hand, the plasma description using the full Boltzmann equation is quite complicated and nontransparent. Therefore, an approximation of the Boltzmann equation based on the solving of the moments is used. The moment of a quantity Q is defined as

$$\langle Q \rangle = \frac{1}{n_{\alpha}} \int Q f_{\alpha} d\mathbf{u}_{\alpha},$$

where n_{α} is particle density

$$n_{\alpha} = \int f_{\alpha} d\mathbf{u}_{\alpha},$$

for the zero moment $Q = 1$ the particle conservation laws and for the first momentum v_α the momentum conservation equation is obtained

$$\frac{dn_\alpha}{dt} = -n_\alpha \nabla \cdot \mathbf{v}_\alpha \quad (4.1.1a)$$

$$m_\alpha n_\alpha \frac{d\mathbf{v}_\alpha}{dt} = n_\alpha q_\alpha (\mathbf{E} + \mathbf{v}_\alpha \times \mathbf{B}) - \nabla \cdot \mathbf{P}_\alpha + \mathbf{R}_\alpha + \mathbf{S}_\alpha, \quad (4.1.1b)$$

where \mathbf{R}_α denotes the momentum transfer due to collisions with other plasma species and \mathbf{S}_α is the momentum source including all external forces applied on plasma. The fluid velocity of species α is defined by

$$\mathbf{v}_\alpha \equiv \langle \mathbf{u}_\alpha \rangle,$$

the pressure tensor is defined:

$$\mathbf{P}_\alpha \equiv n_\alpha m_\alpha \langle (\mathbf{u}_\alpha - \mathbf{v}_\alpha)(\mathbf{u}_\alpha - \mathbf{v}_\alpha) \rangle$$

and the *convective derivation*

$$\frac{d}{dt} = \frac{\partial}{\partial t} + \mathbf{u}_\alpha \cdot \nabla.$$

The system of equations 4.1.1b can be simplified even more by *single fluid* description. It can be obtained by summing of previous equations over all species presented in plasma. The sum of all collisions terms is zero, $\sum_\alpha \mathbf{R}_\alpha = 0$ because of momentum conservation during Coulomb collisions. Summing of these equations leads to a single fluid *momentum balance equation*

$$\rho \frac{d\mathbf{v}}{dt} = \mathbf{j} \times \mathbf{B} - \nabla p - \nabla \cdot \mathbf{\Pi} + \mathbf{S} \quad (4.1.2)$$

and from equation for electrons leads to *generalized Ohm's laws*

$$\mathbf{E} + \mathbf{u} \times \mathbf{B} = \frac{1}{ne} \left(-\frac{m_e}{e} \frac{\partial \mathbf{j}}{\partial t} + \mathbf{j} \times \mathbf{B} - \nabla p_e - \nabla \cdot \mathbf{\Pi}_e + \mathbf{R}_e \right), \quad (4.1.3)$$

the definition of mass m , density n and velocity \mathbf{v} is following:

$$m = \sum_\alpha m_\alpha \quad n = \frac{\sum m_\alpha n_\alpha}{\sum m_\alpha} \quad \mathbf{v} = \frac{\sum m_\alpha n_\alpha \mathbf{v}_\alpha}{\sum m_\alpha n_\alpha},$$

however due to quasi-neutrality $n_i \approx n_e$ and low mass of electron these approximations can be done

$$m \approx m_i \quad \rho \approx nm_i \quad \mathbf{v} \approx \mathbf{v}_i.$$

The pressure tensor \mathbf{P}_α from equation (4.1.1b) was split to scalar pressure and anisotropic part

$$\mathbf{P} = \mathbf{P}_e + \mathbf{P}_i = p \cdot \mathbf{I} + \mathbf{\Pi},$$

the scalar pressure is the function of the temperature and the density, by the state equation of the ideal gas $p = nT$. The anisotropy part of the pressure tensor, so called *viscous stress*

tensor, depends also on the gradients of the velocity and together with convective term in convective derivation d/dt represents term responsible for momentum transport. The terms $\mathbf{\Pi}_e$ and \mathbf{R}_e in generalized Ohm's law are responsible for resistivity of the plasma.

Suppose that plasma is in equilibrium, collisions with electrons are neglectable and the pressure is isotropic ($\mathbf{P} = p \cdot \mathbf{I}$), in the lowest order approximation will be therefore Lorentz force balanced by gradient of pressure

$$n_\alpha q_\alpha (\mathbf{E} + \mathbf{v}_\alpha \times \mathbf{B}) = \nabla p. \quad (4.1.4)$$

This equilibrium is established in the Afvénic timescale (μs). A perpendicular velocity can be found from cross product of these equation with \mathbf{B} ,

$$\mathbf{v}^\perp = \mathbf{v}_{E \times B} + \mathbf{v}^* = \frac{\mathbf{E} \times \mathbf{B}}{B^2} - \frac{1}{qn} \frac{\nabla p \times \mathbf{B}}{B^2}.$$

We can expect mainly the radial electric field E_r because the parallel and cross-field electric field is shortcut by parallel current due to high parallel conductivity of the plasma, therefore the $\mathbf{E} \times \mathbf{B}$ drift can be expressed as:

$$\mathbf{v}_{E \times B} = \frac{1}{B^2} (0, -E_r B_\theta, E_r B_\phi), \quad (4.1.5)$$

the radial electric field causes perpendicular velocity (Fig. 4.1) and *vice versa*. Because the $B_\theta \ll B_\phi$ this rotation has mainly poloidal component. However, the poloidal velocity is almost zero because the it is strongly dumped (section 4.3.1). Therefore the fast parallel rotation velocity appears to compensate for current the poloidal component. Linear map between parallel/perpendicular and toroidal/poloidal component has following form:

$$v_\phi = \frac{1}{B} (v_\parallel B_\phi + v_\perp B_\theta) \quad (4.1.6a)$$

$$v_\theta = \frac{1}{B} (-v_\parallel B_\theta + v_\perp B_\phi). \quad (4.1.6b)$$

If the poloidal velocity is expected to be zero, it can be calculated from (4.1.5) follows that

$$v_\phi = \frac{E_r}{B_\theta} \quad \frac{v_\parallel}{v_\perp} = \frac{B_\phi}{B_\theta},$$

The final rotation profile is however determined by slow dynamics connected with the momentum transport.

4.2 Momentum transport

The estimation of the radial profile of the rotation velocity depends mainly on the momentum sources, radial transport and momentum sinks. The behavior of the momentum balance equation is very similar to the heat conduction equation in toroidal symmetry, a simple linear differential equation. If the sources of sinks are known and diffusion is constant in the first order approximation the solution can be found as a convolution of the Green functions of heat equations with momentum sources/sinks. The first spatial

derivations of the velocity are included in the viscosity term and the only additional term is the momentum convection.

The plasma capability of the toroidal momentum confinement is described by momentum confinement time τ_ϕ

$$\frac{dL_\phi}{dt} = T_\phi(t) - \frac{L_\phi(t)}{\tau_\phi},$$

where $L_\phi = \int \rho v_\theta R dV$ is total toroidal angular momentum, T_ϕ is input toroidal torque. Obviously, this definition very similar to the energy confinement time. This connection is much stronger than only similarity of the formula. The values of τ_ϕ are very close to τ_E in many different plasma regimes, an example of the results from JET are in Fig. 4.2.

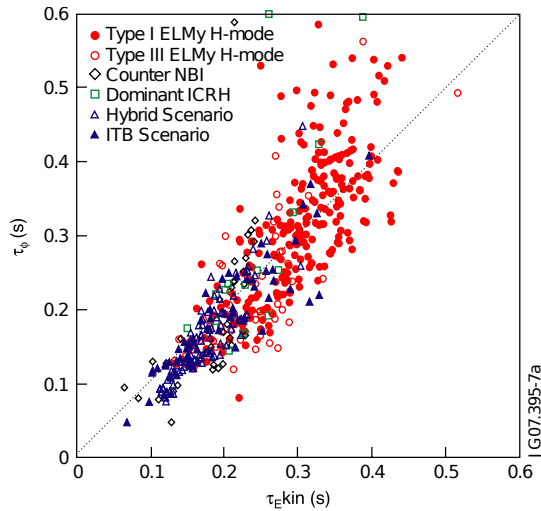


Figure 4.2: Dependency between energy confinement time τ_E and toroidal momentum confinement time τ_ϕ for many different plasma regimes on JET tokamak [52]

4.2.1 Flux surface average

Before any other calculations, it is necessary to explain the concept of the flux surface average. The properties of the plasma on flux surfaces should be constant because of very fast parallel and cross-field diffusion transport. For example, the magnetic flux conservation and gradient of the toroidal field cause non-constant parallel flow, therefore the particles on high field side of tokamak flow faster compared to the low field side. In addition, the value of rotation velocity within flux surface can be unambiguous. Therefore *flux average* must be applied. The definition of the flux averaging is [4]

$$\langle A \rangle_\psi \equiv \lim_{\delta\mathcal{V} \rightarrow 0} \frac{1}{\delta\mathcal{V}} \int_{\delta\mathcal{V}} A d\mathcal{V},$$

where \mathcal{V} is volume between two flux surfaces.

Flux surface averaged toroidal and poloidal velocities V_ϕ and V_θ

$$V_\phi = \langle (B/B_\phi) v_\phi \rangle_\psi \quad V_\theta = \langle (B/B_\phi) v_\theta \rangle_\psi.$$

In the approximation of small inverse aspect ratios $\epsilon \ll 1$, flux surface averaged toroidal and poloidal components of the momentum balance can be estimated [53, 54, 28]

$$m_i n_i \frac{dV_\phi}{dt} = \langle j_r \rangle_\psi B_\theta - \langle (\mathbf{B}_\phi / B^2) \cdot \nabla \cdot \Pi \rangle_\psi B + \langle F_\phi \rangle_\psi \quad (4.2.1a)$$

$$(1 + 2q^2) m_i n_i \frac{dV_\theta}{dt} = -\langle j_r \rangle_\psi B_\phi - \frac{\langle \mathbf{B} \cdot \nabla \cdot \Pi \rangle_\psi}{\Theta B} + \langle F_\theta \rangle_\psi - 2q \langle F_\phi \rangle_\psi \cos \Theta, \quad (4.2.1b)$$

where $\Theta = B_\theta / B_\phi$

4.2.2 Momentum sources and sinks

Short overview of the sources and sinks of momentum in the plasma will be presented in this section. On the right side of the eq. (4.1.2) are four terms responsible for changes of the plasma rotation:

$$\mathbf{j} \times \mathbf{B}, \quad -\nabla p, \quad \nabla \cdot \Pi, \quad \mathbf{S}$$

Only the term ∇p is in radial direction and therefore can not influence plasma rotation. The Lorentz force has a component within the flux surface only if j_r or B_r are present in plasma. In the first case radial electric field E_r cause the radial current j_r and the poloidal force $-j_r B_\phi$ and toroidal force $j_r B_\theta$ arises. If the B_r exists in the plasma, for example from magnetic perturbation coils, it also causes poloidal force $j_\phi B_r$ and toroidal force $j_\theta B_r$.

The viscous tensor Π depends, among other, on the gradient of a velocity. Therefore this tensor is responsible for the radial momentum transport. However it also contains terms from the neoclassical theory which are responsible for so called *intrinsic rotation*. This effect will be discussed in detail in Section 4.3 .

The last term \mathbf{S} contains momentum exchange with outer forces. Examples of such forces are neutral beam or drag force from charge exchange with neutrals at the edge.

Neutral beam

The NBI is usually the most important source of the toroidal momentum in the plasma. The rotation is induced by two different mechanisms.

- Tangentially injected fast neutral particles lost part of their momentum by collisions (friction) with bulk plasma and the rest by charge exchange. This effect influence plasma in the ion-ion collision timescale.
- Part of the particles is after ionization trapped on the banana trajectories. Consequently, net radial current j_r arises due to orbit drift separation between fast ions and electrons. This current, together with the magnetic field, causes torque $\mathbf{j}_r \times \mathbf{B}$ in the perpendicular direction.

The heating neutral beams are usually injected tangentially to maximize path along plasma. Therefore most of the momentum is delivered to the toroidal direction. However

the toroidal force also influences poloidal rotation by term $2q\langle F_\phi \rangle_\psi \cos \Theta$ in Eq. (4.2.1b). The radial density of torque can be roughly estimated from the beam particles energy and the current profile $I(r)$ along the beam in plasma.

$$T(r)dr \approx R \cos \alpha \sqrt{2m_i[\text{eV}]E[\text{eV}]} \frac{1}{e} \frac{dI}{dr} dr,$$

where α is the angle between the beam and toroidal direction. The increase of momentum can be estimated from

$$\Delta L_\phi(r)dr = dMR\Delta V_\phi = (m_i 4\pi^2 a R n_e dr) R \Delta V_\phi = T(r)dr \Delta t$$

in addition, total momentum input and total momentum change can be also calculated

$$2\pi^2 R a^2 \langle n_e \rangle m_i [\text{eV}] \Delta V_\phi / c \approx \cos \alpha \sqrt{2m_i [\text{eV}] E [\text{eV}]} \frac{I}{e} \Delta t.$$

For one NBI for the COMPASS tokamak the acceleration dV_ϕ/dt is 20 (km/s)/ms. The previous formula is valid only for short injections in timescale of milliseconds when the effect of the diffusion transport is negligible.

Charge exchange with neutral atoms

The neutrals at the plasma edge are essentially a momentum sink, because fast particles in plasma is replaced by slow neutral due to the charge exchange and the neutralized fast particles leave plasma with all its momentum. Neutrals velocity is often considered as at rest in the laboratory frame, therefore the drag force is

$$S_{n_0} = -n_i m_i n_0 \langle \sigma_{CX} v \rangle \mathbf{v} = -m_i n_i \nu_0 \mathbf{v},$$

where n_0 is neutrals density, σ_{CX} denotes charge exchange (CX) cross section and ν_0 is CX reaction frequency. This drag force can have significant effect on the poloidal plasma velocity [55].

4.3 Neoclassical rotation

The viscosity and diffusion coefficients necessary to evaluate force balance equation must be determined from theory or measured by dedicated experiment. Transport in toroidal plasma of tokamaks can be described in several ways by classical, neoclassical or transport approach. The classical theory of transport in cylindrical plasma usually significantly underestimates the observed transport. The toroidal shape is taken into account by the neoclassical theory. Nevertheless, the of transport predicted by neoclassical theory is still underestimated and the turbulent transport must be taken in account. Therefore neoclassical transport represents the lowest limit of the transport in tokamaks.

Not only the transport but also a spontaneous rotation was predicted from the neoclassical theory. The spontaneous rotation is very important if other significant sources of momentum (mainly NBI) are present. This effect can be also important if the momentum input from NBI is low. Example of such situation will be NBI system planned for ITER

[56]. Most of the momentum from this NBI will be injected in radial direction and therefore the torque applied on the plasma will be small and intrinsic momentum input exceed momentum input from NBI.

4.3.1 Poloidal velocity dumping

Poloidal flow dumping significantly influence the stationary profile of the poloidal plasma velocity. This effect has two components – collisional and collision-less part. Collisional effect dominants when the poloidal circulation time of particles is longer than the collisional time. A gradient of the toroidal magnetic field is seen by the particle moving in poloidal direction in their rest frame as periodically time-varying magnetic field, higher on HFS and lower at LFS. Because the magnetic moment $\mu = mv_{\perp}^2/2B$ and the energy of these particles must be preserved during their movement, part of the poloidal component of velocity is transferred into the Larmor rotation of the particle. When the particles leave HFS, this part of the velocity is transferred back. Therefore without collisions this effect can not cause poloidal velocity dumping. However, when the particle collide on HFS, the velocity is redistributed nearer to the Maxwell's velocity distribution, plasma is effectively heated and u_{\perp} , μ decreases. When the particle moving back to LFS, it is accelerated again, but the accelerating force $F = -\mu\nabla_{\parallel}B$ is lower than during the previous deacceleration and therefore the mean parallel (poloidal) velocity over a cycle decreases.

If the collisional time is longer than the transition time another dumping effect occurs. This effect is called *transit-time magnetic pumping*. This effect is caused by periodical passing of the particles through a potential well. Principle of the dumping is similar to the Landau dumping of wave [57, 58].

Also the effect of the collisions with the trapped particles is important. The mean poloidal momentum of the trapped particles is zero and because trapped particles represent $\sqrt{\epsilon}$ fraction of the all particles collisions significantly increase the friction.

The poloidal flow dumping is include in the viscous term of the poloidal momentum balance equation

$$\langle(\mathbf{B} \cdot \nabla \Pi)_{\theta}\rangle = \alpha(V_{\theta} - V_{\theta}^{\text{neo}}), \quad (4.3.1)$$

the term α - timescale of the order ion-ion collisional time (about ~ 1 ms), depends on plasma parameters and collisionality regime. The neoclassical predictions for v_{θ}^{neo} and dumping term α are [54, 53]

$$\alpha = \frac{\sqrt{\pi}}{2} \frac{qv_{th}}{R} m_i n_i \quad (\text{Plateau regime}), \quad (4.3.2a)$$

$$V_{\theta}^{\text{neo}} = \frac{K_1}{eB} \frac{dT_i}{dr}, \quad (4.3.2b)$$

other predictions of the term α are summarized in [53]. Calculation of the K_1 coefficient as a function of the normalized collisionality are in [59]. For the banana regime is $K_1 \approx 0.5$, for plateau regime $K_1 \approx 0.5$ and for Pfirsch-Schlüter regime $K_1 \approx -2$. Because the poloidal viscosity (4.3.1) does not contains any radial derivations of the velocity, there is virtually no coupling between poloidal velocities on different flux surfaces. Localized poloidal momentum input will give rise to localized rotation profile. Moreover, the increased poloidal

velocity is exponentially dumped to neoclassical velocity V_θ^{neo} in characteristics time given by

$$\tau = m_i n_i / \alpha.$$

Dependency of the intrinsic poloidal rotation on the gradient of the velocity can be in simplify explained by momentum transferred from trapped particles on banana orbit to passing particles in poloidal direction (Fig. 4.3). Because of the temperature gradient and therefore gradient in collisionality the particle on outer part of the banana orbit transfers its momentum to passing particle with higher probability than the on the inner part of the banana orbit. This and the change of the sign in K_1 coefficient are the reasons why in the banana regime the poloidal rotation is in the ion diamagnetic drift direction and in the Pfirsch-Schlüter regime the rotation is in the electron diamagnetic drift direction.

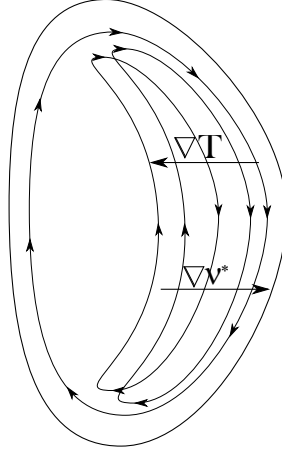


Figure 4.3: An illustration of the intrinsic momentum source caused by radial gradient of friction of trapped ions.

4.3.2 Impurities rotation velocity

In the famous work of Kim and Diamond [59] was provided surprising discovery the rotation velocity of impurities is not same as of the main species. This theoretical calculation was based on the Hirshman and Sigmar *momentum approach* [60]. The explicit expression for velocity difference was also proposed by Kim and summarized with all details in the work of Tesla [61]. Difference between hydrogen and carbon toroidal rotation $\Delta V_\phi = V_{\phi H} - V_{\phi C}$ is:

$$\begin{aligned} \Delta V_\phi &= \frac{v_{\text{th}} \rho_{\theta H}}{4L_{\text{LH}}} \left[K_2 \left(1 - \frac{3B_\phi^2}{\langle B^2 \rangle} \right) - \frac{L_{\text{TH}}}{L_{\text{pH}}} \left(1 - \frac{Z_{\text{H}} T_{\text{C}} L_{\text{pH}}}{Z_{\text{C}} T_{\text{H}} L_{\text{pC}}} \right) \left(1 - \frac{B_\phi^2}{\langle B^2 \rangle} \right) \right] \\ &\approx \frac{K_2}{eB_\theta} \frac{dT}{dr}, \end{aligned} \quad (4.3.3a)$$

where gradient length of some quantity is defined $L_A^{-1} \equiv d \ln A / dr$ (gradient length of temperature and density are negative); thermal velocity $v_{\text{th}} \equiv \sqrt{2T/m}$ and poloidal gyroradius $\rho_{\theta H} \equiv mcv_{\text{th}} / (ZeB_\theta)$.

Also the expression for the poloidal rotation was deduced

$$V_{\theta H} = K_1 \frac{v_{\text{thH}} \rho_{\phi H}}{2L_{\text{TH}}} \frac{|BB_\phi|}{\langle B^2 \rangle} \approx \frac{K_1}{eB_\phi} \frac{dT_i}{dr} \quad (4.3.4a)$$

$$\begin{aligned} \Delta V_\theta &= \frac{v_{\text{thH}} \rho_{\phi H}}{2L_{\text{TH}}} \left[\left(K_1 + \frac{3K_2}{2} \right) - \frac{L_{\text{TH}}}{L_{\text{pH}}} \left(1 - \frac{Z_{\text{H}} T_{\text{C}} L_{\text{pH}}}{Z_{\text{C}} T_{\text{H}} L_{\text{pC}}} \right) \right] \frac{|BB_\phi|}{\langle B^2 \rangle} \\ &\approx \frac{1}{eB_\phi} \frac{dT_i}{dr} \left[\left(K_1 + \frac{3K_2}{2} \right) - \frac{L_{\text{TH}}}{L_{\text{pH}}} \left(1 - \frac{Z_{\text{H}} L_{\text{pH}}}{Z_{\text{C}} L_{\text{pC}}} \right) \right], \end{aligned} \quad (4.3.4b)$$

definition of the toroidal gyroradius is $\rho_{\phi H} \equiv mcv_{\text{th}}/(ZeB_\phi)$ and values of the coefficients $K_1(\nu^*, \epsilon)$, $K_2(\nu^*, \epsilon)$ are in [61, 59]. The physical explanation of this effect is based on the strong coupling of parallel flow of particles by parallel viscosity and weak coupling of the poloidal flow by magnetic pumping, because the magnetic pumping pumps only its own species poloidal flow.

This effect influencing the poloidal rotation is very important at the edge where is a highly collisional plasma.

4.4 Radial electric field

Very important quantity from the point of view of the H-mode bifurcation theories is the edge radial field and the shear of it. The value of the E_r is usually measured indirectly from the poloidal and toroidal plasma rotation. From the radial projection of the force balance equation (4.1.1b) for species α can expressed

$$E_r(r, t) = \frac{1}{eZ^\alpha n^\alpha(r, t)} \frac{dp^\alpha(r, t)}{dr} + V_\theta^\alpha(r, t) B_\phi(r, t) - V_\phi^\alpha(r, t) B_\theta(r, t). \quad (4.4.1)$$

Although the rotation of the impurities can be different from main species, the radial electric field is an overall property common to all the ion species in plasma. Therefore a temperature, density and rotation of arbitrary impurity can be used for measuring of the E_r .

4.5 MHD rotation

Under certain conditions, MHD modes, so called *magnetic islands* or *tearing modes*, can be evolved in plasma. It can happen if the nested flux surfaces breaks up and reconnects. Presence of this MHD modes is indicated by fluctuation in density, temperature and also of the magnetic field. These periodic fluctuations can be easily detected and therefore the question arises: is it possible to estimate plasma rotation from their frequency?

These magnetic perturbations are parallel with magnetic field and therefore only perpendicular rotation is possible. Magnetic field is frozen in plasma, due to very high conductivity of electrons fluid. Therefore, it can be expected that the velocity of the magnetic field is the same as velocity of the plasma without diamagnetic velocity of the electrons

$$\mathbf{v} = \mathbf{v}_{\text{MHD}} - \mathbf{v}_e^*,$$

moreover, the propagation of the MHD modes can be influenced also by ions [62]. The velocity of MHD modes can be experimentally measured from frequency of perturbations. The frequency can be measured for example from Mirnov coils or from SXR AXUV photodiodes. If the toroidal and poloidal numbers of the MHD mode are known, the frequency f_{MHD} follows from:

$$2\pi f_{\text{MHD}} = \mathbf{k} \cdot \mathbf{v}_{\text{MHD}}, \quad (4.5.1)$$

where \mathbf{k} is wave number of the MHD mode

$$\mathbf{k} = -m\boldsymbol{\theta} + n\boldsymbol{\phi} = \frac{m}{r}\mathbf{e}_\theta + \frac{n}{R}\mathbf{e}_\phi$$

this wave number is defined to fulfill condition $\mathbf{k} \cdot \mathbf{B} = 0$ and a requirement of the resonance magnetic surface determined by safety factor q

$$q = \frac{m}{n} \approx \frac{rB_\phi}{RB_\theta},$$

after a substitution to the equation (4.5.1) the frequency is expressed

$$2\pi f_{\text{MHD}} = -\frac{m}{r}v_\theta + \frac{n}{R}v_\phi + \mathbf{k} \cdot \mathbf{v}^*,$$

because $r/R \approx B_\theta/B_\phi \approx v_\theta/v_\phi$, at least one of these velocities must be known to allow calculation of the second one. Only, if the strong toroidal velocities, i.e. induced by momentum input from neutral beams, are present, diamagnetic and poloidal rotation are negligible and the following formula holds

$$v_\phi \approx \frac{1}{n}2\pi f_{\text{MHD}}R.$$

Chapter 5

High dispersion spectrometer

Poloidal rotation at the plasma edge is usually very slow, about 1 km/s. An ion thermal velocity is about ~ 20 km/s, thus it is much faster compared to the rotation velocity. It means that the Doppler broadening of a spectral line is significantly larger than the Doppler shift. Therefore a very careful design of the spectrometer must be the measurement realized.

In this chapter, the high dispersion (HD) spectrometer and all its aspects and issues necessary for analysis of the measured spectra are described in detail. In the first section, the experimental setup, the light detector and finally the light path between the tokamak and spectrometer are described. The following section contains more information about the focusing and alignment of the spectrometer. Finally, in the last section, measurement of the instrumental function and wavelength calibration are investigated and the achievable accuracy are analyzed.

5.1 Experimental setup

A spectrometer designed for measurement of the plasma rotation must fulfil several requirements. The essential requirements are a very high dispersion and maximal stability of the wavelength calibration. Moreover the instrumental function of the spectrometer has to be reasonably narrow. The achieved resolving power ($\Delta\lambda/\lambda$) should be at least 20000 in order to measure the ion temperature about 10 eV. However due to effects caused by inhomogeneity and anisotropy of the light entering the spectrometer, the instrumental function must be as narrow as possible in order to measure tiny Doppler shift.

The high dispersion spectrometer for visible light which was developed for the ISTTOK tokamak in Portugal [30], was used at COMPASS. The spectrometer is designed for observation of a narrow spectral region (~ 2 nm) around wavelength 465.0 nm. This is the region where CIII triplet occurs, which is one of the most intense impurity lines in the tokamak plasma. The example of the observed spectra from COMPASS is given in Fig. 5.1. There can be recognized three lines of CIII triplet but also two oxygen lines are present. In this section description of the spectrometer itself, the light detector and optical path between spectrometer and tokamak will be given.

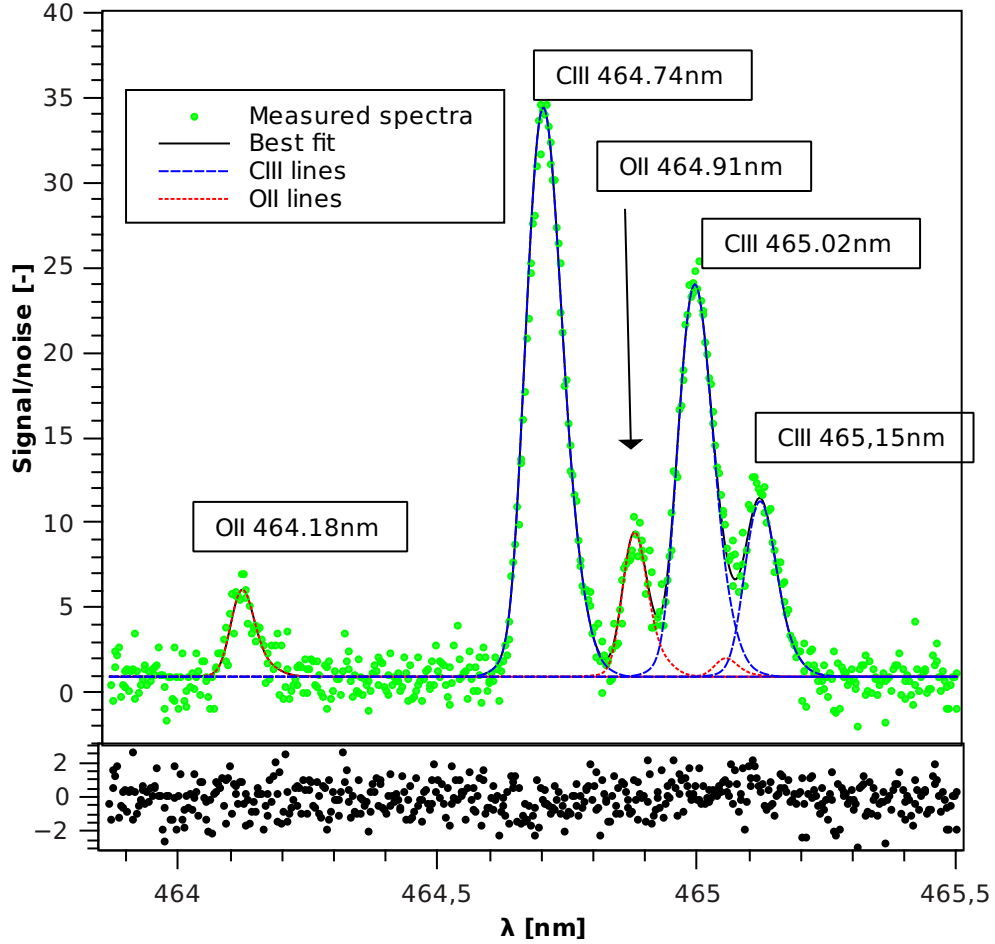


Figure 5.1: An example of the CIII triplet observed by this spectrometer, shot #2901, exposure time 1.3 ms, 30 μm slit, summed two tracks on CCD, $\chi^2/DoF = 1.06$. All of the carbon triplet components are clearly observable and moreover two OII lines are visible.

5.1.1 Description

The spectrometer is based on a double monochromator in an additive dispersion mode [63] using two high density ruled concave diffraction gratings. The scheme of the spectrometer with highlighted optical paths of two close spectral lines is shown in Fig. 5.2. The light from the tokamak is focused by a collecting lens ($f = 50\text{ cm}$, $d = 5\text{ cm}$) to an input slit of variable width ($0 - 500\ \mu\text{m} \times 20\text{ mm}$). The light beam passes through the slit and incidence on the diffraction grating with groove density 2700 grooves/mm, 1 m radius of curvature and area of $60 \times 60\text{ mm}^2$. The numerical aperture (NA) of the whole device is constrained by this first grating and $NA = 0.05$. The slit is situated on the Rowland circle [64] of the first diffraction grating. The Rowland circle is the circle whose diameter is equal to radius of the concave grating, tangential to the surface of the grating and passes through grating the center [63]. The focus of the spectra in the plane perpendicular to the grating and to the grooves, so called *dispersion plane*, is guaranteed in the case that the input and output slit are situated on the Rowland circle. The focus in the perpendicular plane, so called *sagittal plane*, is not generally ensured and therefore astigmatism of second and higher order can be observed. This astigmatism can be reduced using a slightly non-equidistance spacing of the grooves [65, 30].

Instead of the middle slit used in an ordinary double monochromator configuration, a plane

circular mirror with 7 cm radius is used. The plane mirror do not have to be positioned on the cross-section of the Rowland circles, only the total distance between the gratings must fulfill the condition of the Rowland circles. The area of the second grating represents the main limitation of the spectral range of the spectrometer (not of the detector). The spectral range which can be observed without a significant lost of the light is about 5 nm and the maximal observable range is about 10 nm.

The light is refracted from the second grating to a detector that should lay on the Rowland circle too. A cylindrical lens is installed in front of the detector. It is the plano-convex lens with the focal length 50 mm, high 30 mm, width 32 mm, from the N-BK7 substrate and with antireflexive coating. The lens is oriented in sagittal plane in order to fix the astigmatism without influence of the image in the dispersion plane.

5.1.2 Detector

The output light from the spectrometer was collected by a high sensitive camera Andor DU-897E. This camera is equipped by a back illuminated EMCCD (Electron Multiplying Charge Coupled Device) that allows to reach simultaneously low noise and a high time resolution. The resolution of CCD is 512×512 pixels, size of the pixel is $16 \times 16 \mu\text{m}^2$ and size of the detector is $8.2 \times 8.2 \text{mm}^2$.

The CCD chip is divided into two parts: the first is photosensitive for collecting of the light and the second is hidden and serves as a fast storage before the readout. The camera supports on the chip binding of pixels and therefore the SNR¹ and also the reading speed of the camera can be significantly improved by binning of areas of interest (tracks). The thermal noise of the CCD is dramatically reduced by cooling down to -70°C by an inbuilt Peltier element.

The A/D converter resolution is 14 bit for 10 MHz readout speed, and 16 bit for the 1 MHz readout speed. The maximal sensitivity that can be achieved with conventional preamplifier and 1 MHz readout rate is 0.61 count/photoelectron [66] with readout noise RMS (root mean square) 8.9 counts and the quantum efficiency at the 465 nm is 82% [67]. The expected noise and SNR for different camera setting are well explained at [68], therefore only the most important results are resumed here:

- number of counts – n_c

$$n_c = \frac{1}{A} \frac{QE}{100} n + B \quad (5.1.1)$$

- noise in data – σ_c

$$\sigma_c = \sqrt{n_{\text{bin}} \sigma_R^2 + \frac{n_c - B}{\sqrt{A}}} \quad (5.1.2)$$

- signal noise ration – SNR

$$\text{SNR} = \sqrt{n_c - B} \sqrt{\frac{n_{\text{bin}} \sigma_c}{n_c - B} + \frac{1}{\sqrt{A}}} \quad (5.1.3)$$

¹Signal Noise Ratio

where n is the number of photons, A is the CCD sensitivity, QE is the quantum efficiency (82%), B is the nonzero offset of the A/D converter, σ_r is readout noise and n_{bin} is number of tracks binned after readout. The previous formulas were simplified by assumption of conventional preamplifier and negligibility of the background and stray light, background light and dark noise. Precise knowledge of the noise in the observed data is crucial in order to correctly estimate the plasma parameters using the weighted least square fitting of the spectra.

5.1.3 Optical path

The optical path between the bottom and upper port of the tokamak and spectrometer is built from system of the mirrors. A schematic upper projection is shown in Fig. 5.3. The length of the bottom path is 253 cm and the upper path is 344 cm. Currently, only a single path can be used and current path must be switched manually. However when the beam splitter will be available, both optical paths can be used at once.

Apparent advantages of this solution are a lower price, high throughput, and a simple design compared to the optical fibers. On the other hand, the spectrometer has to be installed close to the tokamak in inhospitable conditions unsuitable for such a delicate device. Further, HXR radiation from the runaway electrons incidenting on the CCD detector makes the data evaluation very difficult. A lead shielding was installed, nevertheless a fraction of HXR still penetrates. Also the stray magnetic field and vibration can influence the spectrometer and the optical path in an unexpected way. The last problem arises from anisotropy and inhomogeneity of the light entering the spectrometer. This effect will be discussed in detail in section 5.4.

The second option is installation of the spectrometer to a shielded room. However, the light would have to be transferred from the tokamak by a bundle of optical fibres. The advantage of this option is a higher stability of the spectrometer configuration and an easier wavelength calibration of the spectrometer. Disadvantages are high price of the fibres, lower light throughput and also new optical components would be necessary.

5.2 Focusing of the spectrometer in dispersion plane

Scanning for the best configuration of this spectrometer is an exceptionally difficult problem, which takes hundreds of hours of work often with poor results. The best configuration must fulfil several conditions: the throughput of the spectrometer for light from the CIII triplet must be as high as possible and the shape of the instrumental function must be as narrow and Gaussian as possible.

The position of the gratings are constrained by the *grating equation*

$$m\lambda G = \sin \alpha + \sin \beta, \quad (5.2.1)$$

G denotes the groove density (2700 grooves/mm), m is the diffraction order (the first order in our case) and α, β are angles between the light beam and the normal of the grating. Also the positions the observed spectral range and the last constrain is the desired dispersion. Therefore from the 17 degrees of freedom available in the spectrometer, configuration

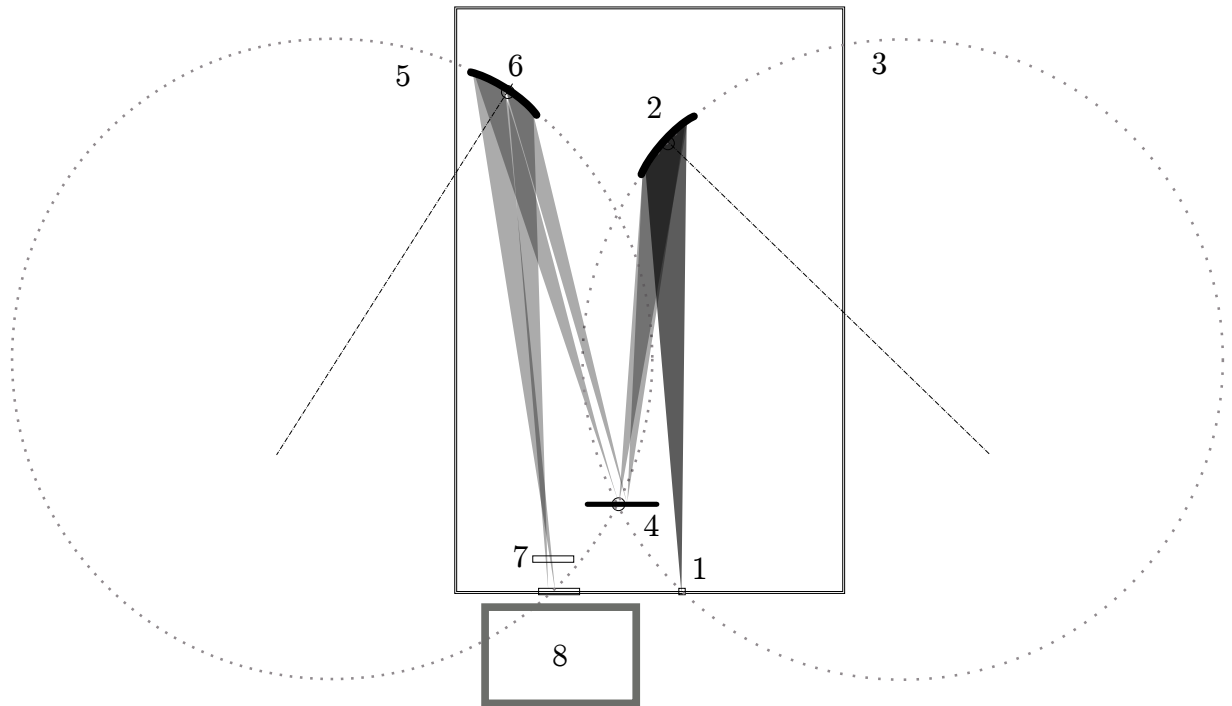


Figure 5.2: The schema of the high dispersion spectrometer; 1 – input slit, 2,6 – concave diffracting gratings, 3,5 – Rowland circles, 7 – cylindrical lens (oriented in the sagittal plane), 8 – EMCCD camera

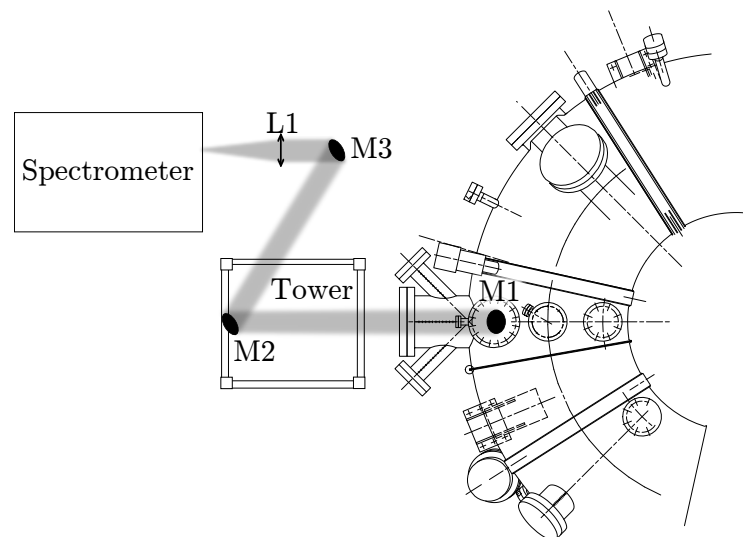


Figure 5.3: The optical path between the tokamak and the spectrometer; M1 – mirror above the top port, M2, M3 – auxiliary mirrors for optical path, L1 – input lens to the spectrometer, Tower – mirrors support structure.

only 4 are almost unconstrained and can be used for the minimizing of the second order aberration – the width of the instrumental function. The condition of the minimal second order aberration is fulfilled on the cross-section of the Rowland circles (the calculation is provided in [63]) and the ray path given by the grating equation (5.2.1). The position of the Rowland circles cannot be measured with the necessary precision and therefore the only option is to propose an algorithm for determination of the optimal configuration of the spectrometer elements.

5.2.1 Focusing as a mathematical problem

The real schema (Fig. 5.3) of the light propagating through spectrometer can be simplified and described by a linear schema shown in Fig. 5.4. The optical properties of the concave gratings are different from the simple system of the lens. For a lens system, it is possible to shift one of the lens so that the whole system will be focused, however the gratings must be focused exactly on the Rowland circle. Close to the optimum, a simpler model can be created based on the assumption that square of the width w of the instrumental function is proportional to sum of squares of differences between the optimal positions (Fig. 5.4) - and current positions x_i of the optical elements. A simplified formula describing the line width w close to the minimum:

$$w^2 \propto \left(C + (L_1 - x_1)^2 + (L_2 + x_1 - (x_3 - L_3) + 2x_2)^2 + (L_4 + x_3 - x_4)^2 \right),$$

the effect of the mirror x_2 position in the second term, is not evident from the linear schema. However from obviously the shift of the mirror in real schema (Fig. 5.3) is the increase of the distance between the first and the second grating.

After a simple substitution the position of the optimum is:

$$\operatorname{argmin} w^2 \propto \operatorname{argmin} \left((y_1)^2 + (y_1 - y_3 + y_2)^2 + (y_3 - y_4)^2 \right) \quad (5.2.2)$$

where y_i represents the *residuum* between the current and the optimal position of the i -th element. Now, if the real physical problem is approximated by this model closely enough, it is necessary to develop a simple iterative optimization algorithm applicable also on the real manual spectrometer setting.

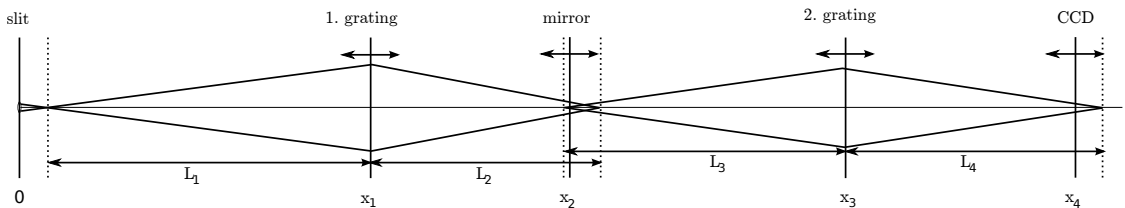


Figure 5.4: The linear schema of the optical components in the spectrometer, cut in the dispersion plane

5.2.2 Optimization algorithms

Only a limited number of optimization operations can be done in a real spectrometer. The simplest task is searching for minimum with respect to each degree of freedom y_i

separately. This procedure can be simply simulated by the model (5.2.2). Lets suppose that the current positions of the optical elements in the spectrometer is defined by a residuum $\mathbf{y} = (y_1, y_2, y_3, y_4)$ between the current position and optimal position. The shifting of a single variable y_i to the optimal position can be described by a linear operator Y_i applied on the vector of current residual positions \mathbf{y} . This operator can be calculated as a derivative of the eq. (5.2.2) with respect to y_i .

$$Y_1 = \begin{pmatrix} 0 & 1/2 & 0 & 0 \\ 0 & 1 & 0 & 0 \\ 0 & 0 & 1 & 0 \\ 0 & 0 & 0 & 1 \end{pmatrix} \quad Y_2 = \begin{pmatrix} 1 & 0 & 0 & 0 \\ 1/2 & 0 & 1/2 & 0 \\ 0 & 0 & 1 & 0 \\ 0 & 0 & 0 & 1 \end{pmatrix}$$

$$Y_3 = \begin{pmatrix} 1 & 0 & 0 & 0 \\ 0 & 1 & 0 & 0 \\ 0 & 1/2 & 0 & 1/2 \\ 0 & 0 & 0 & 1 \end{pmatrix} \quad Y_4 = \begin{pmatrix} 1 & 0 & 0 & 0 \\ 0 & 1 & 0 & 0 \\ 0 & 0 & 1 & 0 \\ 0 & 0 & 1 & 0 \end{pmatrix}$$

These operators have interesting commutative properties: if these operators are applied on the unknown “state” of the spectrometer \mathbf{y} in random order, the asymptotic behaviour is independent of their order. The dynamic of this system is very similar to the dynamic of the random unitary networks [69].

The simplest algorithm for searching of the minimum is therefore an iterative application of these operators on the current state; in reality it is equivalent to iterative focusing of every single optical element separately. This operator is obviously a contraction map, the idea of this algorithm is very close to the idea of the *Gauss–Seidel method* [70]. The current state very quickly converge to the eigenvector with the highest eigenvalue, for the model case (5.2.2) is the eigenvector (0.25, 0.43, 0.6, 0.6) corresponding to the highest eigenvalue 0.85. And the resulting iterative convergence is very slow. An example for the initial state (1, 1, 1, 1) is

	y_1	y_2	y_3	y_4
1. step	1	1	1	1
2. step	1/2	1	1	1
3. step	1/2	3/4	1	1
4. step	1/2	3/4	7/8	1
5. step	3/8	3/4	7/8	1
6. step	3/8	5/8	7/8	1
7. step	3/8	5/8	7/8	7/8
8. step	5/16	5/8	7/8	7/8

After 8 single element focusing, roughly 2 full calibration cycles, the changes are very small but the result is still far from the minimum (0, 0, 0, 0). Very similar behavior was observed during the manual calibration. From the point of view of the real spectrometer focusing, the described behavior is very similar to getting stuck at the local minimum. With the precision achievable in the measurement of the line width, any small position changes cause virtually an increases of the width.

Therefore other algorithm was proposed. Instead of the shifting the state to the minimum in the current dimension, the minimum state will be “overshooting”. The idea is similar

to the *successive over-relaxation method* [71]. Instead of the operators Y_i , an operator $I + \omega(Y_i - I)$ will be used, where ω denotes the relaxation factor determining how much must by optimal value “overshoot”. The optimal value of ω was found numerically as a ω_{opt} that minimize the largest eigenvalue of the asymptotic operator. (Fig. 5.5). The optimal value is close to $\omega_{\text{opt}} = 1.5$, but it is advantageous choose the little higher than the lower value. The residuum can be decreased $10\times$ by application of the 12 full focusing cycles by the first algorithm or by 3 full cycles by the second one. In fact due to the limited precision achievable in the reality and longer steps than in previous example it is not possible to make more than 3 full cycles.

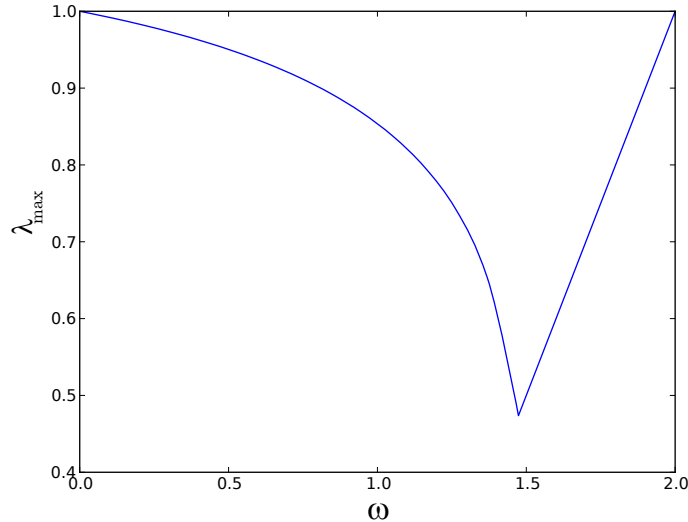


Figure 5.5: An example of the dependence of the eigenvalue λ_{max} on the “overshoot” parameter ω , optimal value ω_{opt} is 1.48

This algorithm was also tested on the real device and if the setup is close enough to the optimal position, the convergence is very fast. However, if the optimal position is too far, this algorithm fails and the optimal position must be searched more or less randomly and success depends mostly only on experiences of the working person. The focusing is considerably complicated by the fact that the process is not monotonic and the process has many seeming local minima.

Also other algorithms were tested, for example an adapted version of the gradient descent method, but these methods usually fails on the imprecise measurement of the local derivations of the instrumental function width.

5.2.3 Focusing on the position of the CIII triplet

The careful focusing of on a intensive calibration line is a very slow procedure. However a calibration on the CIII triplet is even more complicated because any strong line from available lamp was not in the measured wavelength range. Only a limited number of spectral lamps could be used for the calibration.

List of them with the advantages and disadvantages is in the following table:

lamp	lines [nm]	disadvantages	advantages
Zn	462.98; 468.01	out of range	visible by a naked eye
Fe+Ne	464.54; 465.64	life time 200 h, many weak lines	usable intensity
Ne	464.54; 465.64	low power	lifetime 15000 h
Cu	465.11	not available	higher intensity[72] one of the 4 strongest of Cu in VIS

and the positions of these lines with respect to the CIII triplet are in Fig. 5.6.

Majority of the calibration was done using a zinc calibration lamp, because the line at 468.01 nm is visible by a naked eye and this property is very useful for a rough alignment of the optical elements. However if the spectrometer is precisely focused on this zinc line, the focus at the position of the CIII triplet is poor.

The Ne and Fe+Ne hollow cathode lamp for the final stage of the focusing was used. Lines of the iron are extremely weak but also the neon lines are very weak and their measurement is very demanding on the background light intensity in the place of calibration. Moreover due to a limited lifetime about 200 hours, this hollow cathode lamp can be used only for the focusing, not for the long term routine measurements as a reference source. On the contrary, the available weak neon lamp can be hardly used for the calibration, because the necessary exposure time was about 15 minute. But with a lifetime about 25000 hours it is a ideal source for recalibration between the discharges.

5.3 Focusing of the spectrometer in the sagittal plane

The focal length in the sagittal plane (the plane parallel with the grooves and perpendicular to the grating) is usually different from the focal length in dispersion plane. This problem is usually solved using a slightly non-equidistant grooves distance [63]. The grooves distance of the our concave grating is given by the following formula [30]

$$d(y) = d_0(1 + 9.75 \cdot 10^{-6}y + 4.34 \cdot 10^{-7}y^2).$$

In this formula, d_0 denotes spacing of the grooves in the middle of the grating and y is a position in the direction perpendicular to the grooves.

Nevertheless, the light was not focused on our CCD in the sagittal plane. Therefore the plano-convex lens with the focal length 50mm was placed before the CCD. This lens provides three advantages:

- light is focused and it is possible to measure the radiation characteristics with radial resolution
- the light intensity is increased by shrinking of the image size to a smaller size than the height of the CCD
- it should be possible to focus the light from top and bottom port together on the top and bottom halves of the CCD.

However, the light from the plasma cannot be ideally focused on the detector, because the plasma is a volume light source. Therefore the spectrometer was focused to infinity and the line of sight will be represented by back projection of the binned track selected on the detector.

5.4 Instrumental function

The instrumental function determines the relationship between the spectral profile of a line entering the spectrometer and line profile observed by the detector. The precise knowledge of the instrumental function is crucial in order to reach a very precise and accurate measurement of the Doppler shift. The correct model function for the least squares fit is afterwards calculated. Precision on the statistical limits given by signal noise ration (SNR) of the spectra cannot be reached without precise knowledge of the instrumental function. This issue was already investigated in [68] in detail. A numerical simulation of the effects caused by the imprecise model function is shown in the graph 5.7. It follows that a more accurate measurement of the instrumental function allows to achieve a higher precision or a shorter integration time.

5.4.1 The definition

In the usually investigated spectrometers the monochromatic light from a cold spectral source incoming to the spectrometer is projected to the output focal plane as the Gaussian or Voigt profile in the dispersion plane. This line shape is usually constant for wavelengths in the range of the spectrometer. This profile is called the *instrumental function* and we will denoted it by ϕ . Due to the principle of superposition the observed shape of f_r of some line f_λ is given by the convolution

$$f_r = \phi * f_\lambda$$

However, if a very high accuracy is required, another more general approach must be adopted. Lets suppose one ideal ray of monochromatic light entering to the spectrometer. This ray can be described by two angles θ , ϕ a two coordinates ξ , ψ describing the direction and the point when it enters to the slit of a finite width. If the broadening that is caused by the intrinsic resolution of the grating can be neglected (about 0.0025 nm \approx 1 px on the CCD in this spectrometer), this ray is projected on the output plane of the spectrometer as a single point. This ray can be described by its density

$$p_0 \equiv p_{\phi_0\theta_0\xi_0\psi_0\lambda_0}(\phi, \theta, \xi, \psi, \lambda) = \delta(\phi - \phi_0, \theta - \theta_0, \xi - \xi_0, \psi - \psi_0, \lambda - \lambda_0)$$

and the density of the projection is analogously

$$\pi_0(x, y) = \delta(x - x_0, y - y_0)$$

and the spectrometer can represented by the following liner map

$$\mathcal{S}(p_0) \equiv \pi_0 \longleftrightarrow S(\phi_0, \theta_0, \xi_0, \psi_0, \lambda_0) = (x_0, y_0)$$

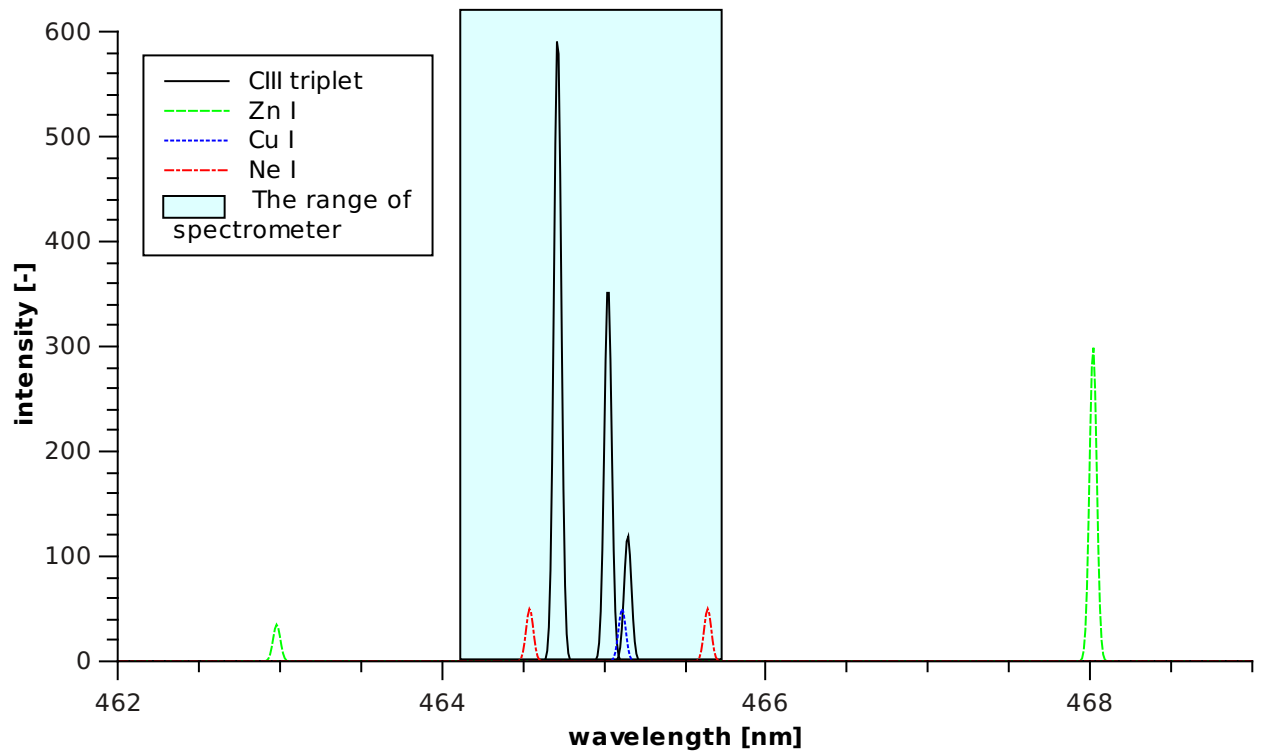


Figure 5.6: Lines of the CIII triplet and the close lines which can be used for calibration - Zc, Cu, Ne lines

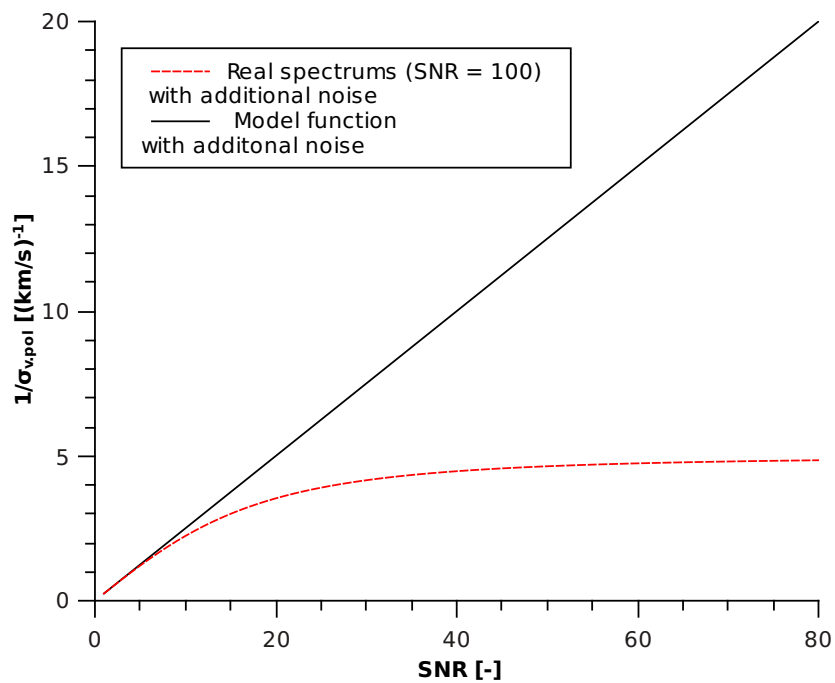


Figure 5.7: The result of the Monte Carlo simulation of the effect caused by an imprecise model (instrumental) function. The theoretical precision is inversely proportional to SNR, however it is only a lower limit of the achievable precision in the real case.

where S is a map in the coordinate space and the kernel of the map is denoted \mathcal{S} . Because of the principle of superposition (in another words due to linearity of the map \mathcal{S}) a real light beam with the density $p(\phi, \theta, \xi, \psi, \lambda)$ entering to the spectrometer can be split into the monochromatic rays and mapped to the output plane of the spectrometer

$$p = \int \langle p_0 | p \rangle |p_0\rangle d\phi_0 d\theta_0 d\xi_0 d\psi_0 d\lambda_0$$

$$\mathcal{S}(p) = \int \langle p_0 | p \rangle \mathcal{S} |p_0\rangle d\phi_0 d\theta_0 d\xi_0 d\psi_0 d\lambda_0 = \int \langle \mathcal{S}^{-1} \pi_0 | p \rangle | \pi_0 \rangle |S|^{-1} dx_0 dy_0$$

It is possible to define a generalized instrumental function for a wavelength λ as $\mathcal{S}(p_\lambda)$, where p_λ is monochromatic light entering to the spectrometer with a specific angular and spatial distribution. Because this definition is obviously unambiguous and strongly depends on the distribution of the entering light, a better definition could be achieved under the assumption that the p_λ is monochromatic, isotropic and homogeneous light.

The consequence is that in the worst case the uncertainty in the line shift caused by unsatisfying the previous conditions would be equal to the width of the instrumental function. In the spectrometer, the maximal error corresponds to the velocity more than 10 km/s. This effect was smaller in our real measurements but still significant. It is also reason why the input slit of the spectrometer should be set as narrow as possible in order to minimize the instrumental function.

5.4.2 Measurement of the instrumental function

Measurement of the two dimensional instrumental function is not trivial, because the same spatial distribution for the calibration light as for the real plasma measurement must be ensured. In the ideal case, the light used for the measurement of the instrumental function is obtained from a cold calibration source. The area of our calibration sources is much smaller than the size and volume of the observed plasma. Therefore a diffusion filter of a proper size was placed in front of the calibration source. However, the consequent decrease of the light intensity prevents to measure the already substantially weak calibration lines. If the diffusion filter is placed at the tokamak port and the lamp is placed to the opposite port, the light intensity is decreased about 3 order of magnitudes and the integration time must be prolonged to more than a week of a continuous measurement in order to achieve sufficiently high SNR. Moreover, due to a slow temperature drift of the calibration line, this measurement cannot be successful. This drift is mentioned in detail in Section 5.6.

Although the measurement of the full 2D instrumental function is not possible with our equipment, the measurement of the 1D fully vertically binned instrumental function was successful and an example of the measurements for a 200 μm width slit is in Fig. 5.8. Nevertheless, a careful statistical analysis of a least square fits of the real spectra from plasma shows that this instrumental function does not estimate the real instrumental function of the plasma with the necessary accuracy. A typical sign is a significant contrast between the sum of squares of the residuum from weighted least square fit of the spectra and statistical χ^2 distribution.

Therefore, another approaches for measuring the instrumental function were tested. The best results were achieved with the instrumental function measured directly using the

CIII triplet radiation from the plasma. When the plasma is very cold, about 10 eV, for example at the beginning of the discharge or during the discharge after discharge². The measured line shape $\tilde{\phi}$ is given by convolution

$$\tilde{\phi} = \phi * f_{\lambda}(T_{\min}) \quad (5.4.1)$$

where ϕ is a real instrumental function and $\tilde{\phi}$ is an instrumental function convoluted with the cold CIII triplet line $f_{\lambda}(T_{\min})$ with the lowest measured temperature T_{\min} . The final model function for the least squares fit f_m is calculated as

$$f_m = \tilde{\phi} * f_{\lambda}(T - T_{\min})$$

for CIII line. The same method can be used for other elements (i.e oxygen,..) but the temperature must be calculated from the eq. (3.4.1) with the corresponding value of the atomic mass. An estimation of the instrumental function $\tilde{\phi}$ measured using the proposed way is shown in Fig. 5.9.

However, even this solution is not ideal because the Doppler shift, radiation distribution and temperature profile at the plasma start is included in such an instrumental function. The only really correct solution can be the installation of the optical fibres because the optical fibre serves also as a light mixing element. The angular distribution of the output light is independent of the angular distribution of the incoming light. Therefore, the light from the calibration lamp will have the same distribution as the light from the plasma and all necessary conditions for the measurement of the real instrumental function will be fulfilled.

5.5 Wavelength calibration

The very slow poloidal plasma rotation at the plasma edge cannot be measured without an exceptionally accurate and precise wavelength calibration. The wavelength calibration was made in two different ways: using the differential Doppler spectroscopy and using a reference line. Unfortunately, each of the method has some disadvantages.

5.5.1 Differential Doppler spectroscopy line

The differential Doppler spectroscopy is based on the idea of measurement the blue and red Doppler shift at once from the bottom and top port. It avoids requirement of any reference line. This method was used for example on the TEXTOR tokamak [28]. It is planned to place the beam splitter between the light beams from upper and bottom port. The light from the ports should be incidenting on different parts of the input slit and consequently it should be focused on different parts of the CCD.

Because the beam splitter is not available yet, this measurement was performed by changing a position of a mirror between discharges. However, this approach was proved to be useless [68] and new measurements confirmed this conclusion. An example of the measurement is in Fig. 5.10. The shots 2634–2636 were measured from the bottom port and

²A few tens of millisecond after the disruption sometimes very cold and rarefied plasma can be observed where most of the radiation comes from helium, however the CIII is detectable.

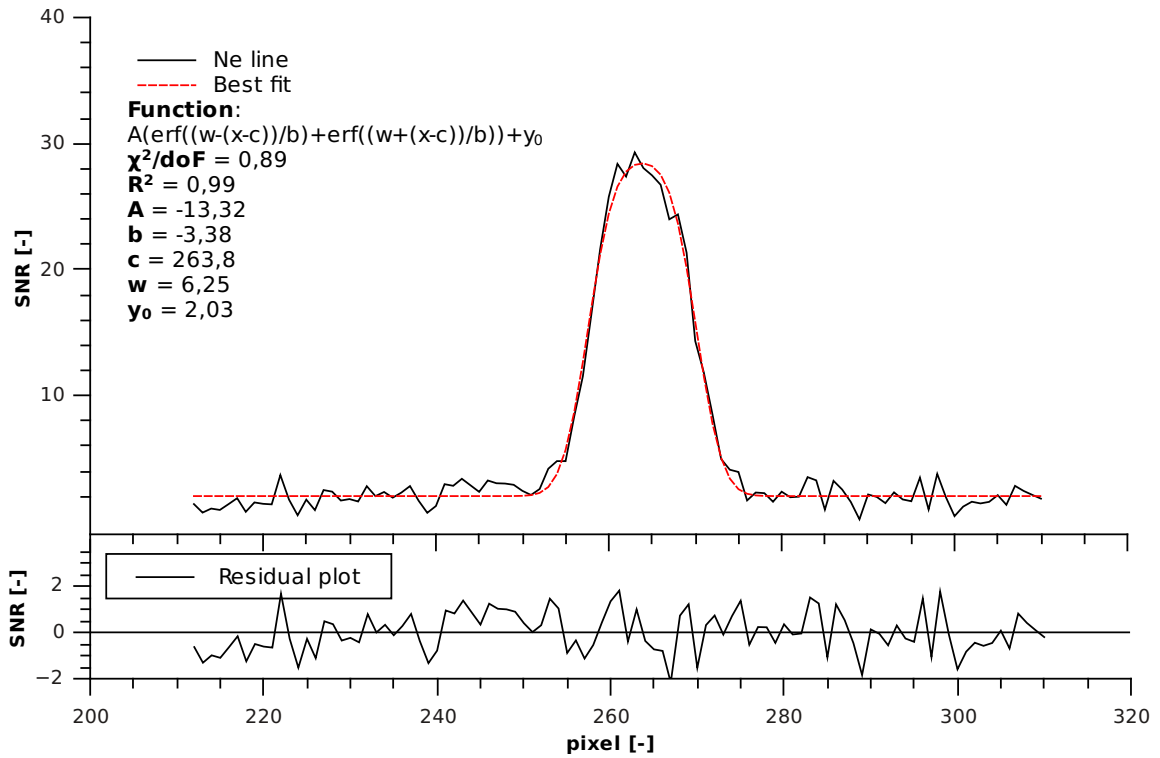


Figure 5.8: Instrumental function measured from the fully vertically binned spectra of the neon lamp and using a $200 \mu\text{m}$ wide slit

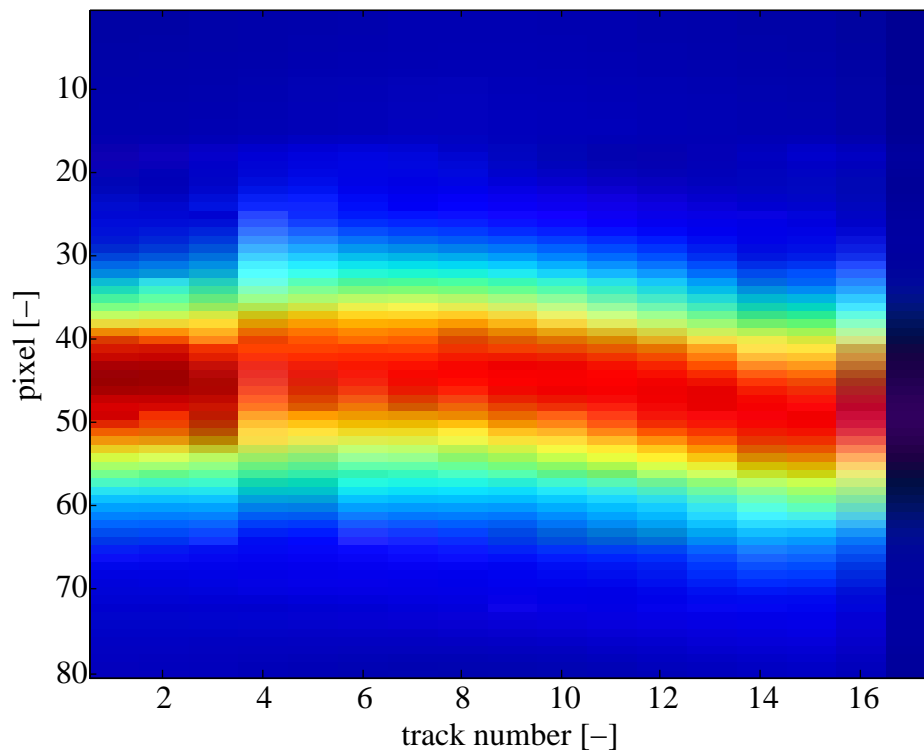


Figure 5.9: The estimated shape from eq. (5.4.1) of the instrumental function over 16 tracks measured from a cold CIII line using a $30 \mu\text{m}$ wide slit

shots 2039–2041 from the top port. The shift of the lines should be reflection symmetric around the zero position, whereas the observed profiles are identical only a little shifted. Moreover the shift of the discharge 2634 is significantly different from the other discharges that used the bottom port. The most probable explanation is that the shift is caused by the radial position of the plasma column and this effect was increased by an imperfectly focused spectrometer (Sec. 5.4.1).

The only advantage of the differential Doppler spectroscopy should be twice larger Doppler shift. However this effect is compensated by the decrease of the light to half by beam splitter so from the statistical precision should be preserved. The velocity error σ_v as a function of the precision of the fit of the peaks σ_{s_1} , σ_{s_2} is

$$\sigma_v = v \sqrt{\left(\frac{\sigma_d}{d}\right)^2 + \frac{\sigma_{s_1}^2 + \sigma_{s_2}^2}{(2\Delta)^2}} \approx \frac{v}{\sqrt{2}} \frac{\sigma_s}{|\Delta|} \approx \frac{c}{\nu} \frac{\sigma_s}{\sqrt{2}} \quad (5.5.1)$$

where d , σ_d are dispersion and its uncertainty, Δ denotes the observed shift, ν is wavelength and c speed of light. However because of decrease of the light intensity to one half, the σ_s increase $\sqrt{2}$ times.

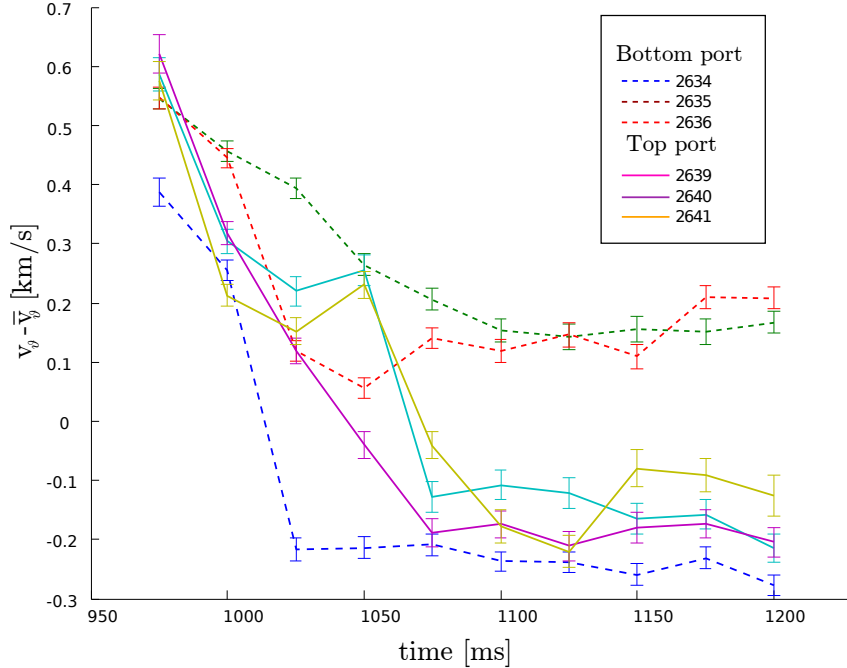


Figure 5.10: Line shift observed by the differential Doppler spectroscopy from top and bottom port separately. The errorbars represents only the statistical precision.

On the other hand, the credibility of this measurement can be improved using the optical fibre similarly to the measurement of the instrumental function. The first option is an installation of two fibres at opposite part of the slit. Unfortunately, because it is not possible to ensure the instrumental function perpendicular to the dispersion plane with the necessary precision (<1 px), there will be always an unknown offset between these two projected images of the line on the CCD causing an artificial shift.

5.5.2 Reference line

A reference line is commonly applied for the wavelength calibration for example at the TCV and NSTX [29, 72]. The statistical precision of such a measurement is the same as for the the Doppler differential spectroscopy

$$\sigma_v = v \sqrt{\left(\frac{\sigma_d}{d}\right)^2 \left(1 + \left(\frac{\Delta_r}{\Delta}\right)^2\right) + \frac{\sigma_r^2 + \sigma_s^2}{(\Delta)^2}} \approx \frac{c}{\nu} \sqrt{\sigma_s^2 + \left(\frac{\sigma_d}{d}\right)^2 \Delta_r^2} \quad (5.5.2)$$

where σ_v is statistical precision of the velocity, Δ is the Doppler shift, Δ_r is distance between reference line and the current line. If the reference line is close enough to the CIII triplet and the dispersion d is measured with successfully precision, the velocity precision σ_v is the same as in the previous section with differential Doppler spectroscopy.

As a reference line was used a weak neon lamp. An example of the neon spectrum is shown in Fig. 5.11 and the neon lines in the range of the spectrometer is in Fig. 5.6.2. The measurement of these lines is extremely demanding on the stray and background light level. More than 99.999% of the light coming from the neon lamp must be absorbed in the spectrometer and the rest, less than 0.001%, is detected. The spectrometer was therefore improved by collimator installed before the camera and a barrier to improve absorption of the zero order reflection from the first grating.

The background light was suppressed by very careful sealing of all holes in the spectrometer and around the camera. The level of the background light was decreased 1300× compared to the previous configuration. The results of the best configuration are shown in the Fig. 5.13. In spite of all these improvement the necessary integration time was 10 minutes. The repetition rate of the COMPASS tokamak is 15–60 minutes, therefore the position of the reference line can be measured between the discharges.

This method suffers with the same issues as the instrumental function measurements. Furthermore, the false shifts caused by plasma movements cannot be determined or removed this way. In spite of this, the reference line is very important for the determination of the spontaneous drift of the lines position caused by thermal drift and slow relaxation of the metal parts of the spectrometer.

5.5.3 Other ways

Also other, less direct, ways has been tried in order to estimate of the zero velocity position. The first of them which was unsuccessfully tested is based on the formula for the Doppler shift (3.5.1)

$$\Delta\lambda = \lambda \frac{v_\theta}{c} \cos \alpha$$

if the zero velocity position λ_0 and poloidal velocity v_θ are constant in radius, the expression for λ_0 is

$$\lambda_0 = \lambda(\alpha) \left(1 - \frac{v_\theta}{c} \cos \alpha\right)$$

An example of the observed Doppler shift and $\cos \alpha$ calculate from radial component of the plasma position in shot #2606 is in Fig. 5.14 when was this effect increased by poor

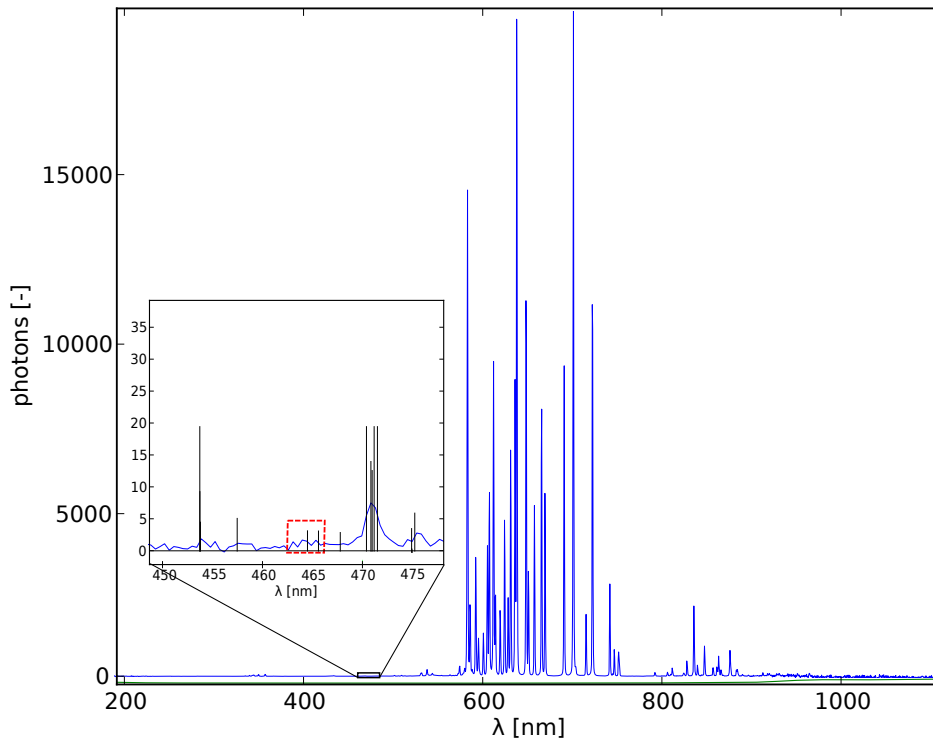


Figure 5.11: The position of the neon line used as the reference line. The line at 464.5 nm should be in the middle of the red dashed square which represents range of the CIII spectrometer. This spectrum was observed using Ocean optics spectrometer and the dynamics range of this spectrometer was improved by averaging of the 1000 spectra with 2 ms integration time.

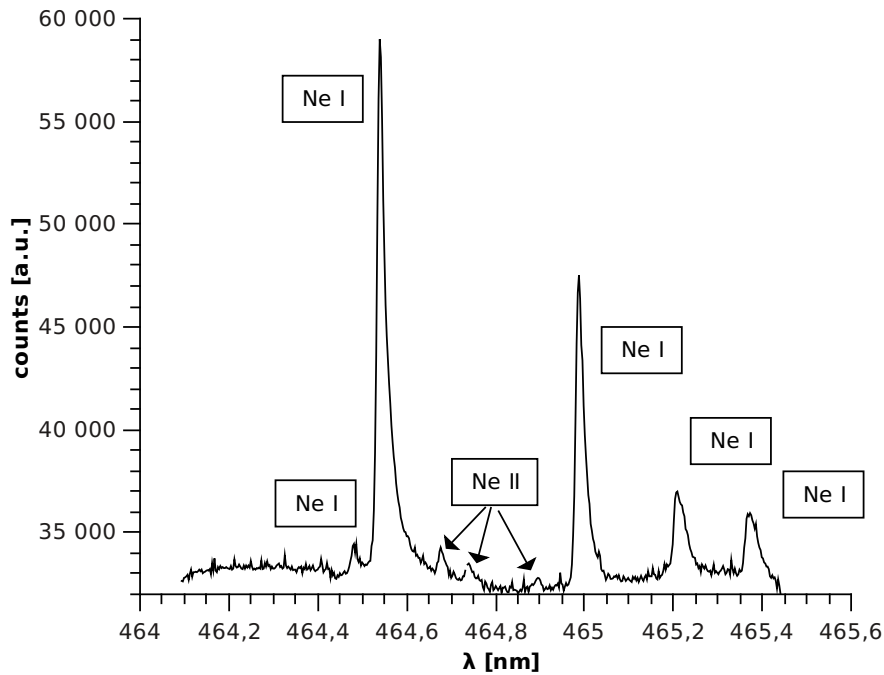


Figure 5.12: Neon lines from the weak neon lamp observed by CIII spectrometer. The result was achieved by averaging spectra from 12 hour integration with $30 \mu\text{m}$ width slit.

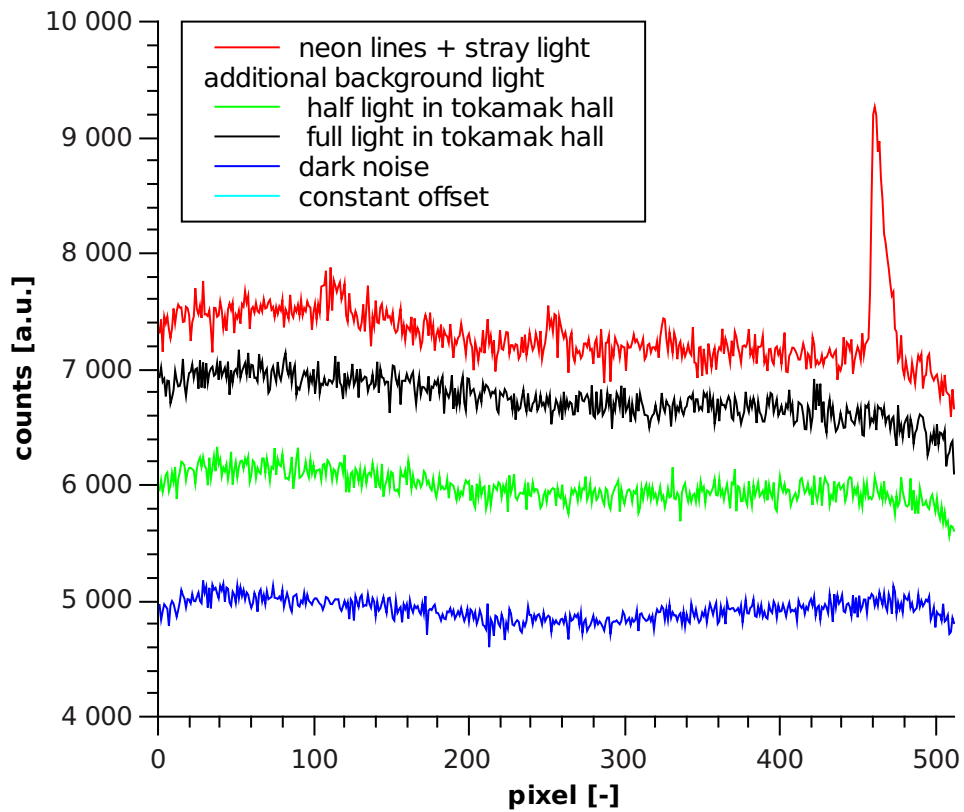


Figure 5.13: Light intensity measured using 100 s exposure. The level 4000 corresponds to a constant offset of A/D converter on CCD, the lowest noise level corresponds to closed shutter on camera, the two higher corresponds to half and fully turned on light in the tokamak hall with opened slit and finally the highest noise level corresponds to the stray light from the neon lamp, you can see the Ne line.

focus. In the better focused shots was this effect significantly reduced. The corresponding poloidal velocity would be about 10 km/s which is much more than the neoclassical predictions of intrinsic rotation that is approximately 1 km/s. The simplest explanation is that the position of the λ_0 is not constant on the CCD and it depends on the current radial position of the plasma as well.

5.6 Limits of the achievable accuracy

Uncertainty of the measurement is determined by two its components: statistical uncertainty and the systematic uncertainty. The statistical error is possible to estimate from a careful analysis of the weighted least square fit of the data (the details about the applied algorithm are in [68]), whereas the estimation of the systematic error is a very difficult problem.

5.6.1 Statistical uncertainty

The statistical noise in the data was determined from formula (5.1.2). In the main peak the readout noise is exceeded by shot noise caused by variation in photon flow described by Poisson statistics. The uncertainty is therefore proportional to square root of the number of counts

$$\sigma \propto \sqrt{n_c}. \quad (5.6.1)$$

The effect of this random noise for the model and real data is shown in Fig.5.7.

The statistical uncertainty represents the lowest limit of the achievable precision. Therefore it is important to identify ways how can be all other uncertainty sources decreased.

The first way is obviously increasing of the photon flow density incidenting the detector. It can be done using a longer integration time, increased slit width and better focus. The signal noise ratio is proportional to the square root of the integration time and to the slit width, due to the dependency in Eq. 5.6.1. Typically achieved SNR is 40 under typical plasma conditions and statistical precision is 0.1 – 0.3 km/s.

The main complication in the statistical evaluating of the data is the “noise” caused by the HXR radiation. This radiation can corrupt a significant fraction of the observed pixels of the image. Although, sophisticate algorithms were developed [68] and a thick lead shielding around the camera was installed, it is not possible to measure the plasma rotation in the case of the low density plasma where significant number of runaway electrons is usually created.

One of the tested ways, how to improve spectrometer parameters, was an increase of the dispersion. The effect of the dispersion on the statistical uncertainty can be easily investigated. Lets suppose that the dispersion was decreased two times. This assumption is done only because than a more clear calculation can be make. The decreasing of the dispersion is equivalent to the binning over two pixels. The uncertainty is based on the least square method, which represents a map F from data x_i to parameters of the model θ_j

$$\theta_j = F(x_i)$$

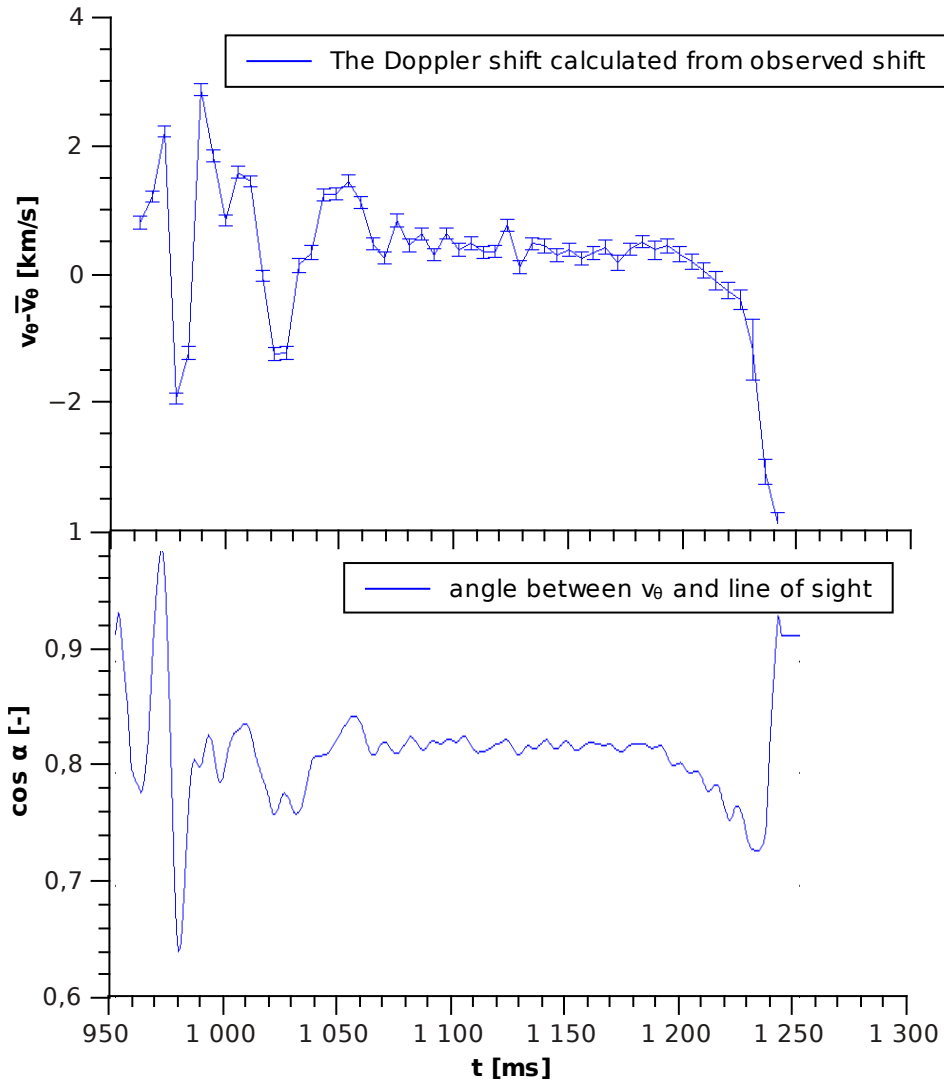


Figure 5.14: The observed false Doppler shift and the corresponding projection of the velocity (v -mean(v)) at shot #2606, the calculated $\cos \alpha$ from Eq. (3.5.1) and the R component of the plasma position. The shift is significantly increased by poor focus of the spectrometer at this shot.

this map can be approximated by its first derivative $F \approx F(x_i) + F'(x_i)\delta(x_i)$ and the statistical uncertainty σ_j of a parameter θ_j is

$$\sigma_j = \sqrt{\sum_{i=1}^n \left(\frac{\partial F_j}{\partial x_i} \right)^2 \xi_i^2} \quad (5.6.2)$$

where uncertainty ξ_i in the data points x_i is given by variance of the Poisson distribution (Eg. 5.6.1). The binning increase the uncertainty of the data by the factor $\sqrt{2}$

$$\sigma'_j = \sqrt{\sum_{i=1}^{n/2} \left(\frac{\partial F_j}{\partial x_{2i}} \right)^2 (\sqrt{2}\xi_{2i})^2} \quad (5.6.3)$$

If the second derivatives of the F are small, it can be expected that

$$\frac{\partial F_j}{\partial x_i} \approx \frac{\partial F_j}{\partial x_{i+1}}$$

and $\sigma_i \approx \sigma'_i$, because

$$\sigma_i = \sqrt{\sum_{i=1}^n \left(\frac{\partial F_j}{\partial x_i} \right)^2 \xi_i^2} = \sqrt{\sum_{i=1}^{n/2} \left(\frac{\partial F_j}{\partial x_{2i}} \right)^2 \xi_{2i}^2 + \left(\frac{\partial F_j}{\partial x_{2i+1}} \right)^2 \xi_{2i+1}^2} \approx \sqrt{\sum_{i=1}^{n/2} 2 \left(\frac{\partial F_j}{\partial x_{2i}} \right)^2 \xi_{2i}^2} = \sigma'_i$$

Therefore a dispersion change can influence the statistical uncertainty. It is also possible to make more general calculations for an arbitrary change of the dispersion but the conclusion would be the same. Decrease of the light density leads to increase of the statistical uncertainty.

However the increase of the dispersion can relatively decrease the influence of systematic errors.

5.6.2 Systematic uncertainty

Identification of the systematic uncertainties is not trivial. The most susceptible to the systematic errors are measurements of the absolute value of the shift. The two main known problems are the uncertainty introduced by the method used to identify the zero velocity (see Section Sec. 5.5) and a spontaneous drift.

A rough estimate of the systematic error for the current configuration is ~ 2 km/s. The most trustful methods is based on the optical fibres. Disadvantage of the measurement with the fibres is significant decrease of the light intensity and consequently decrease of the time resolution and also lost of the spatial resolution.

However, the only truly reliable test would be a swap of the plasma helicity and checking if the velocity has exactly opposite sign. However the changing of the direction of the toroidal magnetic field on the COMPASS is very complicate and it is not planned in near future.

The second important issue is the measurement of a spontaneous drift. The most probable cause of the drift are slow mechanical relaxation processes and thermal expansion of the

spectrometer. The thermal expansion coefficient of aluminium is $23 \cdot 10^{-6} \text{ }^\circ\text{C}^{-1}$ [73]. The expected drift caused by the change of the temperature by 1°C would be 1 px on the CCD. It is equivalent to a false Doppler shift about 2 km/s. However, the thermal drift is only a minor effect. The total drift is plotted in Figs. 5.15,5.16. The drift with a 24 hour period is clearly visible in the high frequency part. These data was achieved during 5 days of a continuous measurement. Although the neon line is not suitable for a precise measurement of the reference wavelength, the drift can be removed with precision about 0.1 km/s. This drift was also observed on the position of the CIII triplet lines as it is shown in Fig. 5.17. Unfortunately, it was not possible to measure the line drift from the neon lamp and the carbon lines at the same time period.

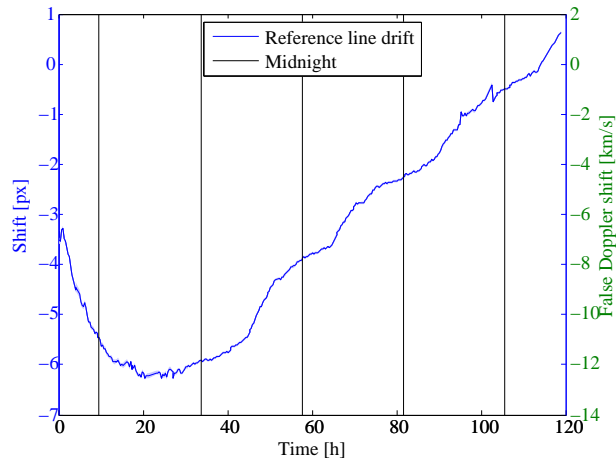


Figure 5.15: A slow drift of the neon line on the CCD during a continuous measurement between 2.3.2012–6.3.2012.

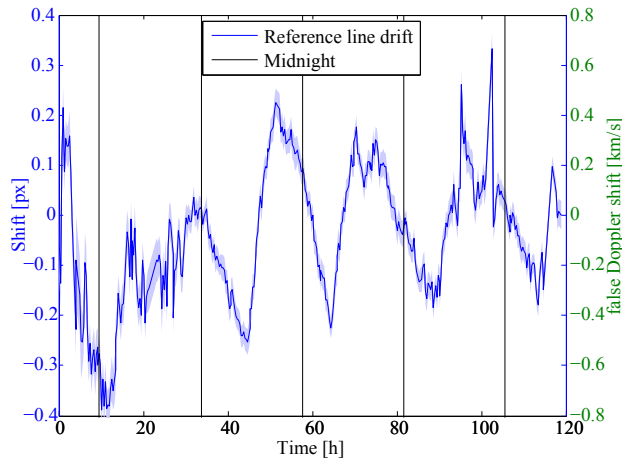


Figure 5.16: A higher frequency part of the slow drift (Fig. 5.15). The 24 hour period of the drift is clearly visible.

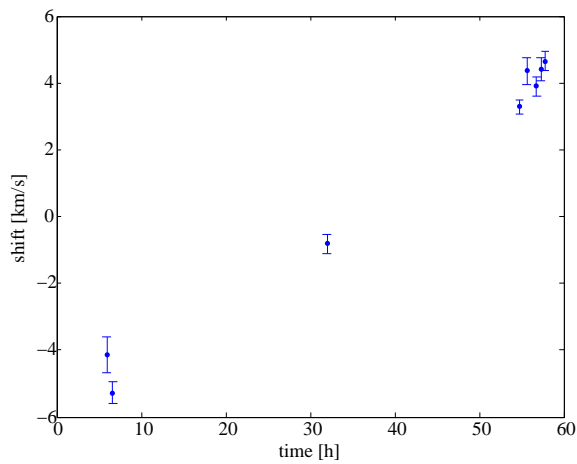


Figure 5.17: A spontaneous drift of the CIII triplet lines observed between 22-24.2.2012 using the shots 2878–2903

Chapter 6

Spectrometers control

One of the goals of this thesis was also developing of programs for the control and storage of the acquired data from the COMPASS spectrometers. In the previous situation, the spectrometers were manually prepared for trigger and after the trigger also the data were stored manually. This solution was unnecessarily time consuming and unreliable.

The control and evaluating of data from the Ocean Optics spectrometers and the high resolution spectrometer (Sec. 2.3.7) is so different that two separate programs had to be developed.

6.1 Ocean Optics spectrometers

6.1.1 Spectrometer Control

Java program for the control of the OceanOptics spectrometers and communication with the spectrometer drivers [74] was developed. This program is stored in file `HighSpeedAcquisition` on the attached data disk and the actual version is published on website [75]. This program was extensively tested on the GOLEM tokamak where is another suitable spectrometer available. The main attention was given to the reliability and maximal acquisition speed. It was possible to read 620 spectra per a second (14 per 25 ms) in the final configuration using a Linux server. Furthermore, systematic errors caused by readout patterns of the CCD were measured.

6.1.2 Data analyse

A project called `Ocean Optics spectrometer data analyzer` for the evaluation of the spectra was developed. The project is stored in folder `oospecanalyz` in the attached CD or an actual version can be download from the webpage [75]. This program was extensively tested on all the accessible data from the COMPASS and GOLEM tokamaks. The most important aspects are mentioned in the following list:

- *Object oriented program:* the program is flexible object based program written in Python.

- *Configuration files*: all the necessary information about the used spectrometers and tokamaks are stored in separate configuration files. Furthermore, the other information are stored, such as the CCD detector and grating effectivity, non-linearity corrections and also the absolute calibration that was calculated provisionally from the solar radiation.
- *Sensitivity of the lines detection*: the lines identification is based on an algorithm allowing detecting close to the statistical limit. Furthermore, the level of the false alarms is reasonable low.
- *Compatibility*: four different data formats that are used on COMPASS and two formats used on GOLEM can be loaded and processes using this program
- *Non-Gaussian instrumental function*: spectral lines are fitted by the skew Voigt instrumental function. The parameters of the instrumental function are stored in an appropriate spectrometer configuration file.
- *Automatics line identification*: the lines positions from the NIST database [76] are included in this program. Therefore, a very fast automatic line identification is implemented. The reliability of this fitting procedure depends on the precision of the wavelength calibration, resolving power of the spectrometer and also the dirtiness of the plasma. Therefore, very good results were achieved after a careful wavelength calibration on the COMPASS.
- *Examples* : The programs includes eight examples illustrating the possible applications: data loading, control of the spectrometer and also assisted line identification.
- *Actual status* : This program is fully integrated to the GOLEM database. Furthermore, integration to the database access tool `PyGo1em` [77] is prepared. On the other hand on the tokamak COMPASS, a provisional database is used and the automatic upload cannot be finished until the new database `pyCDB` will be fully operational.

A very important part of this program is the algorithm for the detection of the spectral lines. A criterion based on χ^2 statistics has been developed. Most of the observed lines in the COMPASS are close to the level of the detector noise and therefore detection algorithm must be very sensitive as well as robust. Under assumption of the Gaussian read-out noise and the mean width of peaks is n pixels than the following condition is fulfilled with probability $1 - \alpha$

$$\sum_{i=1}^n x_i^2 < \chi_\alpha^2(n)$$

where x_i corresponds to the signal, the variance is normalized to one and $\alpha = 0.01/M$, where M is the total number of pixels in the spectra. If the previous criterion is violated, the peak is detected. False rate is about 1% per a spectrum. It can be about 5% in case of the “hot pixels” on CCD. This way allows to achieve better sensitivity and robustness compared to the usually applied threshold criterion

$$x_i < \Phi^{-1}(\alpha) \quad \forall i \in 1 \dots M$$

where Φ is the normal cumulative distribution.

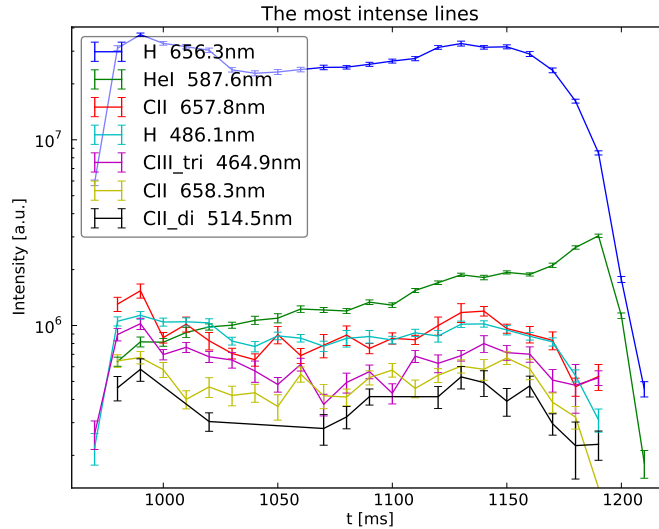


Figure 6.1: An example of the evaluated spectra from the shot #3038 using `oospecanalyz`

6.2 High resolution spectrometer

6.2.1 Andor Camera control

A script in the Andor Basic language [78] was developed for the communication with the Andor camera. This script is available in the file `AndorCameraControl.pgm` on attached CD. At the beginning of the script, all the necessary parameters are set and then the acquisition is started in an infinite cycle. This solution saves time compared to the a manual control used before. The data from acquisition are stored in a local folder and an external program must be used in order to upload the data to the final COMPASS database.

6.2.2 Data extraction

The data and acquisition parameters from the *asc* files of Andor Camera are extracted using `dataExtractionAndorASC`. The data loaded by this program will be stored in the final COMPASS database. The second purpose of this script is a real-time calculation of the line profile during the focusing and configuration of the spectrometer.

6.2.3 Data analyzing

The software for analysis of the data from the HR spectrometer is in folder `CIII_spectra_analyze` on attached CD. In the first stage, the data are preprocessed and the pixels corrupted by HXR radiation are removed. In the second stage, data are fitted using the weighted non-linear least squares using an appropriate model function. A robust fitting with the biweight M-estimator is used. Finally, various characteristics are calculated: H,V shift, temperatures, intensities and everything is plotted.

Chapter 7

Results

This chapter describes the obtained results. Further, the results will be compared with other available diagnostics on the COMPASS.

In the first section, parameters of different calibrations of the spectrometer from the years 2011–2012 will be summarized. In order to introduce the measured data and allow evaluating, the line integrated characteristics of the plasma will be computed the observed profiles in the section 7.2. Furthermore, the poloidal rotation measurements in the COMPASS tokamak are detailed in Section 7.3. The measured rotation is also compared to the neoclassical theory prediction and to the previous measurement on the COMPASS. Finally, evolution of the impurity ions temperature are presented in the two last sections.

7.1 Spectrometer configuration

Four attempts to focus the spectrometer were done in the years 2011–2012. The achieved parameters of the spectrometer are presented in the Tab. 7.1. The configurations in the Table 7.1 are sorted by the date when it was finished. The other columns contains: number of the usable shots, the second momentum (\sim width) of the instrumental function $\tilde{\phi}$ (Eq. (5.4.1)), the level of the background and stray light in the spectrometer and finally the achiever dispersion. The first configuration was finished in December 2011, however due to a poor focus (Fig. 7.1) and a high level of the background light, it had to be reconfigured in February 2012. In the second reconfiguration, the lowest 2. momentum of the instrumental function (its width) and the most Gaussian shape were obtained. Moreover, the background light was reduced 1300 \times . Nevertheless, the spectral line could be still better focused in the vertical direction and also the line was not precisely aligned with the CCD rows. The corresponding two dimensional shape of instrumental function was shown in Fig. 5.9 in the 5. Chapter. In the March 2012, the dispersion was increased by 16% but the results were poor. The last reconfiguration was finished in April 2012, but the results from February have never been achieved again.

N	Date	usable shots	2. moment	back. light [photons/px/s]	d [nm/m]
1	Dec 2011	25	22.2 px	91	0.199
2	Feb 2012	10	8.0 px	0.068	0.195
3	Mar 2012	6	19.6 px	2.34	0.164
4	April 2012	4	18.9 px	0.072	0.165

Table 7.1: The parameters of all recalibration of the spectrometer from years 2011/2012. The columns contains date when was the configuration finished, number of the usable shots, width of the function (5.4.1), the level of the background light and the dispersion d . For the final stage of spectrometer align in case 1 and 3 was responsible Portugal coworkers, I was responsible for 2. and 4.

7.2 Line integrated characteristic of the plasma

The observed light is radiated from a thin radiating shell of the C III ions. The shell is located ~ 2 cm inside the separatrix [79] for the COMPASS tokamak. This passive emission is caused by the combination of charge exchange from thermal neutrals with CIV ions and by the electron-impact excitation of C III. The observed quantities are line integrated over lines of sight (chords) and the local values can be acquired an inversion, so called unfolding. This problem was already investigated in articles [80, 81, 82]. There was developed an algorithm based on the inversion of the first 3 momentum of the observed profile from the n chords and calculation of the local moments in the plasma divided in the n concentric shells. However, this approach do not use all information in the data and it is an ill conditioned task. In the case of a very low Gaussian noise in the data and a very precisely arrangement of the experiment, this method allows to estimate the local plasma parameters close to the C III shell [72].

Much more reliable results can be achieved by unfolding algorithm based on nonlinear least square method described in article [83]. The advantage of this algorithm is simplicity together with universality. This algorithm can be easily generalized for a two dimensional instrumental function. This is a necessary condition for application of this method for our experiment. Moreover in this algorithm prevents the inward propagation of errors which is unavoidable in any Abel-like inversion scheme.

In this section, only the results achieved by analytical calculation of the line-integrated profiles will be summarized. Moreover, the behavior of the individual moments of the observed line shape will be investigated.

7.2.1 Zero momentum

The zero momentum of the observed spectra is the line integrated intensity. The observed line integrated profile of the is generally described by

$$I(\nu) = \frac{1}{4\pi} \int_V \phi(\nu, (\mathbf{v} \cdot \mathbf{n}), T_i(\mathbf{r}, t)) \epsilon(\mathbf{r}, t, T_e) d\Omega(\mathbf{r}') dV(\mathbf{r}) \quad (7.2.1)$$

where ϵ is local emissivity, \mathbf{r} is the position plasma, \mathbf{r}' is the position on detector, \mathbf{v} plasma velocity, $d\Omega$ is solid angle, dV is observed infinitesimal volume, ϕ is local line

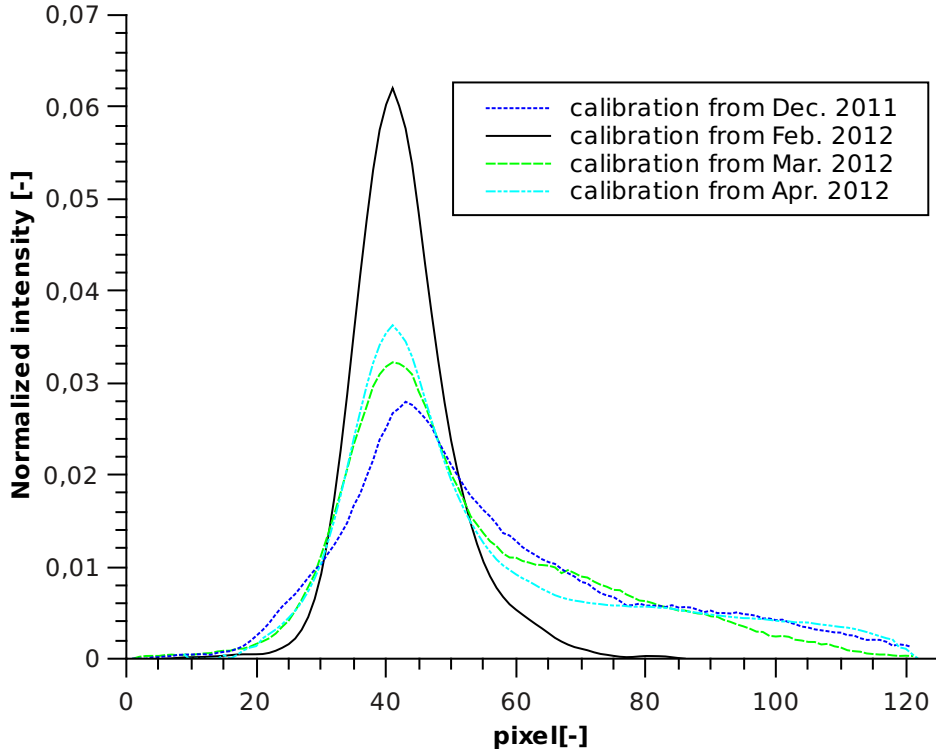


Figure 7.1: Shapes of the instrumental functions calculated according to Eq. (5.4.1) from the observed C III lines

profile Doppler shifted and Doppler broadened

$$\phi(\nu, (\mathbf{v} \cdot \mathbf{n})) = \frac{1}{\sqrt{2\pi\sigma^2}} \exp\left(-\frac{(\lambda - \lambda_0 - \lambda_0/c \mathbf{v} \cdot \mathbf{n})^2}{2\sigma^2}\right)$$

n is chord direction and Doppler broadening σ is defined by (3.5.2). The light intensity is only a zero momentum of the $I(\nu)$ and if the parallel non-diverging chords and circular plasma can be expected, the emissivity at radius r_0 can be estimated as

$$I_0(r_0) = \frac{\Omega}{4\pi} \int_{r_0}^a \epsilon(r) \frac{dr}{\sqrt{r^2 - r_0^2}}$$

An example of the line integrated profile of the intensity is shown in the Fig. 7.2a. The local emissivity ϵ has two main contributions, charge exchange with thermal neutrals ϵ_{CX} and the collisional excitation estimated from the coronal model ϵ_C

$$\epsilon = \epsilon_{CX} + \epsilon_C = \langle \sigma_{CX} v \rangle n_0 n_{CIII} + n_{CIII} n_e P_C \quad (7.2.2)$$

where $\langle \sigma_{CX} v \rangle$ is the charge exchange rate to the right excitation level and P_C is a radiated power function calculated from the stationary coronal model (Fig.7.3).

A typical time evolution of the spatial distribution of the C III radiation is in Fig. 7.5. The plasma discharge can be divided into three phases: during the first phases, the carbon ion C III is burned out from the center to the edge (Fig.7.4) and together with a higher influx of the neutrals from wall it results to higher radiation intensity. In the second phase, during the flat top, a stationary equilibrium is achieved when the C III ions create

a thin radiating shell at the edge of the plasma. The observed intensity is a half of the intensity during the plasma breakdown. Finally, during the last phase the plasma density and temperature slowly decreases.

7.2.2 First momentum

Change of the first moment of the measured lines should corresponds to the line integrated Doppler shift. the relation between local profile of the velocity and measured velocity for circular plasma can be expressed from the eq. (7.2.1) as

$$\langle v_\theta \rangle(r_{\min}) = \frac{\Omega}{4\pi I_0(r_{\min})} \int_{r_{\min}}^a \epsilon(r) \left(v_\theta(r) \frac{r}{a} \right) \frac{dr}{\sqrt{r^2 - r_{\min}^2}}$$

An example of a calculated line integrated velocity profile is in Fig. 7.2b. and an example of the radial profile of the velocity is in Fig. 7.6. Due to complications with a reliable measurement of the exact two dimensional instrumental function, only a time changes of the shift can be measured. It is not possible to measure the absolute value of the shift with the necessary precision.

Theoretically it is possible to estimate even the gradient of the poloidal intrinsic velocity. Unfortunately, such a measurement needs a very high precision that is not achievable with our spectrometer.

The shear of the radial electric field during the H-mode could cause a significant velocity gradient that should be measurable. Moreover in the H-mode, also other effect raising from significant temperature and density gradients in plasma must be taken in account [84].

7.2.3 Second momentum

The second momentum of the measured lines is related to the ion temperature. However evaluating of the real temperature from the measured is not trivial compared to the previous moments

$$\langle T_i \rangle(r_{\min}) = \frac{\Omega}{4\pi I_0(r_{\min})} \int_{r_{\min}}^a \epsilon(r, T_e) T_i \frac{dr}{\sqrt{r^2 - r_{\min}^2}}$$

An example of the calculated line integrated temperature is in Fig. 7.2c. Because the C III ions density and therefore the radiation intensity is a function of the electron temperature and density, the behaviour of the measured ion temperature is different from the other line integrated quantities. If the plasma temperature increases, the shell of the radiating C III will be shifted closer to the edge. This behaviour is typical for the part of the radiation resulting from coronal model equilibrium (Eq. (7.2.2)).

If the contribution of the charge exchange radiation to the total C III radiation is negligible, it is possible to analytically calculate the behaviour of the temperature during the flat top of the discharge [68]. From the calculation follows that the line integrated temperature observed at constant part of the radial profile in Fig. 7.2 depends on local

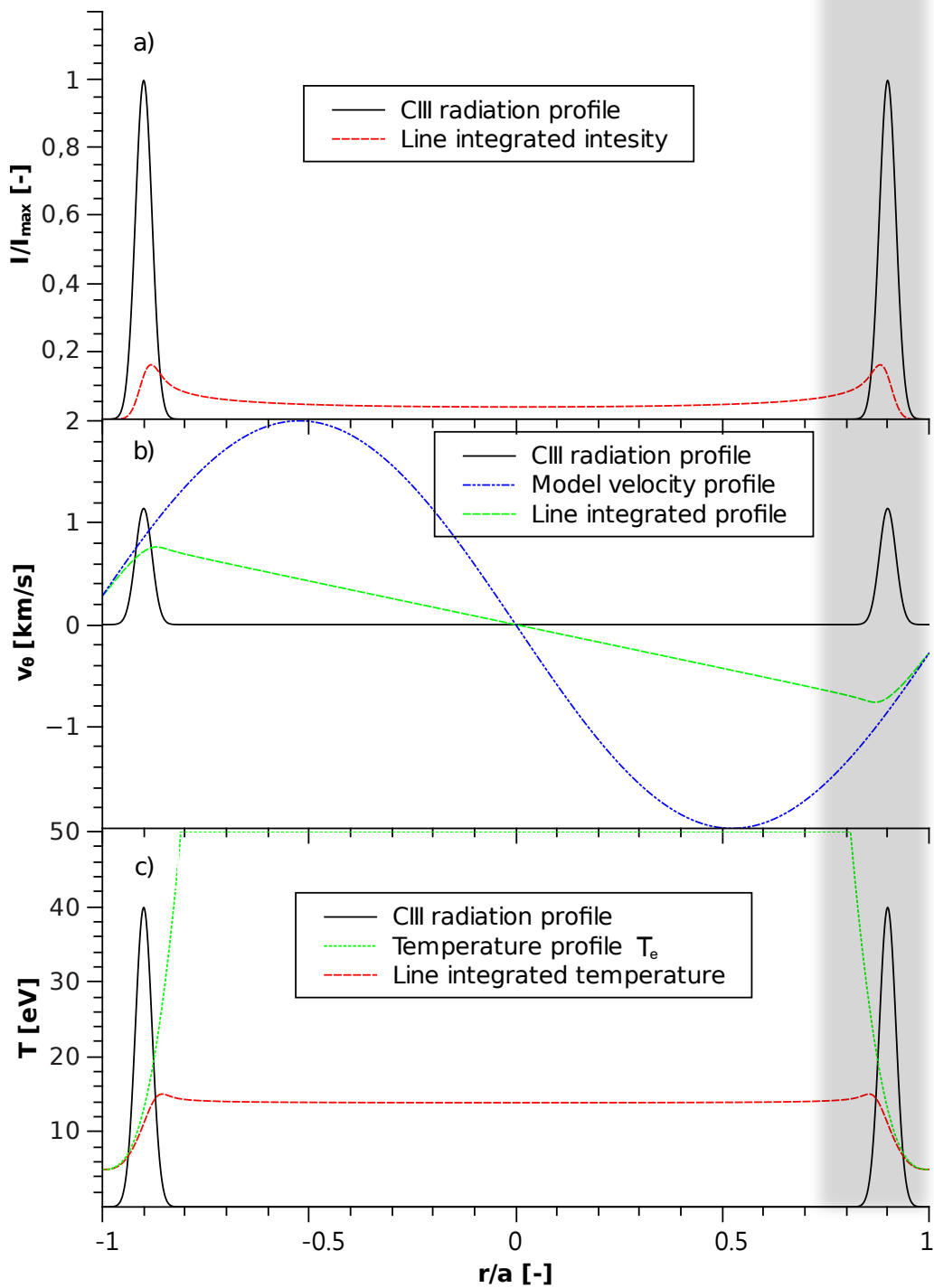


Figure 7.2: Line integrated characteristics of the plasma for model radiation from a 2 cm thick shell of the C III; a) zero moment - the light intensity, b) first moment - the velocity calculated from model profile, c) second moment - the temperature, data comes from Thomson scattering; the gray strip approximately corresponds to the observed region

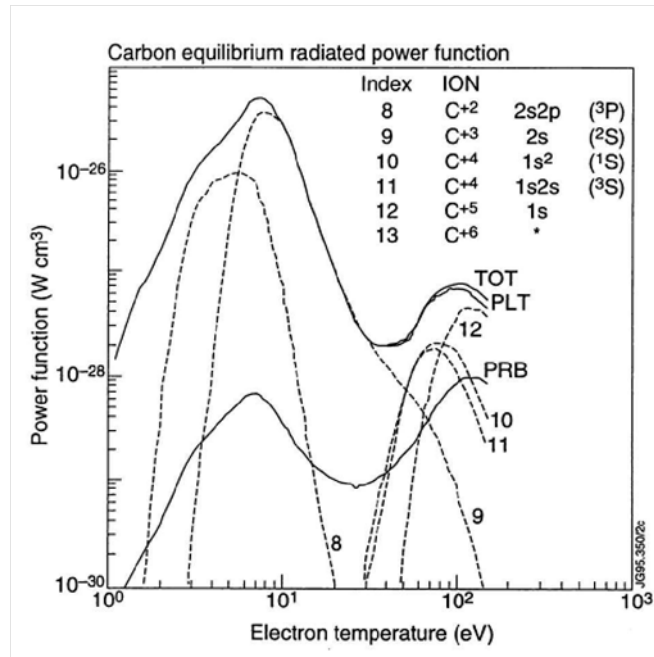


Figure 7.3: An expected power distribution of the carbon radiation calculated from the stationary coronal model

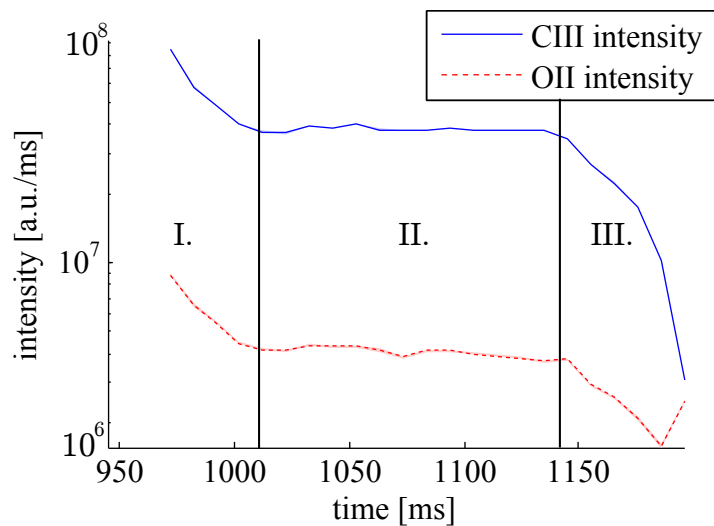


Figure 7.4: Light intensity observed by high resolution spectrometer during shot #2883, divided into 3 phases with respect to the radiation behavior.

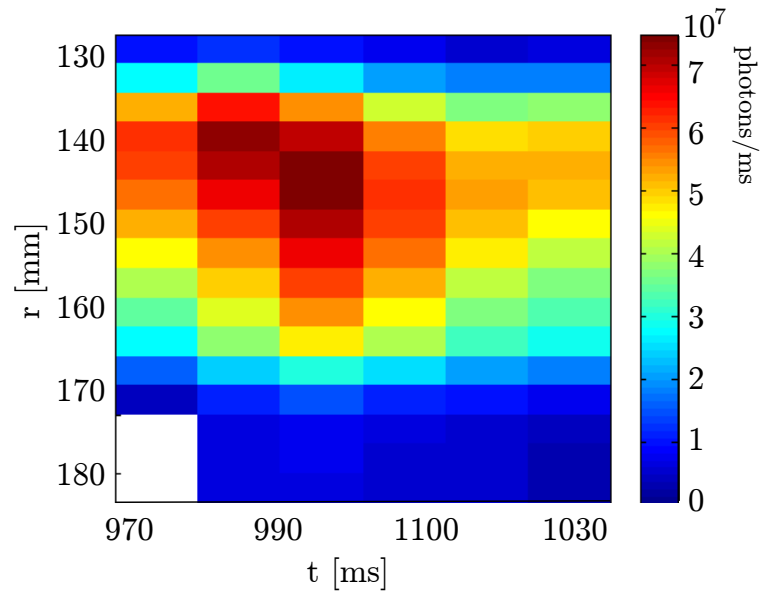


Figure 7.5: Line integrated radiation profile without a deconvolution in the radial direction, shot #2788

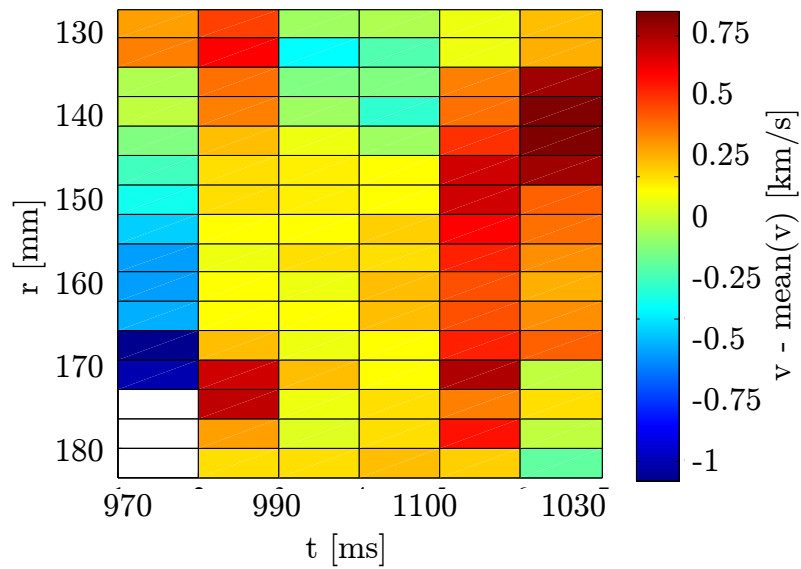


Figure 7.6: Time and spatial profile of the observed line shift during shot #2788.

gradient length of n_e and T_e and it should be independent of the local ion temperature, because the shape of the line $\phi(\lambda)$ would be

$$\phi(\lambda) \propto A(\lambda) + \frac{L_{T_e}}{L_{n_e}} B(\lambda) \quad (7.2.3)$$

where $A(\lambda)$ and $B(\lambda)$ are first order approximation independent of the plasma conditions and L_{T_e} and L_{n_e} are gradient lengths of electron temperature and density. An example of the spatial distribution of the temperature is plotted in Fig. 7.7. The temperature is almost constant about 35 eV, only at the position corresponding to $r = 170$ mm is a small peak. It can correspond to the same small peak on the line integrated temperature profile at the Fig. 7.2c, in $r/a = 0.85$, but it can be also some effect in the spectrometer.

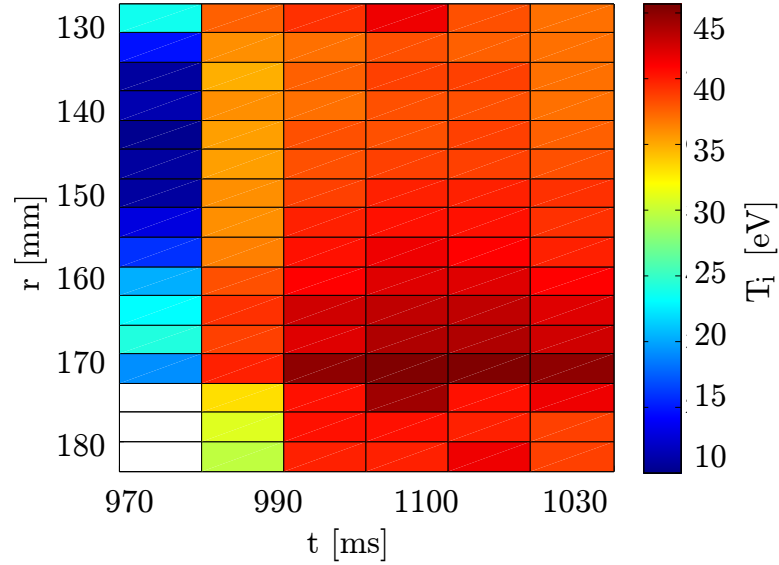


Figure 7.7: Spatial distribution of the line integrated CIII ion temperature from shot #2788

7.3 Plasma rotation

In this section, measurements of the poloidal plasma rotation on COMPASS are presented. Because neither of the two NBI was not fully functional, the plasma rotation was measured without external sources of momentum.

7.3.1 Neoclassical prediction

In the case of the ohmically heated plasma without any external sources of the poloidal momentum is the main source of the rotation the neoclassical effect explained in the section 4.3. If the momentum sink introduced by charge exchange with neutrals can be neglected, the poloidal velocity is given by formula (4.3.2b). The electron temperature was used for the calculations instead of the ion temperature gradient, assuming $T_i \sim T_e$. However the ion temperature can differ from the electron temperature at the plasma edge. A credible measurement of the ion temperature gradient was not available, therefore the electron temperature T_e from the Thompson scattering diagnostic was used. Also,

the normalized collisionality was calculated from the electron density observed by this diagnostics.

Typical T_e and n_e profiles are shown in Fig. 7.8. The plasma collisionality at the plasma edge is in the Pfirsch-Schüter regime and therefore the coefficient K_1 in Eq. (4.3.2b) changes the sign. The maximum rotation velocity is at the half of the minor radius and it is approximately 2 km/s. However, the rotation at the plasma edge is less than 0.5 km/s.

7.3.2 Rotation in ohmically heated plasma

The Doppler shift was evaluated only for the best achieved configuration of the spectrometer (Tab.7.1). However, only 10 longer discharges, which were not entirely corrupted by the HXR radiation, were analyzed. The parameters of these shots are in Tab. 7.2. These discharges were similar and the main differences are in the time evolution of the density.

The measured shifts of the spectra (recalculated to the plasma poloidal velocity) and the theoretical evolution of the neoclassical velocity are shown in Fig. 7.9. Only the velocity of the hydrogen was calculated, however the velocity of impurities (4.3.4b) is of the same order of magnitude. Because the accuracy of the wavelength calibration was too low, the systematic error was around 2 km/s, only the velocity with subtracted mean value was plotted instead of the measured velocity. At the beginning of the discharge, variation and decrease of the shift about 1 km/s is observed and at the end the speed (shift) is further decreased. This is not a real change of speed but rather an effect of movement of the CIII radiating shell. These changes of the position are caused by movements of the whole plasma column and also at the beginning by a formation of the CIII radiating shell at the plasma edge caused by a steep rise of the ion temperature. The radial position of the plasma column is plotted in Fig. 7.10, however changes of the radial position of the CIII shell can be slightly different. The significant disagreement is at the end of the discharge, where is the line shift opposite to the plasma shift. It could be caused by increasing impact of the integration drift on the plasma position during steep decrease of the plasma current.

Line shifts caused by movement of the plasma were significantly reduced compared to the previous configuration with a wide instrumental function. This line shift observed with first configuration (Tab.7.1) is in two first plots at Fig. 7.10, the shifts with the second configuration are in the rest four plots. Obviously the shift at the end of the discharge was reduced about $5\times$, shift at the beginning was reduced too. The apparent conclusion from the plots in Fig. 7.9 is that the neoclassical velocity cannot be measured due to low accuracy. The statistical precision can be significantly increased by extending the exposure time, however the accuracy can be increased only by a new and even better focusing and even better by installation of the optical fibers.

7.3.3 Rotation in NBI heated plasma

The rotation of the plasma during neutrals beams injection (NBI) could not be evaluated because no shots with the NBI were available. The NBI were not fully functional until the end of this thesis.

shot num.	I_p [kA]	$\langle n_e \rangle$ [10^{19}m^{-3}]	B_t [T]	Δt [ms]
2883	147	2.0	1.0	232
2895	156	2.5	1.15	229
2900	145	2.5	1.15	228
2903	135	2.0	1.15	230
2905	155	2.0	1.15	229
2906	153	2.5	1.15	230
2910	142	2.2	1.15	230
2914	144	2.5	1.15	230
2943	147	2.2	1.0	230
2945	153	3.0	1.0	146

Table 7.2: Basic parameters, plasma current, density, tor. mag. field, discharge length, of the usable shots observed with the 2. configuration of the spectrometer from Tab. 7.1.

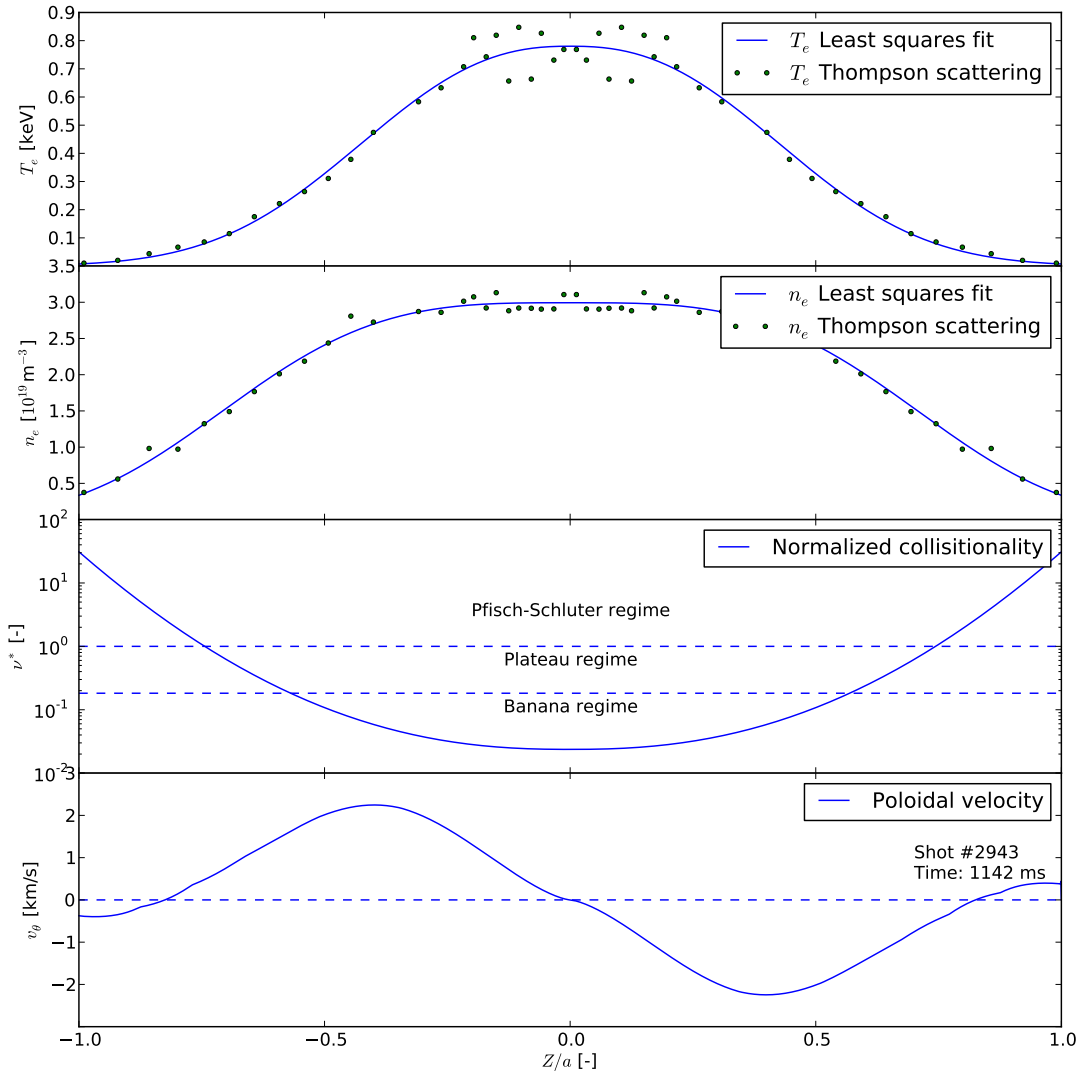


Figure 7.8: The neoclassical calculation of the poloidal velocity based on the formula (4.3.2b). Plasma temperature and density profiles was taken from Thompson scattering.

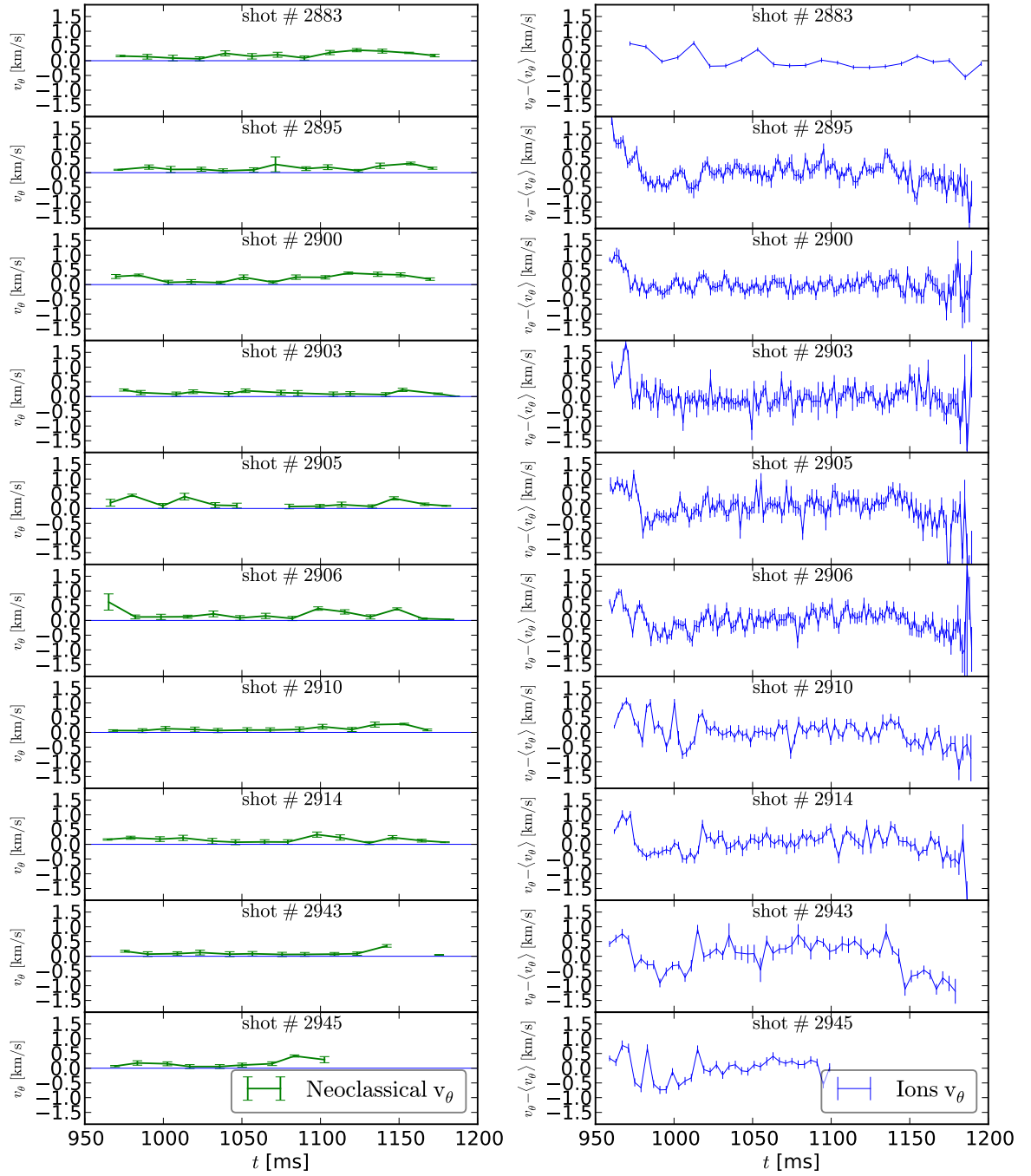


Figure 7.9: In the left column is calculated neoclassical velocity at the edge ($r/a = 0.95$) compared to the measured Doppler velocity in right column. Because the accuracy of the wavelength calibration was about ± 2 km/s, the absolute value of the velocity could not be calculated and therefore the mean velocity $\langle v_\theta \rangle$ subtracted from the measured velocity v_θ was plotted.

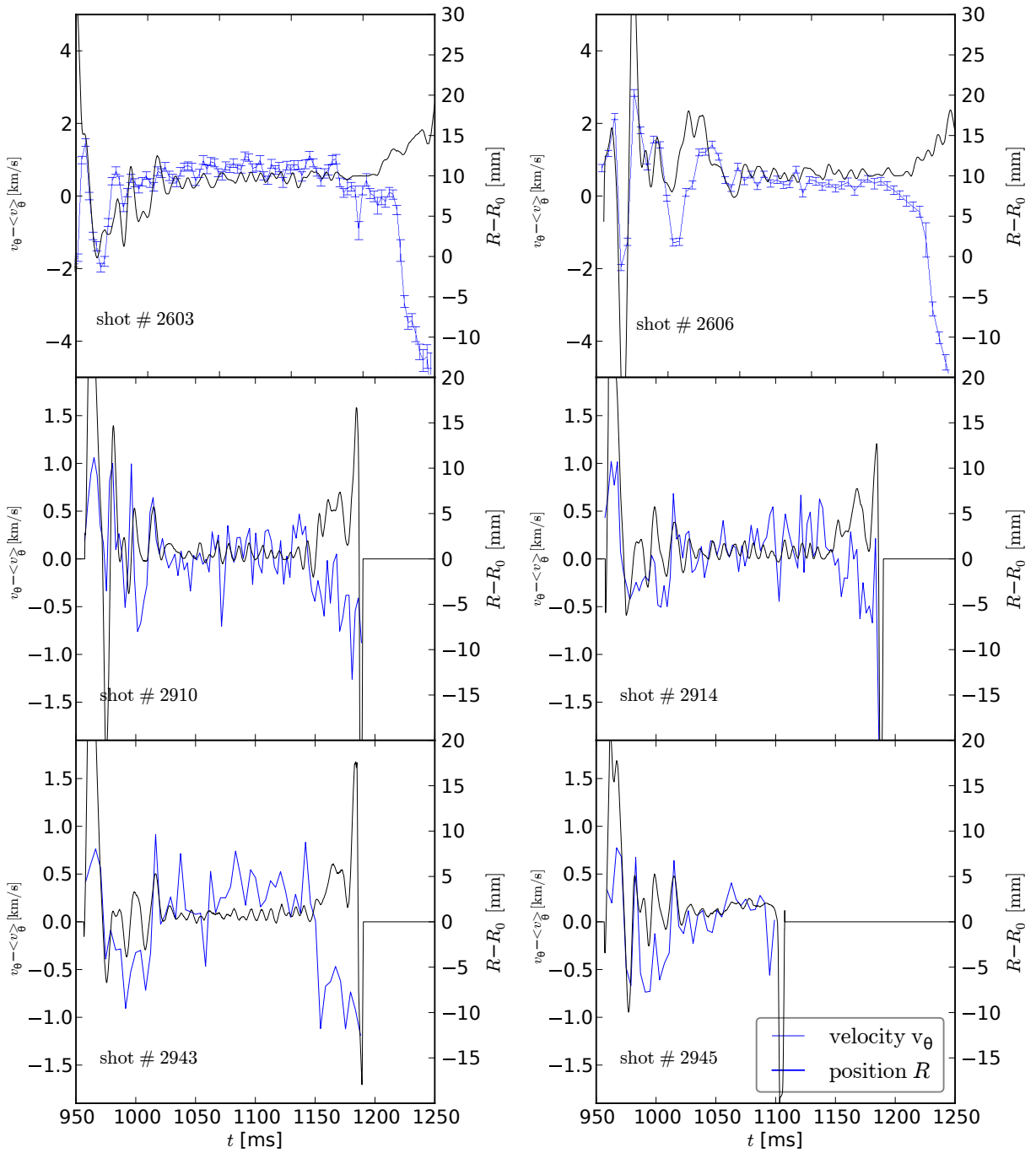


Figure 7.10: Observed shift of the line plotted together with the radial position of the plasma column. In the two first plots are shots 2603 and 2606 from the first spectrometer alignment (Tab. 7.1), in the rest are shots from the 2. alignment with most significant plasma movements.

7.3.4 Rotation measured on COMPASS in Culham

The plasma poloidal rotation measured in Culham can be taken as a realistic prediction of the rotation which could be observed with divertor plasma and during L-H transition. The measurement is described in [85] and some details can be found also in [79, 86, 87].

The configuration of the experiment was similar to the actual. The passive C III and B IV radiation at the plasma was measured. The radiation was observed by a Czerny-Turnov spectrometer [88] with a maximal dispersion 0.005 nm/px. Time resolution of this system was >0.15 ms, statistical precision of the Doppler shift >0.3 km/s and temperature precision >15 eV. High time resolution was achieved by an array of photo-cathodes whereas the high spectral resolution was achieved by a CCD camera.

They have measured for example the radial electric field during a clear ohmic H-mode (Fig. 7.11) or a fast breaking of the plasma rotation caused by ELMs. Unfortunately, these experiments cannot be repeated on our tokamak now because H-mode or other physically interesting circumstances have not been achieved, yet. The only interesting plasma phenomena which can be investigated is neoclassical rotation.

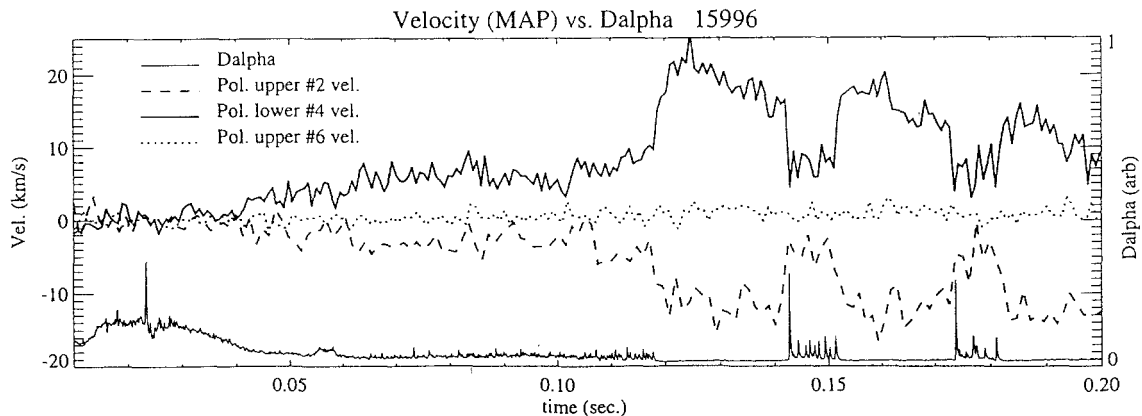


Figure 7.11: The poloidal velocity observed during L-H transition and ELM-free H-mode on the COMPASS tokamak measured in Culham [86]. Plasma shaping begin in 40 ms and L-H transition starts at 120 ms.

7.4 Ion temperature

The second investigated quantity was the ion temperature. The C III and O II temperature measured at discharges 2883-2945 (Tab. 7.2) is plotted in Fig. 7.12. The temperature was calculated from the line width averaged from the whole observed volume and the Zeeman splitting was subtracted. Flat top temperature of the C III ions was in range 15-30 eV and measured temperature of O II ions was 5-10 eV.

The expected maximal temperature based on equilibrium coronal model is up to 10 eV for C III (Fig. 3.3, 7.3) and up to 8 eV for O II ions [8]. This temperature is much smaller than the ionization temperature of C III – 47.8 eV and O II – 35.1 eV [73]. However, the measured temperature was about 25 eV for C III and 10 eV for O II. A possible explanation is that the coronal model is not valid in the low temperature edge plasma and can not

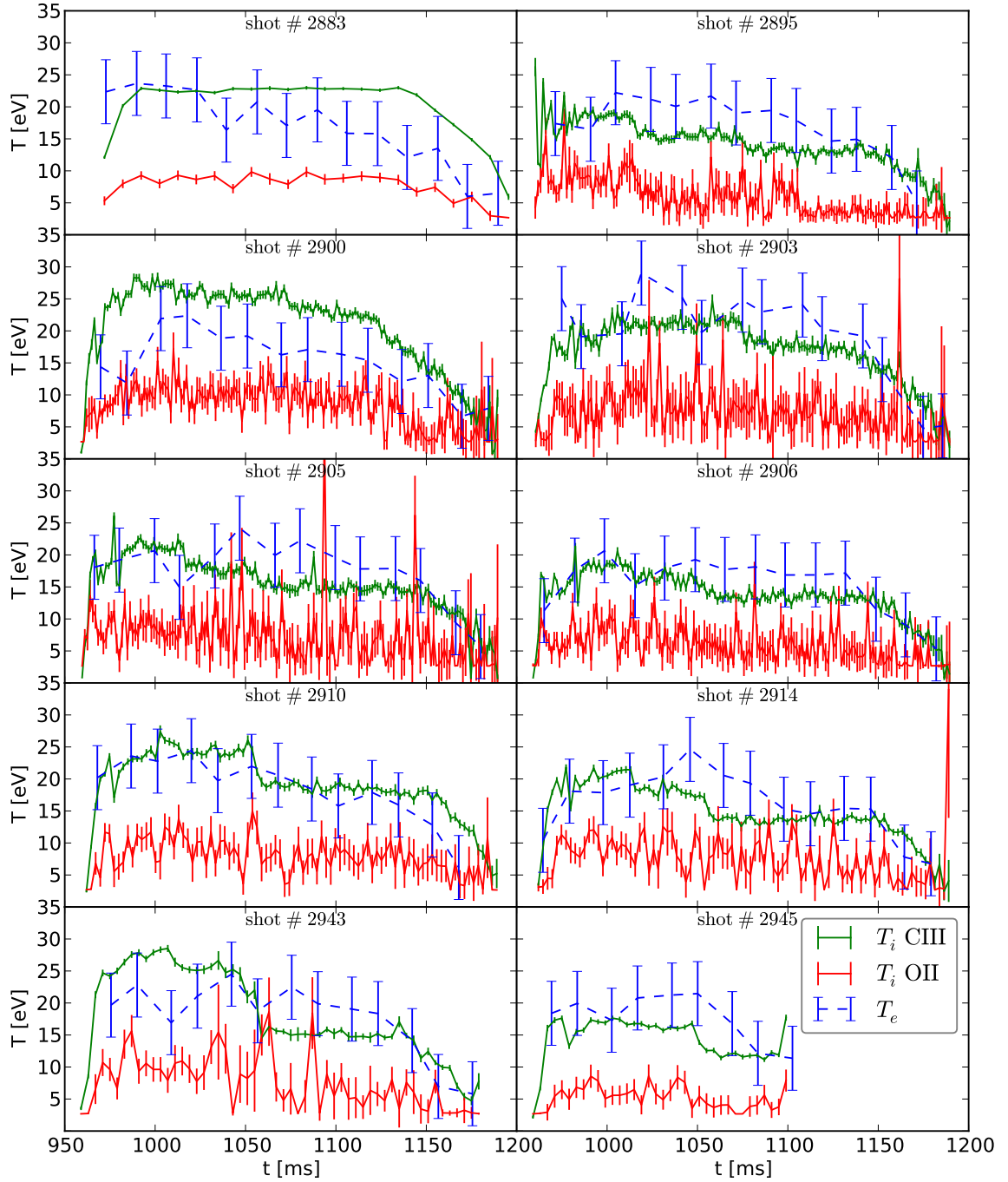


Figure 7.12: The measured line averaged ion edge temperature from the C III and O II radiation, compared to the electron temperature from the Thompson scattering diagnostics. Temperature from TS had to be 2.5 times decreased, because it was measured at $r = 0$ cm, $z = 15.6 - 19.4$ cm, whereas the ion temperature was measured at $r = 13.3 - 18.3$ cm

be used even as rough approximation. However the validity condition of coronal model in Eq. (3.3.1) is fulfilled, at least for hydrogen. The second explanation is important effect of the charge exchange radiation. The C III ions are created by recombination of the C IV ions in hot area of the plasma where radiates before are ionized again. This conclusion is also supported by following observations.

The interpretation of the measured ion temperature is more complicated due to issues connected with the passive spectroscopy explained in Section 7.2.3. The observed line width interpreted as the temperature is a result of the equilibrium established between atomics processes in the plasmas. Moreover if the ionization time is shorter than the thermalization time, the thermal equilibrium between impurities and the surrounding plasma cannot be established and the mean ion temperature can even decrease (Fig. 7.13). Furthermore, the predicted maximal temperature from this effect well corresponds to the measured values.

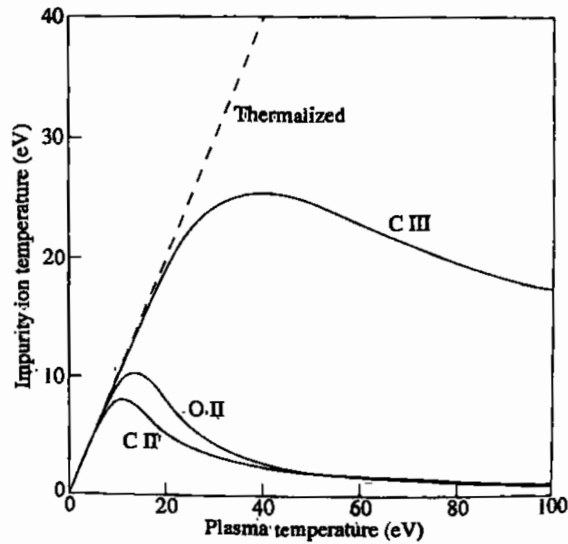


Figure 7.13: Calculated temperature of the impurities as a function of the plasma temperature. The initial temperature of the impurity was zero, the observed temperature is calculated from ionization and thermalization process [8].

The temperatures of carbon and oxygen from the shots in Tab. 7.2 are shown in Fig. 7.12. Although the parameters of the discharges were very similar, the observed temperatures are significantly different. Lets compare the shots 2900 and 2906, according to all other diagnostics (i.e. current and density evolution, Thompson scattering) these shots are identical. In spite of this, the temperature in the shots #2906 is about 40% lower. The only other difference was higher level of radiation from measured C III, O II ions and the increased radiation observed by the H_{α} detector. The radiation in the shot 2906 was almost $2\times$ lower. The increase of the temperature can be explained by increased influx of the neutrals. The neutrals penetrate deep into the hot plasma and then cause radiation by the charge exchange recombination with C IV ions.

The second observed phenomenon is a sudden decrease of the observed C III and O II temperature during the flattop phase in discharges 2903, 2910, 2914, 2943, 2945 (see Fig. 7.12). The most significant decrease was observed in shot 2943 where the temperature

drop was 30%. It is the reason why this discharge was investigated in detail. The abrupt jumps in O II temperature was caused by HXR corrupted spectra.

All diagnostics available for the shot #2943 are plotted in Fig. 7.14. The significant noise from diagnostics observed by COMPASS high speed data acquisition system was smoothed by a 4.0 ms time window corresponding to the exposure time of the high resolution spectrometer. The ion C III temperature in plot *a*) and C III and O II ion emissivity in plot *b*) was acquired using the HR spectrometer. Input power in *e*) is estimated as $P_{in} = P_{OH} - LdI_p^2/dt$. Finally, the edge electron temperature and density in the plots *a*), *g*), mean density in plot *e*) and gradient lengths of electron density and temperature in plot *h*) were also calculated from the central Thompson scattering (TS) diagnostics. The edge TS has not been installed yet and therefore the central TS is currently the only diagnostic routinely measuring the edge plasma. The start and the end of the flattop is indicated by dash-dot lines and the position of the sudden drop of the ion temperature is indicated by a vertical dashed line.

The only relevant change observed by the available diagnostics is a rapid central density increase, faster than in other discharges. Any significant change can be observed in temperature and density gradient length and therefore the formula (7.2.3) was not confirmed. However one important different can be seen on the injection of the working gas. A few millisecond before the observed temperature drop a 50% increase of gas puff was set. Because the H_α radiation stayed unchanged, the hydrogen had to be fully ionized close to the valve, on the opposite side of the tokamak where are all optical diagnostics installed. However, the edge main species and after a few milliseconds also the impurities as carbon or oxygen were cooled down. While the higher neutral influx increase observed temperature, the the gas puff cool down the ions without any significant effect on the electron temperature.

Conclusion

The reliable measurement and inversion of the local ion temperature could be done, however only if the position of the plasma edge and spectrometer chords will be known with high precision. The necessary precision and stability of the chords position can be ensured only by employing optical fibres. Moreover, a better focus in the saggatial plane must be achieved in order to improve the radial resolution.

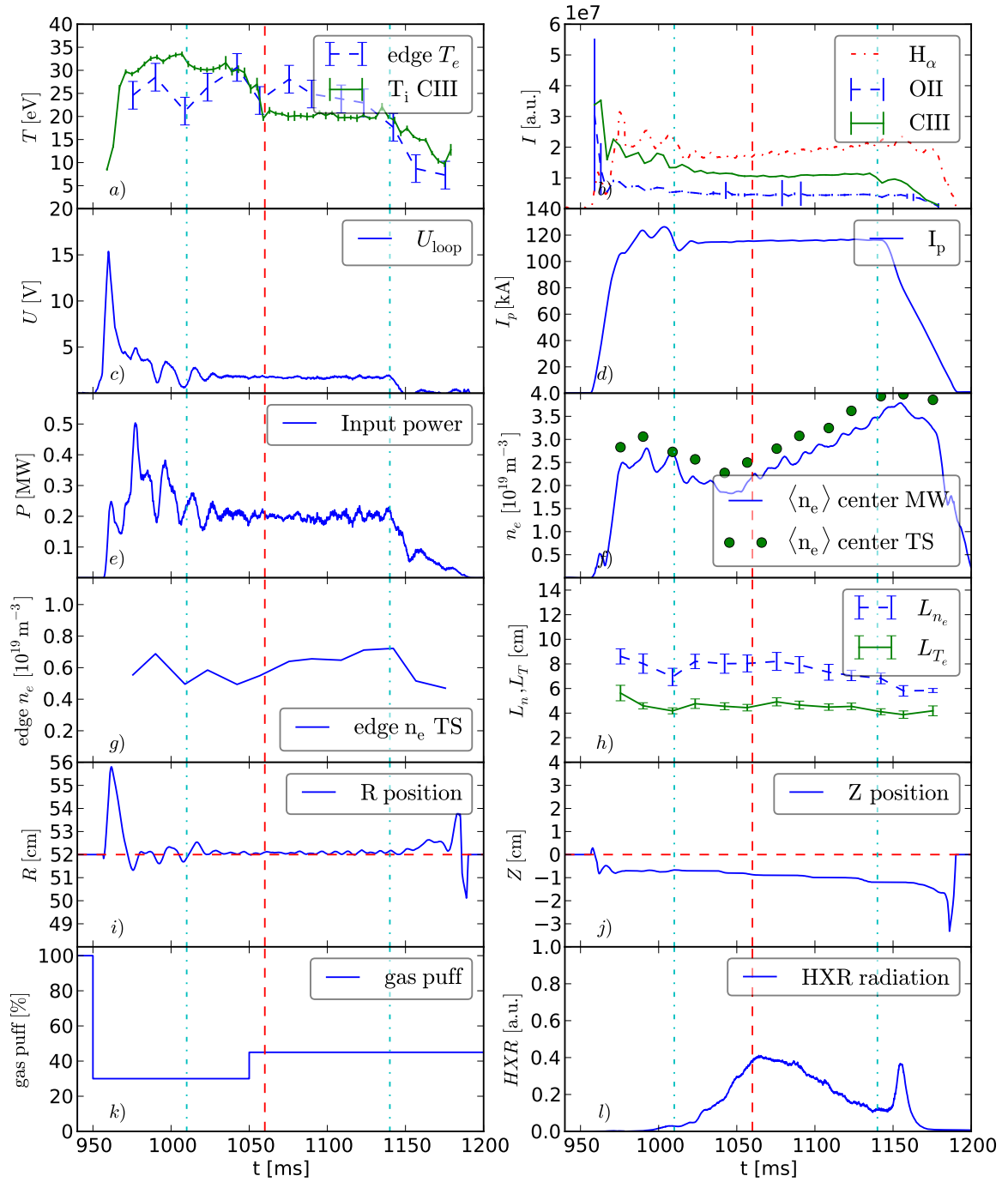


Figure 7.14: Temporal evolution of the diagnostics available on the COMPASS tokamak in the discharge #2943. The ion CIII temperature in plot a) and CIII and OII ion emissivity in plot b) was acquired using the HD spectrometer, input power in e), the edge electron temperature and density in the plots a), g), mean electron density from Thompson scattering (TS) and microwaves (MW) in plot e) and gradient lengths of electron density L_{n_e} and temperature L_{T_e} in plot h) were also calculated from the Thompson Scattering diagnostics.

Conclusions and suggestions for future experiments

The installed high resolution spectrometer is actually the diagnostics with the highest spatial and temporal resolution in the edge plasma on COMPASS tokamak. Therefore, it will be a crucial diagnostic for the future experiments focused on plasma edge.

Several installations of the spectrometer to the tokamak including the alignment of the optical path were accomplished in this work. During the second installation by a careful focusing and alignment was achieved the highest registered photon throughput and spatial resolution than ever before on this device. Moreover a narrow and Gaussian instrumental function was observed. In spite of this success, both spatial and wavelength resolution can be improved even more.

The second aim of this work was implementation of a data access for the spectrometer to the COMPASS database. Programs for controlling of the spectrometer and evaluating of the spectra were successfully developed. However, because the new COMPASS database is not finished yet, the data are stored in a temporal database. The program for the control of the HR2000+ spectrometers was also tested on the GOLEM tokamak and successfully included to this tokamak database.

The last part of this work was focused on the measurement and discussion of the ion temperature and plasma rotation in the ohmically heated limited circular plasma. The measured rotation velocity was 0 ± 2 km/s. The measurement of the NBI could not be realized because the NBI was not operating until the deadline of this thesis.

Suggestions for future

The achieved parameters of the spectrometer are sufficient for a measurement of the plasma velocity during the H-mode, however for identification of the neoclassical rotation further improvements must be applied.

First and the most important is buying a hollow cathode copper lamp for calibration and achieving at least the best configuration that was already achieved in this work. Furthermore a fiber optics should be tested. At the beginning two edge fibers from the visible tomography system for differential Doppler spectroscopy can be used. The spectrometer could be then placed to a shielded room to the temperature controlled environment. If this approach will be verified a whole optical path from fiber should be installed.

However, great results can be achieved even without the optical fibers. A higher throughput of the mirror based optical path ensure more light and a short exposure time can

be used. The difficult measurement of the reference wavelength and can be avoided by almost perfect wavelength calibration and instrumental function measurement by a glow discharge of neon at tokamak. If the position of the plasma edge will be known with a millimeter precision a tomographical reconstruction can be applied and the line averaged plasma parameters can be inverted to the local values on the flux surfaces.

In conclusion, the current configuration of the spectrometer will be sufficient for the observation of the rotation during the L-H transition. However the neoclassical rotation or inversion of the line integrated quantities cannot be finished without the suggested upgrades.

Bibliography

- [1] D. Clayton, *Principles of stellar evolution and nucleosynthesis: with a new preface.* University of Chicago Press, 1968.
- [2] J. Lawson, “Some criteria for a power producing thermonuclear reactor,” *Proceedings of the Physical Society. Section B*, vol. 70, p. 6, 1957.
- [3] W. Elmore, J. Tuck, and K. Watson, “On the inertial-electrostatic confinement of a plasma,” *Physics of Fluids*, vol. 2, p. 239, 1959.
- [4] P. Helander and D. Sigmar, *Collisional transport in magnetized plasmas*, vol. 87. Cambridge University Press, 2002.
- [5] L. Spitzer and P. U. P. P. Laboratory, “The stellarator concept,” *Physics of Fluids*, vol. 1, no. 4, p. 253, 1958.
- [6] L. Artsimovich, V. Afrosimov, I. Gladkovskij, *et al.*, “Ohmic heating of the plasma in toroidal machine tokamak-3,” *Plasma Physics and Controlled Nuclear Fusion Research, IAEA, Vienna*, vol. 2, p. 595, 1966.
- [7] H. Grad and H. Rubin, “Hydromagnetic equilibria and force-free fields,” in *2nd Int. Conf. Peac. Uses of Atom. Energy*, vol. 31, p. 386, 1958.
- [8] J. Wesson, *Tokamaks*. Oxford University Press, New York, NY, 1987.
- [9] M. Kruskal and M. Schwarzschild, “Some instabilities of a completely ionized plasma,” *Proceedings of the Royal Society of London. Series A. Mathematical and Physical Sciences*, vol. 223, no. 1154, p. 348, 1954.
- [10] V. Shafranov, “Atomnaya energiya 1, no. 5, 38 (1956),” *English trans. in/. Nucl. Energy*, vol. 5, p. 86, 1957.
- [11] EFDA, “Tokamak principle.” online, 9 2011. <http://www.efda.org/2011/09/tokamak-principle-2/> [cite:1.5.2012].
- [12] “Official site of the iter project.” online. <http://www.iter.org>.
- [13] “ITER Plant Description Document (2009) available in the ITER Document Management System (IDM) PD - Plant Description (2X6K67),” tech. rep. <https://user.iter.org/?uid=2X6K67> [cite:15.2.2011].
- [14] EURATOM/UKAEA, “Fusion association offer of COMPASS to IPP Prague.” http://server.ipp.cas.cz/~vwei/pictures/compass_offer.png [cite:15.2.2011].

- [15] R. Pánek, O. Bilyková, V. Fuchs, M. Hron, P. Chráska, P. Pavlo, J. Stöckel, J. Urban, V. Weinzettl, J. Zajac, *et al.*, “Reinstallation of the COMPASS-D tokamak in IPP ASCR,” *Czechoslovak Journal of Physics*, vol. 56, pp. 125–137, 2006.
- [16] P. Cahyna, R. Panek, V. Fuchs, L. Krlin, M. Becoulet, G. Huysmans, and E. Nardon, “The optimization of resonant magnetic perturbation spectra for the COMPASS tokamak,” *Nuclear Fusion*, vol. 49, p. 055024, 2009.
- [17] V. Weinzettl, R. Panek, M. Hron, J. Stockel, F. Zacek, J. Havlicek, P. Bilkova, D. Naydenkova, P. Hacek, J. Zajac, *et al.*, “Overview of the COMPASS diagnostics,” *Fusion Engineering and Design*, 2011.
- [18] J. Havlicek, J. Horacek, V. Weinzettl, O. Hronova, D. Naydenkova, and J. Zajac, “Magnetic diagnostics for start-up phase of COMPASS,” *WDS’09 Proceedings of Contributed Papers: Part II—Physics of Plasmas and Ionized Media*, pp. 148–152, 2009.
- [19] J. Horacek, *Measurement of edge electrostatic turbulence in the TCV tokamak plasma boundary*. PhD thesis, ÉCOLE POLYTECHNIQUE FÉDÉRALE DE LAUSANNE, 2006.
- [20] A. Silva, J. Zajac, and M. Manso, “Design of reflectometry system for the Compass-D tokamak,” tech. rep., internal report CFN/IST, 2007.
- [21] X. Weiwen, D. Xuanton, L. Zetian, Y. Lianghua, S. Hongjuan, D. Xuru, Y. Longwen, and Y. Qingwei, “Measurement of turbulence propagation velocity using doppler reflectometer on HL-2A Tokamak,” *Plasma Science and Technology*, vol. 10, p. 403, 2008.
- [22] P. Bílková, M. Aftanas, P. Böhm, V. Weinzettl, D. Šesták, R. Melich, J. Stöckel, R. Scannell, and M. Walsh, “Design of new thomson scattering diagnostic system on COMPASS tokamak,” *Nuclear Instruments and Methods in Physics Research Section A: Accelerators, Spectrometers, Detectors and Associated Equipment*, vol. 623, no. 2, pp. 656–659, 2010.
- [23] V. Weinzettl, D. Naydenkova, D. Sestak, J. Vlcek, J. Mlynar, R. Melich, D. Jares, J. Malot, D. Sarychev, and V. Igochine, “Design of multi-range tomographic system for transport studies in tokamak plasmas,” *Nuclear Instruments and Methods in Physics Research Section A: Accelerators, Spectrometers, Detectors and Associated Equipment*, vol. 623, no. 2, pp. 806–808, 2010.
- [24] D. Naydenkova, V. Weinzettl, J. Stockel, D. Šesták, and M. Aftanas, “Design of new optical system for visible plasma radiation measurements at COMPASS tokamak,” in *Proceedings of the 17th Annual Conference of Doctoral Students, WDS*, 2008.
- [25] J. Mlynar, V. Weinzettl, and M. Odstrcil, “Progress in rapid tomography for the COMPASS tokamak,” *Bulletin of the American Physical Society*, vol. 55, 2010.
- [26] M. Anton, H. Weisen, M. Dutch, W. Linden, F. Buhlmann, R. Chavan, B. Marletaz, P. Marmillod, and P. Paris, “X-ray tomography on the TCV tokamak,” *Plasma physics and controlled fusion*, vol. 38, p. 1849, 1996.

- [27] H. Griem, “Principles of plasma spectroscopy,” *Proceedings of the Physical Society*, vol. 1, 2005.
- [28] J. Coenen, *The Influence of the Dynamic Ergodic Divertor on the Radial Electric Field at the Tokamak TEXTOR*, vol. 39. Forschungszentrum Jülich, 2009.
- [29] A. Bortolon, *Plasma Rotation and Momentum Transport Studies in the TCV Tokamak Based on Charge Exchange Spectroscopy Measurements*. PhD thesis, ÉCOLE POLYTECHNIQUE FÉDÉRALE DE LAUSANNE, 2009.
- [30] R. Gomes, C. Varandas, J. Cabral, E. Sokolova, and S. Cortes, “High dispersion spectrometer for time resolved Doppler measurements of impurity lines emitted during ISTTOK tokamak discharges,” *Review of Scientific Instruments*, vol. 74, no. 3, pp. 2071–2074, 2003.
- [31] J. Urban, V. Fuchs, R. Pánek, J. Preinhaelter, J. Stöckel, F. Žáček, V. Davydenko, and V. Mishagin, “Nbi system for reinstalled COMPASS-D tokamak,” *Czechoslovak Journal of Physics*, vol. 56, pp. 176–181, 2006.
- [32] V. Fuchs, O. Bilyková, R. Pánek, M. Stránský, J. Stöckel, J. Urban, F. Žáček, Y. Peysson, J. Decker, I. Voitsekhovitch, *et al.*, “Heating and current drive modeling for the ipp prague COMPASS tokamak,” in *Proc. 35th EPS Conf. on Plasma Physics (Hersonissos, Greece)*, vol. 32, 2008.
- [33] R. Goldston, D. McCune, H. Towner, S. Davis, R. Hawryluk, and G. Schmidt, “New techniques for calculating heat and particle source rates due to neutral beam injection in axisymmetric tokamaks,” *Journal of computational physics*, vol. 43, no. 1, pp. 61–78, 1981.
- [34] J. Stöckel, “Dodatečný ohřev plazmatu v tokamacích energetickým svazkem atomu,” 2011. Zimní seminář FJFI, Mariánská.
- [35] C. De Michelis and M. Mattioli, “Soft-x-ray spectroscopic diagnostics of laboratory plasmas,” *Nuclear Fusion*, vol. 21, p. 677, 1981.
- [36] O. site of the FLYCHK code: <http://nlte.nist.gov/fly>.
- [37] I. Hutchinson, *Principles of plasma diagnostics*. Cambridge University Press, 2002.
- [38] P. Brussaard and H. Van de Hulst, “Approximation formulas for nonrelativistic bremsstrahlung and average gaunt factors for a maxwellian electron gas,” *Revs. Modern Phys.*, vol. 34, 1962.
- [39] R. McWhirter, “Spectral intensities, plasma diagnostic techniques,” *Academic Press, New York*, p. 206, 1965.
- [40] C. Fa-Yin and S. Bing-Ren, “Study of impurity behaviour in non-coronal equilibrium state,” *Chinese Physics*, vol. 16, p. 3458, 2007.
- [41] V. Weinzettel, *Prostorové a časové chování lehkých nečistot ve vysokoteplotním plazmatu*. PhD thesis, CVUT FJFI, 2004.
- [42] “ADAS - Atomic Data and Analysis Structure, <http://www.adas.ac.uk>.”

- [43] H. Chung, M. Chen, W. Morgan, Y. Ralchenko, and R. Lee, “Flychk: Generalized population kinetics and spectral model for rapid spectroscopic analysis for all elements,” *High energy density physics*, vol. 1, no. 1, pp. 3–12, 2005.
- [44] O. V. Hoey, “Visible light measurements on the COMPASS tokamak,” Master’s thesis, University Gent, 2010.
- [45] H. Griem, “Spectral line broadening by plasmas,” *New York, Academic Press, Inc. (Pure and Applied Physics. Volume 39), 1974. 421 p.*, vol. 1, 1974.
- [46] J. FORMÁNEK, *Úvod do kvantové teorie I. a II.* Akademia, Praha 2004.
- [47] J. Baldzuhn, “Diagnostics for fusion plasmas,” 2011. IPP Summer University on Plasma Physics.
- [48] T. Soetens, R. Jaspers, M. Von Hellermann, G. Van Oost, and E. Desoppere, “Quantitative beam emission spectroscopy on TEXTOR-94.,” in *Proceedings of the 27th EPS Conference on Controlled Fusion and Plasma Physics, Budapest (Hungary), 12-16 June 2000, 4pp*, 2000.
- [49] A. Peeters, “Toroidal momentum transport,” 6 2010. Isaac Newton Institute, presentation http://www.gkw.org.uk/pdf/AGPeeters_Cambridge_2010.pdf.
- [50] A. Kallenbach, H. Mayer, G. Fussmann, V. Mertens, U. Stroth, O. Vollmer, *et al.*, “Characterization of the angular momentum transport in ASDEX,” *Plasma Physics and Controlled Fusion*, vol. 33, p. 595, 1991.
- [51] Y. Camenen, A. Peeters, C. Angioni, F. Casson, W. Hornsby, A. Snodin, and D. Strintzi, “Transport of parallel momentum induced by current-symmetry breaking in toroidal plasmas,” *Physical review letters*, vol. 102, no. 12, p. 125001, 2009.
- [52] P. De Vries, M. Hua, D. McDonald, C. Giroud, M. Janvier, M. Johnson, T. Tala, and K. Zastrow, “Scaling of rotation and momentum confinement in JET plasmas,” *Nuclear Fusion*, vol. 48, p. 065006, 2008.
- [53] J. Cornelis, R. Sporcken, G. Oost, and R. Weynants, “Predicting the radial electric field imposed by externally driven radial currents in tokamaks,” *Nuclear fusion*, vol. 34, p. 171, 1994.
- [54] V. Rozhansky and M. Tendler, “Plasma rotation in tokamaks,” *Reviews of Plasma Physics*, vol. 19, p. 147, 1996.
- [55] P. Monier-Garbet, K. Burrell, F. Hinton, J. Kim, X. Garbet, and R. Groebner, “Effects of neutrals on plasma rotation in DIII-D,” *Nuclear fusion*, vol. 37, p. 403, 1997.
- [56] J. Rice, “Spontaneous rotation and momentum transport in tokamak plasmas,” in *Journal of Physics: Conference Series*, vol. 123, p. 012003, IOP Publishing, 2008.
- [57] J. Berger, W. Newcomb, J. Dawson, E. Frieman, R. Kulsrud, and A. Lenard, “Heating of a confined plasma by oscillating electromagnetic fields,” *Physics of Fluids*, vol. 1, p. 301, 1958.
- [58] T. Stix, “Decay of poloidal rotation in a tokamak plasma,” *Physics of Fluids*, vol. 16, p. 1260, 1973.

- [59] Y. Kim, P. Diamond, and R. Groebner, “Neoclassical poloidal and toroidal rotation in tokamaks,” *Physics of Fluids B: Plasma Physics*, vol. 3, p. 2050, 1991.
- [60] S. Hirshman and D. Sigmar, “Neoclassical transport of impurities in tokamak plasmas,” *Nuclear Fusion*, vol. 21, p. 1079, 1981.
- [61] D. Testa, C. Giroud, A. Fasoli, K. Zastrow, and E. Team, “On the measurement of toroidal rotation for the impurity and the main ion species on the Joint European Torus,” *Physics of Plasmas*, vol. 9, p. 243, 2002.
- [62] F. Waelbroeck, “Natural velocity of magnetic islands,” *Physical review letters*, vol. 95, no. 3, p. 35002, 2005.
- [63] C. Palmer and E. Loewen, *Diffraction grating handbook*. Newport Corporation, 2005.
- [64] H. Rowland, “LXI. Preliminary notice of the results accomplished in the manufacture and theory of gratings for optical purposes,” *Philosophical Magazine Series 5*, vol. 13, no. 84, pp. 469–474, 1882.
- [65] A. Sokolova, Elena, S. D. R. Cortes, and N. Mineiro, “High-resolution spectrometer for tokamak plasma diagnostics,” *Proc. SPIE 3130, 160*, 1997.
- [66] *Andor iXoin^{EM} + Performance Sheet*. Model: DU-897E-CS0-BV .
- [67] Andor, “iXonEM+ 897 (back-illuminated) – specification sheet.” online.
- [68] T. Odstrčil, “Development of diagnostics system for plasma rotation measurement on the tokamak COMPASS,” 2011. Research work.
- [69] T. Odstrčil, “Atom processors and quantum networks,” 2010. Bachelor thesis.
- [70] N. Black and S. Moore, “Gauss-seidel method.” *From MathWorld—A Wolfram Web Resource*, created by Eric W. Weisstein. <http://mathworld.wolfram.com/Gauss-SeidelMethod.html> [cite-1.5.2012].
- [71] D. Young and C. P. D. o. M. University of Maryland, *Iterative methods for solving partial difference equations of elliptic type*. PhD thesis, Harvard University, 1950.
- [72] T. Biewer, R. Bell, R. Feder, D. Johnson, and R. Palladino, “Edge rotation and temperature diagnostic on the National Spherical Torus Experiment,” *Review of scientific instruments*, vol. 75, p. 650, 2004.
- [73] J. Weaver and B. McCall, “Crc handbook of chemistry and physics,” *Journal of the American Chemical Society*, vol. 129, no. 3, p. 724, 2005.
- [74] *Spectroscopy Development Platform – OmniDrivers*. <http://www.oceanoptics.com/products/omnidriver.asp> [cite-1.5.2012].
- [75] T. Odstrčil, “Project: Ocean Optics spectrometer data analyzer.” <http://sourceforge.net/p/oospecanalyzer> [cite-1.5.2012].
- [76] Y. Ralchenko, A. Kramida, J. Reader, and et al., “NIST Atomic Spectra Database (ver. 4.0.1).” *National Institute of Standards and Technology, Gaithersburg, MD*, <http://physics.nist.gov/asd>, [2011, March 27].

- [77] O. Grover, “Project: Python API for the GOLEM Tokamak discharge database.” <http://sourceforge.net/p/pygolem> [cite-1.5.2012].
- [78] Andor Technology, *Programmer’s guide to: Andor Basic*. http://www.lot-oriel.com/files/downloads/andor/en/cc_andorbasicmanual_deen01.pdf [cite-1.5.2012].
- [79] P. Carolan, N. Conway, M. R. Tournianski, R. Akers, G. Counsell, M. Dunstan, A. Field, A. O’Connell, and M. J. Walsh, “Poloidal Rotation between ELMs in the START,” 1998. poster, UKAEA.
- [80] R. Golingo and U. Shumlak, “Spatial deconvolution technique to obtain velocity profiles from chord integrated spectra,” *Review of scientific instruments*, vol. 74, p. 2332, 2003.
- [81] I. Condrea, E. Haddad, B. Gregory, and G. Abel, “Local poloidal and toroidal plasma rotation velocities and ion temperature in a tokamak plasma obtained with a matrix inversion method considering asymmetries,” *Physics of Plasmas*, vol. 7, p. 3641, 2000.
- [82] R. Bell, “An inversion technique to obtain full poloidal velocity profiles in a tokamak plasma,” *Review of scientific instruments*, vol. 68, p. 1273, 1997.
- [83] N. Conway, P. Carolan, and M. Tournianski, “The unfolding of multichord doppler spectrometry,” *Review of scientific instruments*, vol. 70, p. 934, 1999.
- [84] A. Field, G. Fussmann, and J. Hofmann, “Measurement of the radial electric field in the asdex tokamak,” *Nuclear fusion*, vol. 32, p. 1191, 1992.
- [85] R. O’Connell, *Impurity fluid investigations on the COMPASS-D tokamak*. PhD thesis, University College of Dublin, 1996.
- [86] T. Todd, P. Carolan, N. Conway, I. Melnick, R. O’Connell, N. Peacock, and M. Walsh, “High resolution diagnostics on COMPASS-D and START,” *Fusion engineering and design*, vol. 34, pp. 823–827, 1997.
- [87] P. Carolan, S. Fielding, S. Gerasimov, J. Hugill, A. Morris, D. Robinson, T. Todd, M. Valovic, J. Ashall, K. Axon, *et al.*, “Characteristics of ohmic h-modes in COMPASS-D,” *Plasma physics and controlled fusion*, vol. 36, p. A111, 1994.
- [88] C. Bunting, P. Carolan, A. Field, and M. Forrest, “Spectroscopy of plasmas with a multifiber commutator,” *Review of Scientific Instruments*, vol. 57, p. 2015, 1986.